

CMEMS-LSCE: A global 0.25-degree, monthly reconstruction of the surface ocean carbonate system

Thi-Tuyet-Trang Chau¹, Marion Gehlen¹, Nicolas Metzler², and Frédéric Chevallier¹

¹Laboratoire des Sciences du Climat et de l'Environnement, LSCE/IPSL, CEA-CNRS-UVSQ, Université Paris-Saclay, F-91191 Gif-sur-Yvette, France

²Laboratoire LOCEAN (IPSL), Sorbonne Université, CNRS-IRD-MNHN, Paris, F-75005, France

Correspondence: Thi-Tuyet-Trang CHAU (trang.chau@lsce.ipsl.fr, thi.tuyet.trang.chau@gmail.com)

Abstract. Observation-based data reconstructions of global surface ocean carbonate system variables play an essential role in monitoring the recent status of ocean carbon uptake and ocean acidification as well as their impacts on marine organisms and ecosystems. So far ongoing efforts are directed towards exploring new approaches to describe the complete marine carbonate system and to better recover its fine-scale features. In this respect, our research activities within the Copernicus Marine Environment Monitoring Service (CMEMS) aim at developing a sustainable production chain of observation-derived global ocean carbonate system datasets at high space-time resolution. As the start of the long-term objective, this study introduces a new global 0.25° monthly reconstruction, namely CMEMS-LSCE, for the period 1985-2021. The CMEMS-LSCE reconstruction derives datasets of six carbonate system variables including surface ocean partial pressure of CO₂ ($p\text{CO}_2$), total alkalinity (A_T), total dissolved inorganic carbon (DIC), surface ocean pH, and saturation states with respect to aragonite (Ω_{ar}) and calcite (Ω_{ca}). Reconstructing $p\text{CO}_2$ relies on an ensemble of neural network models mapping gridded observation-based data provided by the Surface Ocean CO₂ Atlas (SOCAT). Surface ocean A_T is estimated with a multiple linear regression approach, and the remaining carbonate variables are resolved by CO₂ system speciation given the reconstructed $p\text{CO}_2$ and A_T . 1σ -uncertainty associated with these estimates is also provided. Here, σ stands for either ensemble standard deviation of $p\text{CO}_2$ estimates or total uncertainty for each of the five other variables propagated through the processing chain with input data uncertainty. We demonstrate that the 0.25°-resolution $p\text{CO}_2$ product outperforms a coarser spatial resolution (1°) thanks to a higher data coverage nearshore and a better description of horizontal and temporal variations in $p\text{CO}_2$ across diverse ocean basins, particularly in the coastal-open-ocean continuum. Product qualification with observation-based data confirms reliable reconstructions with root-of-mean-square-deviation from observations less than 8%, 4%, and 1% relative to the global mean of $p\text{CO}_2$, A_T (DIC), and pH. The global average 1σ -uncertainty is below 5% and 8% for $p\text{CO}_2$ and Ω_{ar} (Ω_{ca}), 2% for A_T and DIC, and 0.4% for pH relative to their global mean values. Both model-observation misfit and model uncertainty indicate that coastal data reproduction still needs further improvement, wherein high temporal and horizontal gradients of carbonate variables and representative uncertainty from data sampling would be taken into account in priority. This study also presents a potential use case of the CMEMS-LSCE carbonate data product in tracking the recent state of ocean acidification.

1 Introduction

25 Between 1750 and 2019, the ocean took up an estimated 25% (or 170 ± 20 PgC) of total cumulated anthropogenic CO_2 (685 ± 75 PgC) emitted to the atmosphere (IPCC AR6 - the Sixth Assessment Report of the United Nations Intergovernmental Panel on Climate Change, Canadell et al., 2021). While the uptake of anthropogenic CO_2 mitigates global warming it also profoundly modifies seawater chemistry in a suite of well-understood reactions (Orr et al., 2005) leading to an increase in hydrogen ion concentration ($[\text{H}^+]$), as well as a decrease in carbonate ion concentration ($[\text{CO}_3^{2-}]$) and in the saturation state of seawater (Ω)
30 with respect to calcium carbonate minerals (CaCO_3). The increase in hydrogen ion concentration ($[\text{H}^+]$) is commonly reported as a decrease in pH ($\text{pH} = -\log[\text{H}^+]$) and referred to as ocean acidification.

Changes in carbonate chemistry impact calcifying plankton and benthos as a direct result of decreasing seawater saturation state with respect to CaCO_3 (Fabry et al., 2008; Thomsen et al., 2015). Ocean acidification also modifies the production of marine trace gases exchanged at the air-sea interface (Hopkins et al., 2020), the availability of nutrients fueling primary
35 production (Doney et al., 2009), as well as the speciation of pollutants (Millero et al., 2009; Hoffmann et al., 2012). These chemical changes interact with warming and ocean deoxygenation to drive major changes in marine ecosystems (Doney et al., 2020) and to alter global biogeochemical cycles with the potential for feeding back on radiative forcing (Gehlen et al., 2011; Hopkins et al., 2020). The likelihood for major disruptive impacts of ocean acidification on marine ecosystems, if future CO_2 emissions were to go unabated, is reflected by the Sustainable Development Goal 14.3 (SDG 14.3) - "Reduce Ocean
40 Acidification: minimize and address impacts of ocean acidification" (<https://www.globalgoals.org/14-life-below-water>, last access: 20/03/2023). Albeit not specifically mentioned, moving towards SDG 14.3 implies the understanding of historical and contemporary carbonate chemistry, its mean state, trends and variability.

In situ time series have played an important role in monitoring ocean acidification over the last decades (Bates et al., 2014; Lauvset et al., 2015; Sutton et al., 2019; Pérez et al., 2021; Leseurre et al., 2022; Skjelvan et al., 2022). At these sites, seawater
45 pH (Ω) has been either directly measured or calculated from measurements of other carbonate system variables. These variables include surface ocean partial pressure of CO_2 ($p\text{CO}_2$), total alkalinity (A_T), and dissolved inorganic carbon (DIC). While changes in time series of carbonate system variables well reflect impacts of enhanced anthropogenic CO_2 uptake on ocean chemistry at a local scale (Steinberg et al., 2001; González-Dávila and Santana-Casiano, 2009; Dore et al., 2009; Bates et al., 2014; Pérez et al., 2021), the reliable upscaling to large ocean regions or entire basins requires a significant extension of the
50 existing observing network (Lauvset et al., 2015; Bakker et al., 2016; Sutton et al., 2019; Lauvset et al., 2022a).

Time series data are completed by bottle data from international cruises. These data are synthesized by the Global Ocean Data Analysis Project v2.2022 (GLODAPv2.2022) and include about 1.4 million measurements of surface-to-interior ocean pH , A_T , DIC, and other parameters (Lauvset et al., 2022b, <https://www.glodap.info/>, last access: 30/9/2022). Likewise, underway measurements of near-surface CO_2 fugacity, i.e., $p\text{CO}_2$ corrected for non-ideal gas behavior, are compiled in the Surface Ocean
55 CO_2 Atlas (SOCAT) since its first release in 2011 (Pfeil et al., 2013). That latest version SOCATv2022 yields approximately 33.7 million high-quality controlled data (Bakker et al., 2022, <http://www.socat.info/>, last access: 17/6/2022). Despite millions of observations available, data coverage is still modest, e.g., CO_2 fugacity samples over the global ocean cover less than 2%

of its surface for each month in the last three decades (Bakker et al., 2016; Hauck et al., 2020). Mapping methods have thus become an essential tool in ocean carbon cycle research allowing to interpolate or extrapolate these sparse measurements into
60 space-time varying fields of carbonate system variables.

Recent years have seen the rapid development of machine learning approaches to map global surface ocean $p\text{CO}_2$ (see Rödenbeck et al., 2013; Landschützer et al., 2016; Denvil-Sommer et al., 2019; Gregor et al., 2019; Chau et al., 2022b, for instance). Thanks to these efforts, the carbon cycle community can now draw on an ensemble of reconstructions for the observation-based assessment of the ocean carbon sink (Friedlingstein et al., 2022). However, only a few global observation-
65 based reconstructions are available for $p\text{H}$, A_{T} , DIC, and Ω with respect to calcite and aragonite (see Gregor and Gruber, 2021, for a review). The reconstruction of global distributions of these variables is hampered by an insufficient amount of direct measurements (Bakker et al., 2016; Lauvset et al., 2022a). Alternatively, the complete carbonate system can be obtained by speciation given the information of any couple of $p\text{CO}_2$, $p\text{H}$, A_{T} or DIC together with chemical (e.g., phosphate, silicate, nitrate) and physical variables (e.g., temperature, salinity), as well as corresponding dissociation constants (Park, 1969; Lewis
70 and Wallace, 1998; Dickson et al., 2007).

Regardless of the developments in different observation-based estimation methods, Takahashi et al. (2014), Iida et al. (2021), and Gregor and Gruber (2021) propose global climatologies or monthly varying fields of all variables of the carbonate system, i.e., $p\text{CO}_2$, $p\text{H}$, A_{T} , DIC, and Ω . These data products have a spatial resolution of 1° ($\sim 100\text{km} \times 100\text{km}$) or even coarser. Nevertheless, the variations of carbonate system variables over the coastal regions where their instantaneous gradients are
75 driven by smaller-scale features like ocean upwelling, wind turbulence, eddies, water runoff, and sharp biological productivity (Jones et al., 2012; Bakker et al., 2016; Laruelle et al., 2017) are poorly described at such spatial resolutions. Here we improve on existing studies by providing a global 0.25° , monthly observation-based product consisting of datasets of six core surface ocean carbonate system variables of the marine carbonate system and their associated 1σ -uncertainty. This high-resolution data product covers the years from 1985 to 2021. Laboratoire des Sciences du Climat et de l'Environnement (LSCE) is in charge of
80 the product within the European Copernicus Marine Environment Monitoring Service (CMEMS). Our product is referred to as CMEMS-LSCE hereafter.

The reconstruction of surface ocean carbonate system variables starts with the reconstruction of surface ocean $p\text{CO}_2$ and A_{T} in each regular grid of $1\text{month} \times 0.25^\circ \times 0.25^\circ$ in the period 1985-2021 (444 months in total). Next, variables $p\text{H}$, DIC, and Ω are derived by speciation. Advantages of the combination of $p\text{CO}_2$ and A_{T} over others for the speciation of the carbonate system
85 are: (1) $p\text{CO}_2$ is the most extensively measured parameter, (2) A_{T} can be accurately predicted from salinity, temperature, and nutrient concentrations, and (3) the combination of these two prior variables results in the slightest uncertainty of $p\text{H}$ estimates (Zeebe and Wolf-Gladrow, 2001; Lauvset and Gruber, 2014; Takahashi et al., 2014; Orr et al., 2018). The three main successive modules used in the CMEMS-LSCE production chain are summarized as follows.

i) *Reconstruction of $p\text{CO}_2$* (Sect. 3.1): the CMEMS-LSCE-FFNN ensemble-based approach (Chau et al., 2022b) is modified to map gridded datasets of SOCATv2022 CO_2 fugacity and predictors in order to reconstruct $p\text{CO}_2$ at a finer spatial
90 scale resolution of 0.25° for every month in the period 1985-2021 (444 months in total). The spatial resolution of new feed-forward neural networks (FFNNs) is 16-fold higher than the original. By design, the ensemble of model outputs

allows to yield the best model estimate (i.e., ensemble mean) and model uncertainty (i.e., ensemble standard deviation) at each 0.25° -grid cell and each month. Global monthly reconstructions of $p\text{CO}_2$ proposed by this study complement the previous climatological product by Landschützer et al. (2020), i.e., a combination of the two existing datasets covering respectively the open ocean at 1° (Landschützer et al., 2016) and the coastal sector at 0.25° (Laruelle et al., 2017).

ii) *Reconstruction of A_T* (Sect. 3.2): locally interpolated alkalinity regression (LIAR; Carter et al., 2016, 2018) is chosen to estimate monthly total alkalinity over the global surface ocean. Various reconstruction methods for A_T exist (see Carter et al., 2016; Broullón et al., 2019; Gregor and Gruber, 2021, for a review), but we choose LIAR due to its global applicability, simplicity in setting, and accuracy compared to other published approaches (Carter et al., 2018; Gregor and Gruber, 2021). Importantly, LIAR allows determining reconstruction uncertainty propagated from multiple sources of input uncertainties at desired model resolutions.

iii) *Reconstruction of pH , DIC , and saturation states with respect to aragonite (Ω_{ar}) and calcite (Ω_{ca})* (Sect. 3.3): CO2SYS (Lewis and Wallace, 1998; Van Heuven et al., 2011) is a standard software used for the speciation of carbonate parameters in the marine CO_2 system (see Olsen et al., 2016; Bresnahan et al., 2021; Gregor and Gruber, 2021; Woosley, 2021, for a few). A complementary of the CO2SYS software developed by Orr et al. (2018) is used to quantify the uncertainty associated with these carbonate system variables. All the input data uncertainties are propagated through the CO2SYS processing chain.

The global monthly, 0.25° -resolution datasets of surface carbonate variables are intensively evaluated against different observation-based products independent from our model fitting at a global scale to in situ locations. In Section 4, multiple metrics are proposed for product analyses and assessments. Results are presented in section 5 with emphasis on the evaluation of the best reconstruction and associated model uncertainty for each variable (Sect. 5). This section also highlights the advantages obtained with an increase in spatial resolution and presents an application of the CMEMS-LSCE product in tracking ocean acidification over the last three decades. Section 6 summarizes key results, discusses the potential for future model upgrades, and introduces possible product use cases. The high-resolution data product described in this manuscript (netCDF format) can be accessed via repository under data DOI: 10.14768/a2f0891b-763a-49e9-af1b-78ed78b16982.

2 Data used and reprocessing

2.1 Input data products for surface ocean carbonate system reconstructions

Many observation-based products are used as predictors of our target carbonate system variables (Table 1). Global ocean maps of sea surface temperature (SST), sea surface salinity (SSS), sea surface height above geoid (SSH), chlorophyll-*a* (Chl-*a*) come from the Copernicus Marine Environment Monitoring Service (CMEMS: Good et al., 2020; Nardelli et al., 2016; Droghei et al., 2018; Maritorena et al., 2010). Mixed layer depth (MLD) fields belong to Estimating the Circulation and Climate of the Ocean project Phase II (ECCO2, Menemenlis et al., 2008). CO_2 mole fractions ($x\text{CO}_2$) are derived from the CO_2

atmospheric inversion of the Copernicus Atmosphere Monitoring Service (CAMS, Chevallier et al., 2005, 2010; Chevallier, 2013). Surface ocean concentrations of nitrate (NO_3), silicate (SiO_2), and phosphate (PO_4) are extracted from the World Ocean Atlas 2018 (WOA18, Garcia et al., 2019). The climatological $p\text{CO}_2$ ($p\text{CO}_2^{\text{clim}}$) product is provided by Lamont Doherty Earth Observatory (LDEO, Takahashi et al., 2009). Details of these products including resource access, data coverage, and resolutions are presented in Table 1.

Table 1. Input data used in the reconstructions of CMEMS-LSCE carbonate system variables over the global ocean in 1985-2021.

Variables	Notations	Units	Products	Resolutions	References
1. CO_2 fugacity	$f\text{CO}_2$	μatm	Surface Ocean CO_2 Atlas version 2022 (SOCATv2022, 1985-2021)	monthly, 1° (open ocean) and 0.25° (coastal ocean)	Bakker et al. (2022)
2. Sea surface temperature	SST	$^\circ\text{C}$	CMEMS SST_GLO_SST_L4_REP_OBSERVATIONS_010_011 and SST_GLO_SST_L4_NRT_OBSERVATIONS_010_001 (1985-2021)	daily, 0.05°	Good et al. (2020)
3. Sea surface salinity	SSS	PSU	CMEMS MULTIOBS_GLO_PHY_S_SURFACE_MYNRT_015_013 (1993-2021)	monthly, 0.25°	Nardelli et al. (2016); Droghei et al. (2018)
4. Sea surface height	SSH	m	CMEMS SEALEVEL_GLO_PHY_L4_MY_008_047 and SEALEVEL_GLO_PHY_L4_NRT_OBSERVATIONS_008_046 (1993-2021)	daily, 0.25°	CLS-TOULOUSE
5. Mixed layer depth	MLD	m	Estimating the Circulation and Climate of the Ocean project Phase II (ECCO2, 1992-2021)	daily, 0.25°	Menemenlis et al. (2008)
6. Chlorophyll- <i>a</i>	CHL- <i>a</i>	mg m^{-3}	CMEMS OCEANCOLOUR_GLO_CHL_L4_REP_OBSERVATIONS_009_082 and OCEANCOLOUR_GLO_CHL_L4_NRT_OBSERVATIONS_009_033 (1998-2021)	daily, 0.25°	GLOCOLOUR, Maritorena et al. (2010)
7. CO_2 mole fraction	$x\text{CO}_2$	ppm	CO_2 atmospheric inversion from the Copernicus Atmosphere Monitoring Service (CAMS, 1985-2021)	3-hourly, $1.9^\circ \times 3.75^\circ$	Chevallier et al. (2005, 2010); Chevallier (2013)
8. $p\text{CO}_2$ climatology	$p\text{CO}_2^{\text{clim}}$	μatm	Lamont Doherty Earth Observatory (LDEO, climatology)	monthly, $4^\circ \times 5^\circ$	Takahashi et al. (2009)
9. Nitrate 10. Silicate 11. Phosphate	NO_3 SiO_2 PO_4	$\mu\text{mol kg}^{-1}$	World Ocean Atlas 2018 (WOA18, climatologies)	monthly, 1°	Garcia et al. (2019)

* Last access was on 15/4/2022 for all input databases except for SOCATv2022 data (17/6/2022) and WOA18 data (30/7/2022).

** Data products 1-8 are used in the $p\text{CO}_2$ reconstruction. Products 2-3 and 9-11 are used to compute A_T , DIC, pH, Ω_{ar} , and Ω_{ca} .

*** Global values of product uncertainty (data[†] or analysis errors expressed as σ) have been reported for $f\text{CO}_2^\dagger$ ($< 5 \mu\text{atm}$), SST (0.15°C), SSS (0.2 PSU), SSH (0.02 m), MLD (-), CHL-*a* (0.03 mg m^{-3}), $x\text{CO}_2$ (-), $p\text{CO}_2^{\text{clim}}$ ($10 \mu\text{atm}$), NO_3 ($1.8 \mu\text{mol kg}^{-1}$), SiO_2 ($3.6 \mu\text{mol kg}^{-1}$), PO_4 ($0.12 \mu\text{mol kg}^{-1}$).

With the exception of $x\text{CO}_2$, nutrient concentrations, and $p\text{CO}_2^{\text{clim}}$, these input data products have original resolutions equivalent to or even finer than a spatial resolution of 0.25° and a temporal resolution of monthly. When mismatches in data resolutions appear, input data products are interpolated to fit the pre-defined model resolutions. The datasets of SST and $x\text{CO}_2$ - the two key variables driving global $p\text{CO}_2$ changes (Bates et al., 2014; Gruber et al., 2019; Landschützer et al., 2019; Chau et al., 2022b; Friedlingstein et al., 2022) - cover the full learning period and the whole globe as expected. The other predictor data are not available before the 1990s, when new types of satellite measurements started, and one of them (i.e., Chl-*a*) does not cover the high latitudes of the winter hemisphere. We therefore gap-fill the time series in an ad hoc manner, as in previous

studies (Landschützer et al., 2016; Gregor et al., 2019; Chau et al., 2022b). Monthly climatologies of SSS, Chl-*a*, and MLD computed on the available data are used for each missing year. Likewise, climatologies plus linear trends of SSH following global warming effects serve for the pre-1993 period. Missing Chl-*a* data in the high latitudes of the winter hemisphere are replaced by the minimum concentration of Chl-*a* over the available data for the same grid cell ($\sim 0.01 \text{ mg m}^{-3}$). WOA18 nutrients and LDEO $p\text{CO}_2^{\text{clim}}$ are already climatologies per se and we apply them for all the analysis years 1985-2021. The sine function is applied to convert latitude while both the sine and cosine are used to transform longitude to conserve their periodical behaviors.

CO_2 fugacity from SOCATv2022 (Bakker et al., 2022) is used as the target data in our monthly $p\text{CO}_2$ reconstructions. The SOCAT project collects and qualifies underway observations via international vessels, moorings, or autonomous platforms. It grids the observations at spatial resolutions of 1° or 0.25° resulting in the two major SOCAT gridded data products. The temporal resolution of these two products is monthly. While the 1° -data product (SOCATv2022r100) covers the global ocean, the 0.25° covers solely the coastal regions. The SOCAT coastal areas is within 400 km from the shoreline (Sabine et al., 2013; Bakker et al., 2016); see Fig. A1a for an illustration. To merge the two resolutions, we first duplicate the 1° -open-ocean SOCATv2022 data ($\sim 2 \times 10^5$ data points) over its sixteen 0.25° sub-cells. This 0.25° -open-ocean data are then combined with the 0.25° -coastal-ocean SOCATv2022 data ($\sim 4 \times 10^5$ data points) to generate a global monthly 0.25° ocean data product fed to our reconstruction model of $p\text{CO}_2$ (Sect. 3.1). The merged SOCATv2022 product at monthly, 0.25° resolutions is referred to as SOCATv2022r025 hereafter. The assumption of open-ocean data homogeneity of $p\text{CO}_2$ within 1° -grid boxes ($\sim 100 \text{ km} \times 100 \text{ km}$) does not degrade the reconstruction skill over the global open ocean (see Sect. 5 for results) where $p\text{CO}_2$ observations are spatially auto-correlated within a global median distance of $400 \pm 250 \text{ km}$ (Jones et al., 2012). The data distribution of SOCATv2022 CO_2 fugacity before and after combining is shown in Fig. A2 and Table 3.

2.2 Product qualification and comparison

The monthly, 0.25° -resolution reconstructions of carbonate system variables are qualified with gridded observation-based datasets and in-situ time series which are not used in our model fitting (Table 2).

- The SOCAT data in each reconstruction month are excluded from the model fitting, which avoids overfitting and ensures fairness in the model evaluation (Chau et al., 2022b). The global monthly, 0.25° -resolution CMEMS-LSCE-FFNN $p\text{CO}_2$ fields can therefore be evaluated against the $p\text{CO}_2$ data converted from SOCATv2022 CO_2 fugacity (Körtzinger, 1999) at the same resolution. Doing this, CMEMS-LSCE-FFNN $p\text{CO}_2$ is assessed with more than 32×10^5 open-ocean data and 4×10^5 coastal-ocean data (Table 3). The SOCATv2022 data have low random uncertainty (2-5 μatm) but the spatio-temporal sampling bias from the month and grid centers is significant (Bakker et al., 2016). The 0.25° -data reconstruction is also compared to its previous version with a spatial resolution of 1° (Chau et al., 2022a, b).
- The monthly, 0.25° reconstructions of A_T , DIC, and $p\text{H}$ are qualified based on GLODAPv2.2022 data (Lauvset et al., 2022b). GLODAP provides non-gridded datasets of ocean carbon variables which have been compiled and bias-corrected from water samples taken at various depths. The measurement uncertainty is $4 \mu\text{mol kg}^{-1}$ in A_T and DIC and between

0.01 – 0.02 in *pH* (Lauvset et al., 2022a). Only direct measurements at depths shallower than 10 m and with a flag of 2
170 (best quality control) are selected for this evaluation. Measurements in each box of 1month × 10m × 0.25° × 0.25° are
averaged to obtain representative data of surface A_T , DIC, and *pH* at 0.25°-grid cells for months in the period 1985-2021.
This results in roughly 16×10^3 data points for A_T and DIC over the global ocean (Table 4). Only half of that amount
stems from direct *pH* measurements. Another half, referred to as indirect measurements (i.e., *pH* calculated with A_T and
DIC), is excluded from this data evaluation. Over 30% of GLODAP data are distributed along the coasts.

175 • In situ time series of direct measurements of carbonate system variables (*pCO*₂, A_T , DIC, and *pH*) are used to qualify
our product at local scale (Table 2).

a) Sutton et al. (2019) present data over multiple sites equipped with autonomous moorings measuring surface ocean
*pCO*₂ and *pH* since 2004. These stations cover a wide range of oceanic conditions from the tropics to high latitudes
(Fig. A1b). More than half of 42 stations distribute over the continental shelves, and many of them observe *pCO*₂
180 and *pH* in the regime of coral reefs (Tables A2 and A3). Measurement uncertainty is up to 2 μ atm reported for
*pCO*₂ and 0.02 for *pH*.

b) For A_T and DIC, we consider eight time series accessible to provide insights into changes in the surface ocean
carbonate system over the recent decades (Bates et al., 2014; Coppola et al., 2020; Gregor and Gruber, 2021; Pérez
et al., 2021; Leseurre et al., 2022). Two of them belong to the biogeochemical observing systems located in the
185 subtropical Atlantic: Bermuda Atlantic Time Series (BATS, Michaels and Knap, 1996; Steinberg et al., 2001) and
European Station for Time-Series in the Ocean Canary islands (ESTOC, González-Dávila and Santana-Casiano,
2009). The other two provide direct measurements in the same ocean basin but in the subpolar region: Irminger Sea
and Iceland Sea (IRMINGER and ICELAND, Olafsson et al., 2010). Further mentions time series distributed in
specific conditions including a high-Arctic fjord in Svalbard (AWIPEV, Fischer et al., 2017; Gattuso et al., 2023)
190 and the Mediterranean basin (DYFAMED, Coppola et al., 2021). Hawaii Ocean Time-series in the subtropical
North Pacific (HOT, Dore et al., 2009) and OISO time series in the subpolar Southern Ocean (KERFIX, Metzl
and Lo Monaco, 1998) allow to complete the reconstruction qualification in different ocean basins. Measurement
uncertainty (f.i., from replication experiments) reported at these sites is below 3 μ molkg⁻¹. Except for HOT and
ESTOC (surface ocean measurements), data over all the stations are extracted at seawater depth shallower than
195 10 m. A monthly average is applied for all the mentioned time series in order to be compatible with output from
the CMEMS-LSCE chain of models.

Table 2. Data sources used in product evaluation and comparison. Values in brackets of each variable present measurement-based data uncertainty or analysis[‡] uncertainty.

	Product	Data type	Evaluation variables	Reference
Global ocean	1. Surface Ocean CO ₂ Atlas version 2022 (SOCATv2022, 1985-2021), last access: 17/6/2022	observation-based gridding, resolution: 1° (global ocean) and 0.25° (coastal ocean), monthly	$p\text{CO}_2$ ($< 5 \mu\text{atm}$)	Bakker et al. (2022)
	2. CMEMS global ocean surface carbon product (MULTI-OBS_GLO_BIO_CARBON_SURFACE_REP_015_008, 1985-2021), last access: 05/12/2022	SOCAT-based reconstruction, resolution: 1°, monthly	$p\text{CO}_2^{\ddagger}$ ($8 \mu\text{atm}$)	Chau et al. (2022a, b)
	3. Global Ocean Data Analysis Project bottle data version 2.2022 (GLODAPv2.2022, 1985-2021), last access: 30/9/2022	observation	A_T ($4 \mu\text{mol kg}^{-1}$) DIC ($4 \mu\text{mol kg}^{-1}$) $p\text{H}$ ($0.01 - 0.02$)	Lauvset et al. (2022a, b)
Time series stations	4. Autonomous time series from surface buoys since 2004 (see details in Table A2), last access: 15/10/2022	observation	$p\text{CO}_2$ ($2 \mu\text{atm}$) $p\text{H}$ (0.02)	Sutton et al. (2019)
	5. Bermuda Atlantic Time Series (BATS: 31.7°N-64.2°W, 1988-2021), last access: 30/10/2022	observation	A_T ($3 \mu\text{mol kg}^{-1}$) DIC ($1 \mu\text{mol kg}^{-1}$)	Michaels and Knap (1996); Steinberg et al. (2001)
	6. Atmospheric Flux Dynamics Time Series in the Mediterranean (DYFAMED: 43.5°N-7.9°E, 1998-2017), last access: 23/03/2023	observation	A_T , DIC	Coppola et al. (2020, 2021)
	7. European Station for Time-Series in the Ocean Canary islands (ES-TOC: 29.2°N-15.5°W, 1995-2009), last access: 30/10/2022	observation	A_T , DIC	González-Dávila and Santana-Casiano (2009)
	8. Hawaii Ocean Time-series (HOT: 22.5°N-158.1°W, 1988-2020), last access: 30/10/2022	observation	A_T , DIC	Dore et al. (2009)
	9. Underwater observatory in Spitsbergen (Svalbard) (AWIPEV: 78.93°N-11.92°E, 2015-2020), last access: 20/07/2023	observation	A_T ($2.6 \mu\text{mol kg}^{-1}$) DIC ($3 \mu\text{mol kg}^{-1}$)	Fischer et al. (2017); Gattuso et al. (2023)
	10. Irminger Sea and the Iceland Sea time series (IRMINGER: 64.33°N-28.00°W, 2014-2021; ICELAND: 68.00°N-12.67°W, 2014-2021), last access: 20/07/2023	observation	A_T (-) DIC ($2 \mu\text{mol kg}^{-1}$)	Olafsson et al. (2010)
	11. Southern Ocean time series under the OISO project (KERFIX: 50.67°S-68.42°E, 1992-2018), last access: 20/07/2023	observation	A_T ($3 \mu\text{mol kg}^{-1}$) DIC ($3 \mu\text{mol kg}^{-1}$)	Metzl and Lo Monaco (1998)

3 Reconstruction methods

3.1 Ensemble $p\text{CO}_2$ mapping feed-forward neural networks

The CMEMS-LSCE-FFNN (Chau et al., 2022b) is based on an ensemble of 100 feed-forward neural network (FFNN) models mapping SOCAT CO_2 fugacity ($f\text{CO}_2$) and predictor variables (Eq. 1).

$$f\text{CO}_2 = \text{FFNN}(\text{SST}, \text{SSS}, \text{SSH}, \text{Chl} - a, \text{MLD}, x\text{CO}_2, f\text{CO}_2^{\text{clim}}, \text{latitude}, \text{longitude}) \quad (1)$$

The predictors of $f\text{CO}_2$ include sea surface temperature (SST), salinity (SSS), surface height (SSH), chlorophyll- a (Chl- a), mixed layer depth (MLD), CO_2 mole fraction ($x\text{CO}_2$), $f\text{CO}_2$ climatologies ($f\text{CO}_2^{\text{clim}}$), and the geographical coordinates (latitude and longitude). The datasets of SOCAT $f\text{CO}_2$ and predictors are first reprocessed to match model fitting requirements (Sect. 2.1). After excluding the data in the reconstruction month, the data within the 3-month window are randomly separated into FFNN training and validation subsets with a ratio of 2 : 1. The subsampling process is repeated for each 100 FFNN runs that results in 100 different datasets for model fitting. The excluded SOCATv2022 datasets are used in model evaluation. The CMEMS-LSCE-FFNN approach was originally developed for $p\text{CO}_2$ reconstructions at monthly, 1° resolutions where $p\text{CO}_2$ is converted from $f\text{CO}_2$ following the formulation by Körtzinger (1999). The model best estimate and its uncertainty are defined as the ensemble mean (μ) and ensemble spread (σ) of 100 model outputs of $p\text{CO}_2$.

This study slightly modifies the CMEMS-LSCE-FFNN ensemble approach by Chau et al. (2022b) to achieve $p\text{CO}_2$ reconstructions at monthly, 0.25° resolutions. Some of the input datasets presented here (Table 1) are different from those presented in Chau et al. (2022b) (Table S1). The up-to-date input datasets have higher resolutions and a better coverage over the coastal ocean as well as in the high latitudes. Furthermore, the new CMEMS data resources offer space-time varying uncertainty fields which are important in quantifying carbonate system variable uncertainties.

For comparable evaluations in this study, we execute 100-member ensembles of FFNN models at spatial resolutions of both 1° (FFNNr100) and 0.25° (FFNNr025) using the same lot of input data resources (Table 1). Remind that the training data of $f\text{CO}_2$ is extracted from the SOCATv2022r100 product for FFNNr100 while it comes from the SOCATv2022r025 product (i.e., the merged product of the 1° -open-ocean dataset and the 0.25° -coastal-ocean dataset) for FFNNr025. All input datasets are reprocessed with respect to each model resolution (Sect. 2.1). Sect. 3.1 compares these two CMEMS-LSCE-FFNN versions and highlights the skill of the finer resolution data product.

3.2 Locally interpolated alkalinity regression

Locally interpolated alkalinity regression (LIAR; Carter et al., 2016, 2018) is an ensemble-based regression method developed for the global reconstruction of total alkalinity (A_T). Regression coefficients were learned on GLODAPv2 data (Olsen et al., 2016) binned within regular windows of $5^\circ \times 5^\circ$. For prediction, the LIAR software interpolates between the regression coefficients to arbitrary resolutions specified by the users. This study employs eight LIAR models (Carter et al., 2018, Table 2) for calculating A_T at monthly, 0.25° resolutions. Each model represents a combination of predictor variables (see the full

presentation in Eq. 2),

$$A_T = \text{LIAR}(\text{SSS}, \text{SST}, \text{NO}_3, \text{SiO}_2). \quad (2)$$

230 The eight regression models include salinity (SSS) - the predominant predictor of A_T - and some combinations of temperature (SST), nitrate (NO_3), and silicate (SiO_2). The model which has the smallest propagation uncertainty is chosen to provide the best estimate of A_T .

Global monthly total alkalinity and 1σ -uncertainty are estimated with given input data from the monthly CMEMS SSS and SST fields and from the WOA18 datasets of nutrient concentrations (Table 1). Uncertainty of the A_T field is estimated
235 systematically through input uncertainty propagation along the processing chain (Carter et al., 2018). Here we define the input uncertainty of predictors in terms of standard deviations (1σ). Input uncertainty fields associated to the monthly CMEMS SSS and SST are products' analysis errors (see e.g., Fig. A7) while uncertainties of the WOA18 NO_3 and SiO_2 climatologies are set to 15% of data values per cell. The 15% quantity refers to the median percentage of standard analysis errors against climatological means of nutrient concentrations (see product standard errors in Table 6, Garcia et al., 2019). The WOA18
240 standard analysis errors are defined as misfits between their interpolated data and GLODAPv2 bottle data (Olsen et al., 2016). Spatial distribution of the error percentage of the WOA18 nutrient concentrations at the ocean surface is illustrated in Fig. A8.

3.3 Carbonate system speciation

The CO2SYS speciation software was first developed by Lewis and Wallace (1998) to determine carbonate system parameters in the marine CO_2 system based on a set of equilibrium equations (Dickson et al., 2007). Here we use the speciation program
245 written by Van Heuven et al. (2011) and its extension with uncertainty propagation proposed by Orr et al. (2018). To obtain a complete description of the ocean carbonate system, the CO2SYS initialization requires the following input conditions:

- i) values of any couple of the parameters $p\text{CO}_2$, A_T , DIC, and $p\text{H}$,
- ii) temperature and pressure,
- iii) total concentrations of all the non- CO_2 acid-base systems,
- 250 iv) equilibrium constants used to describe seawater acid-base chemistry.

The (iii)-condition involves total concentrations of both conservative and non-conservative constituents in the non- CO_2 acid-base systems. The amount of conservative constituents such as borate, fluoride, and sulfate in surface seawater is estimated with salinity. The total concentration of non-conservative constituents (nutrients) is computed approximately with silicate (SiO_2), and phosphate (PO_4). Further information of the carbonate system speciation can be found in Dickson et al. (2007) and Dickson
255 (2010).

With the reconstructions of $p\text{CO}_2$ and A_T (Sects 3.1 and 3.2), the CO2SYS speciation software is used to derive $p\text{H}$, DIC, Ω_{ar} , and Ω_{ca} , and determine their uncertainty over the ocean surface at a resolution of 0.25° . Equation 3 expresses all input-output variables of CO2SYS for this study. Note that the estimates for other carbonate system variables such as hydrogen ion

(H^+) concentration and Revelle Factor (RF) - a measure of the carbonate buffer capacity- are also available (Figs. A4 and A6) but beyond the scope of our data evaluation.

$$pH, DIC, \Omega_{ar}, \Omega_{ca} = \text{CO2SYS}(p\text{CO}_2, A_T, \text{SST}, \text{SSS}, P, \text{SiO}_2, \text{PO}_4, \text{constants}) \quad (3)$$

The FFNN best estimate (ensemble mean) of $p\text{CO}_2$ reconstructions (Sect. 3.1) and the LIAR outputs of A_T (Sect. 3.2) are used as the prior inputs of the CO2SYS at each grid cell for every month in the period 1985-2021. We take the same data products of SST, SSS, and nutrient concentrations as for the previous reconstructions (Table 1). Pressure (P) is assumed to be 0 dbar at the ocean surface. For equilibrium constants, we choose the best empirical values recommended by Dickson et al. (2007) and Dickson (2010). These settings include (1) the dissociation constants K_1 and K_2 from Lueker et al. (2000) and K_{HSO_4} from Dickson (1990) in combination with the total boron-ratio-salinity formulation by Uppstrom (1974).

The uncertainty of the CO2SYS variables is estimated by error propagation (Orr et al., 2018). Inputs for the CO2SYS error propagation include the reconstruction uncertainty of $p\text{CO}_2$ (FFNN ensemble standard deviation) and of A_T (LIAR error propagation). The uncertainty of SST, SSS, and nutrient concentrations are set to the same values as in the previous section (Sect. 3.2). Equilibrium constants' standard errors are default values (see Table 1, Orr et al., 2018). As for FFNN and LIAR, uncertainty values of each carbonate system variable are computed for each month in 1985-2021 and at each 0.25° -grid box over the global surface ocean.

4 Evaluation metrics

4.1 Model best estimate and uncertainty quantification

The 100 FFNN models result in an ensemble of 100 estimates of global monthly, 0.25° surface ocean $p\text{CO}_2$ fields (Sect. 3.1). Specify any $t = 1 : 444$ (month), $i = 1 : 180$ (latitude), and $j = 1 : 360$ (longitude), the best estimate (μ_{tij}) and uncertainty (σ_{tij}) at time t and grid cell ij are deduced from 100 FFNN $p\text{CO}_2$ estimates ($X(t, i, j, m)_{m=1}^{m=100}$) as follows.

$$\mu_{tij} = \frac{\sum_{m=1}^{m=100} X(t, i, j, m)}{100}, \quad (4a)$$

$$\sigma_{tij} = \sqrt{\frac{\sum_{m=1}^{m=100} [X(t, i, j, m) - \mu_{tij}]^2}{100}}. \quad (4b)$$

For pH , A_T , DIC , Ω_{ar} , and Ω_{ca} , the best estimates and associated uncertainties (μ_{tij} and σ_{tij}) are obtained directly from the LIAR and CO2SYS speciation tools and their error propagation (Sects. 3.2 and 3.3).

To assign representatives of μ and σ estimates for carbonate system variables at a specific space-time window, we define statistics with respect to each of the three following cases:

285 i) a representative over a period of time (T months)

$$\mu_{ij} = \frac{\sum_t \mu_{tij}}{T}, \quad (5a)$$

$$\sigma_{ij} = \sqrt{\frac{\sum_t \sigma_{tij}^2}{T}}. \quad (5b)$$

ii) a representative over a region (e.g., ocean basins and sub-basins, the global ocean)

$$\mu_t = \frac{\sum_{ij} \mu_{tij} \times A_{ij}}{\sum_{ij} A_{ij}}, \quad (6a)$$

290
$$\sigma_t = \sqrt{\frac{\sum_{ij} \sigma_{tij}^2 \times A_{ij}}{\sum_{ij} A_{ij}}}. \quad (6b)$$

iii) a representative over a period of time and a region

$$\mu = \frac{\sum_{t,ij} \mu_{tij} \times A_{ij}}{T \times \sum_{ij} A_{ij}}, \quad (7a)$$

$$\sigma = \sqrt{\frac{\sum_{t,ij} \sigma_{tij}^2 \times A_{ij}}{T \times \sum_{ij} A_{ij}}}. \quad (7b)$$

where t is in a time period with length T and A_{ij} is the area of each grid cell in a desired region. It is noteworthy that the statistics in Eqs. (5b)-(7b) are not the standard deviation associated to the mean quantities in Eqs. (5a)-(7a), but they stand for the best representative of uncertainty estimates over an ocean basin and/or time period. These statistics also support for the comparison with model-observation deviation (e.g., Eq. 10) which is typically used in the calculation of standard uncertainty proposed in the previous studies (Jiang et al., 2019; Iida et al., 2021; Gregor and Gruber, 2021). Subscripts in the notations of the best model estimates (μ) and model uncertainties (σ) in Eqs. (4)-(7) are dropped out for general situations.

300 The best model estimate (μ) is assessed against model uncertainty (σ) through σ -to- μ ratio (%)

$$R(\mu, \sigma) = 100\% \frac{\sigma}{|\mu|}. \quad (8)$$

The σ -to- μ ratio allows evaluating the significance of the model estimate. Model estimates of carbonate variables are reliable with $R(\sigma, \mu)$ values less than 20% (Rose, 2013).

4.2 Model performance in comparison with evaluation data

305 Assume that μ_{tij} and O_{tij} are the best model estimate and an observation (or its gridded data) available at time t and grid cell ij , and μ and O are respectively their means over the total number of evaluation data (N). Model skills are assessed against observation data (Table 2) with the following metrics:

- mean model-observation differences (Bias)

$$\text{Bias} = \frac{\sum_{t,ij} (\mu_{tij} - O_{tij})}{N}, \quad (9)$$

310 • root-of-mean-square-deviation (RMSD)

$$\text{RMSD} = \sqrt{\frac{\sum_{t,ij} (\mu_{tij} - O_{tij})^2}{N}}, \quad (10)$$

• coefficient of determination (r^2)

$$r^2 = \frac{\left[\sum_{t,ij} (\mu_{tij} - \mu) \times (O_{tij} - O) \right]^2}{\sum_{t,ij} (\mu_{tij} - \mu)^2 \times \sum_{t,ij} (O_{tij} - O)^2}. \quad (11)$$

5 Results

315 5.1 Surface ocean $p\text{CO}_2$

This section presents the reconstruction of surface ocean $p\text{CO}_2$ at monthly and 0.25° resolutions. The reconstruction skill is evaluated against SOCATv2022 data from global to ocean basin scale and at the level of grid cells (Sect. 2.2). We compare the novel reconstruction at a higher spatial resolution to the one at a coarser spatial resolution (Chau et al., 2022b). Emphasis is put on the skill to reproduce spatial and temporal variations of $p\text{CO}_2$ across a variety of coastal regions and time series stations.

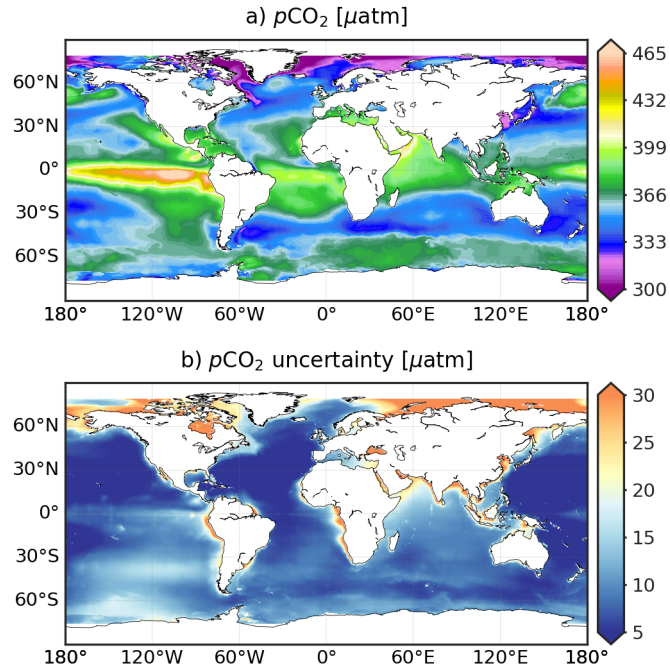


Figure 1. CMEMS-LSCE-FFNN $p\text{CO}_2$ over the global ocean at a spatial resolution of 0.25° . Temporal means of the model best estimate and 1σ -uncertainty per grid cell over 1985-2021 are calculated by using Eq. (5).

Table 3. Evaluation statistics for monthly CMEMS-LSCE-FFNN reconstructions of $p\text{CO}_2$ at 1° (r100) and 0.25° (r025) spatial resolutions computed over the period 1985-2021. r100 \rightarrow 025 and r025 \rightarrow 100 are referred to the versions downscaled or upscaled from the original CMEMS-LSCE-FFNN $p\text{CO}_2$ at 1° and 0.25° resolutions. SOCATv2022 gridded data independent from CMEMS-LSCE-FFNN training are used as benchmarks for model evaluation (see text for details). Statistics including total numbers of data, RMSD (Eq. 10), and r^2 (Eq. 11) are reported for both the open ocean (O) and coastal region (C). * marks results with respect to the primary product proposed in this study.

Basins			Number of data		RMSD [μatm]				r^2			
			r100	r025*	r100	r025 \rightarrow 100	r025*	r100 \rightarrow 025	r100	r025 \rightarrow 100	r025*	r100 \rightarrow 025
0.	Globe	(O)	207174	3317273	14.3	14.1	14.3	14.4	0.83	0.83	0.83	0.83
		(C)	101007	431758	26.6	26.5	27.6	28.5	0.72	0.72	0.74	0.72
1.	Arctic	(O)	537	8589	27.9	27.4	28.0	28.1	0.69	0.69	0.67	0.67
		(C)	5897	25844	38.7	38.6	41.5	43.2	0.55	0.56	0.55	0.52
2.	Atlantic	(O)	54797	876116	13.8	13.6	13.7	13.8	0.81	0.81	0.81	0.81
		(C)	49770	227665	25.0	24.8	25.2	26.1	0.76	0.76	0.77	0.77
3.	Pacific	(O)	120604	1932981	14.6	14.3	14.5	14.7	0.85	0.85	0.85	0.85
		(C)	26847	104269	26.8	26.9	28.5	29.0	0.71	0.71	0.69	0.67
4.	Indian Ocean	(O)	4485	71719	10.3	10.2	10.3	10.3	0.88	0.88	0.88	0.88
		(C)	1522	6187	23.5	22.8	25.4	26.5	0.69	0.71	0.69	0.69
5.	Southern Ocean	(O)	26751	427868	14.4	14.3	14.5	14.4	0.69	0.69	0.69	0.69
		(C)	16971	67793	26.0	25.8	27.4	28.8	0.61	0.61	0.64	0.59

320 Figure 1 presents global maps at 0.25° -resolution of long-term averages of $p\text{CO}_2$ and corresponding uncertainty estimates. Reconstructed $p\text{CO}_2$ distributions reveal well documented large scale structures. Values are high over upwelling regions (e.g., Equatorial Pacific, California Boundary Current, Western Arabian Sea). Low $p\text{CO}_2$ is associated with increased CO_2 solubility in cold high latitudes seawater (e.g., Arctic), strong biological production (e.g., China Sea), or the combination of both (e.g., subpolar Northern Atlantic, Southern Ocean between $35 - 50^\circ\text{S}$). Spatial structures appear coherent from small to large spatial
325 scales, both along the coast and moving towards the open ocean (see also in Figs. 2-4). The combination of a down-scaled version of open-ocean and higher-resolution coastal SOCATv2022 data (Sect. 2.1) yields $p\text{CO}_2$ distributions without discontinuities. The uncertainty map (Fig 1b) represents the confidence level in surface ocean $p\text{CO}_2$ estimates (Fig 1a). Predominantly low uncertainty estimates ($\sigma < 5 \mu\text{atm}$) indicate the global stability of the ensemble reconstruction. Exceptions are found in many coastal regions, open-ocean areas with sparse data coverage (e.g., Southern Pacific, Indian Ocean), or regions with sub-
330 stantially high or low surface ocean $p\text{CO}_2$ (e.g., Arctic, eastern equatorial Pacific). However, $p\text{CO}_2$ is reconstructed with a high degree of confidence over most of the global ocean with a σ -to- μ ratio (Eq. 8) below 10% (Fig. A9a).

Skill scores of the monthly, 0.25° -resolution reconstruction are presented in Table 3 (columns marked by an asterisk). The global RMSD (Eq. 10) between the best reconstruction and SOCATv2022r025 $p\text{CO}_2$ over the entire period is $14.3 \mu\text{atm}$ for the open ocean and $27.6 \mu\text{atm}$ for the coastal ocean. These two model errors are lower than 4% and 8% of the global mean $p\text{CO}_2$
335 (Table 6). Moreover, variability present in observation-based data is reproduced by the CMEMS-LSCE-FFNN with high values of r^2 (open ocean: 0.83, coast: 0.74). The reconstruction quality is similar among major ocean basins. Spatial distributions of SOCATv2022 data, bias, and RMSD are shown in Figs. A2-bd and A3-bdfh. Estimation skills are low in the ocean basins

with sparse data coverage and significant space-time variability of $p\text{CO}_2$ (e.g., Arctic, eastern Equatorial Pacific, land-ocean continuum).

340 Table 3 also presents statistics for the monthly FFNN products of surface ocean $p\text{CO}_2$ at spatial resolutions of 0.25° (r025) and 1° (r100) together with their variants (r100 \rightarrow 025 and r025 \rightarrow 100). The latter are respectively extrapolation and interpolation versions of the original r100 and r025 datasets. We used the Climate Data Operators (CDO) remap operator to regrid FFNN model outputs to a finer or coarser spatial resolution. For compatibility, we compare statistics between:

- i) FFNN(r025) and FFNN(r100 \rightarrow 025) by using SOCATv2022r025 as evaluation data,
- 345 ii) FFNN(r025 \rightarrow 100) and FFNN(r100) by using SOCATv2022r100 as evaluation data.

The FFNN(r025) central to this study yields a lower RMSD and a higher correlation to the SOCAT data than the FFNN(r100 \rightarrow 025). As expected, the improvement in reconstruction skill with higher model resolution is larger over coastal regions than in the open ocean. The FFNN(r025) product after interpolating to a coarser resolution, i.e., FFNN(r025 \rightarrow 100), agrees with the original 1° -resolution data product over all the ocean.

350 The motivation to increase the spatial resolution of the reconstruction is to improve the representation of horizontal gradients of $p\text{CO}_2$ at fine scales. Figures 2-4 exemplify spatial distributions for the two reconstructions (r025 and r100) over the coastal-open-ocean continuum. Ten distinct oceanic regions are considered (see Fig. A1a and Table A1 for the ten locations), which can be classified into three groups:

- permanent Eastern Boundary current upwelling systems with relatively high $p\text{CO}_2$ (California Current System - CCS, 355 Humboldt Current System - HCS, Canary Current System - CnCS, and Benguela Current System - BCS),
- regions characterized by low $p\text{CO}_2$ values driven by cold water temperatures and strong biological production (Labrador Sea, Western South Atlantic, Northern Europe, and Sea of Japan),
- other regions either under the influence of strong river runoff (Amazon mouth) or monsoon-driven upwelling (Western Arabian Sea).

360 The legend of Figs 2-4 includes regional RMSD and r^2 computed between the best estimates of two models and coastal-ocean SOCATv2022r025 data. The coarser spatial resolution product is co-located at the same 0.25° -grid cells for this analysis. These figures illustrate important discrepancies in $p\text{CO}_2$ data density between coastal regions with poorly monitored regions (e.g., HCS, BCS, Amazon mouth) contrasting with areas with higher data coverage (e.g., Northern Europe, Sea of Japan).

Over 7 out of the 10 analysed regions the reconstruction at monthly, 0.25° resolutions yields RMSDs below 10% of the 365 global mean of coastal-ocean $p\text{CO}_2$ estimates (Table 6) and r^2 values higher than 0.3; e.g., Northern Europe (RMSD = 32.4 μatm , $r^2 = 0.81$), Sea of Japan (RMSD = 20.8 μatm , $r^2 = 0.71$), and CnCS (RMSD = 28.8 μatm , $r^2 = 0.4$). The CMEMS-LSCE-FFNN model projections of $p\text{CO}_2$ lack skill over the HCS (RMSD = 50.0 μatm , $r^2 = 0.33$), the region under influence of the Amazon river (RMSD = 45.7 μatm , $r^2 = 0.38$), and the Western Arabian Sea (RMSD = 44.8 μatm , $r^2 = 0.49$). In nearshore sectors of these coastal areas, $p\text{CO}_2$ estimates are also subject to a substantial amount of uncertainty ($\sigma > 20 \mu\text{atm}$).

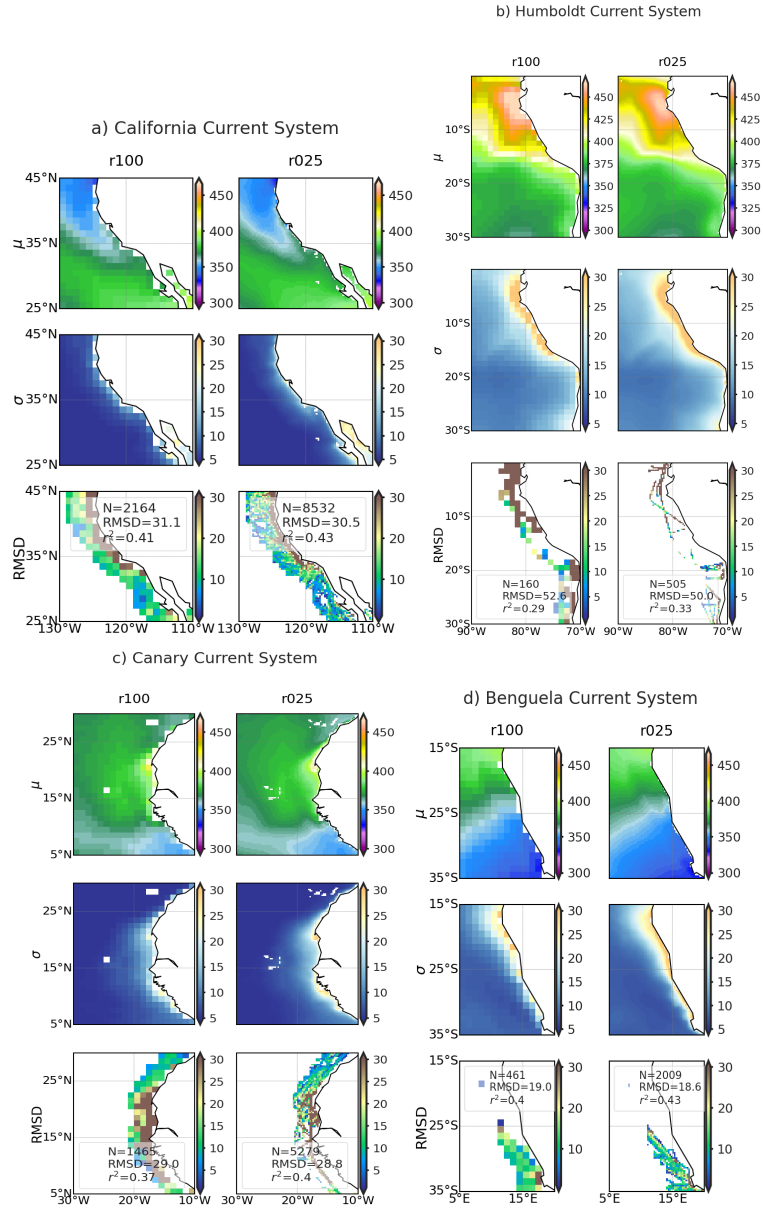


Figure 2. Comparison of CMEMS-LSCE-FFNN mapping $p\text{CO}_2$ at 1° (r100) and 0.25° (r025) resolutions over 4 permanent upwelling regions associated with the Eastern Boundary Currents (California, Humboldt, Canary, and Benguela; see Figure A1-ABGH for geographical locations). For each region, spatial distributions of $p\text{CO}_2$ (μ) and uncertainty (σ) estimates, and coastal-ocean RMSD of $p\text{CO}_2$ averaged over 1985-2021 (Eqs. 5 and 10) are shown. Metrics presented in the legend for each of the 3rd row include the number of coastal-ocean SOCATv2022 data (N), regional RMSD (Eq. 10) and r^2 (Eq. 11).

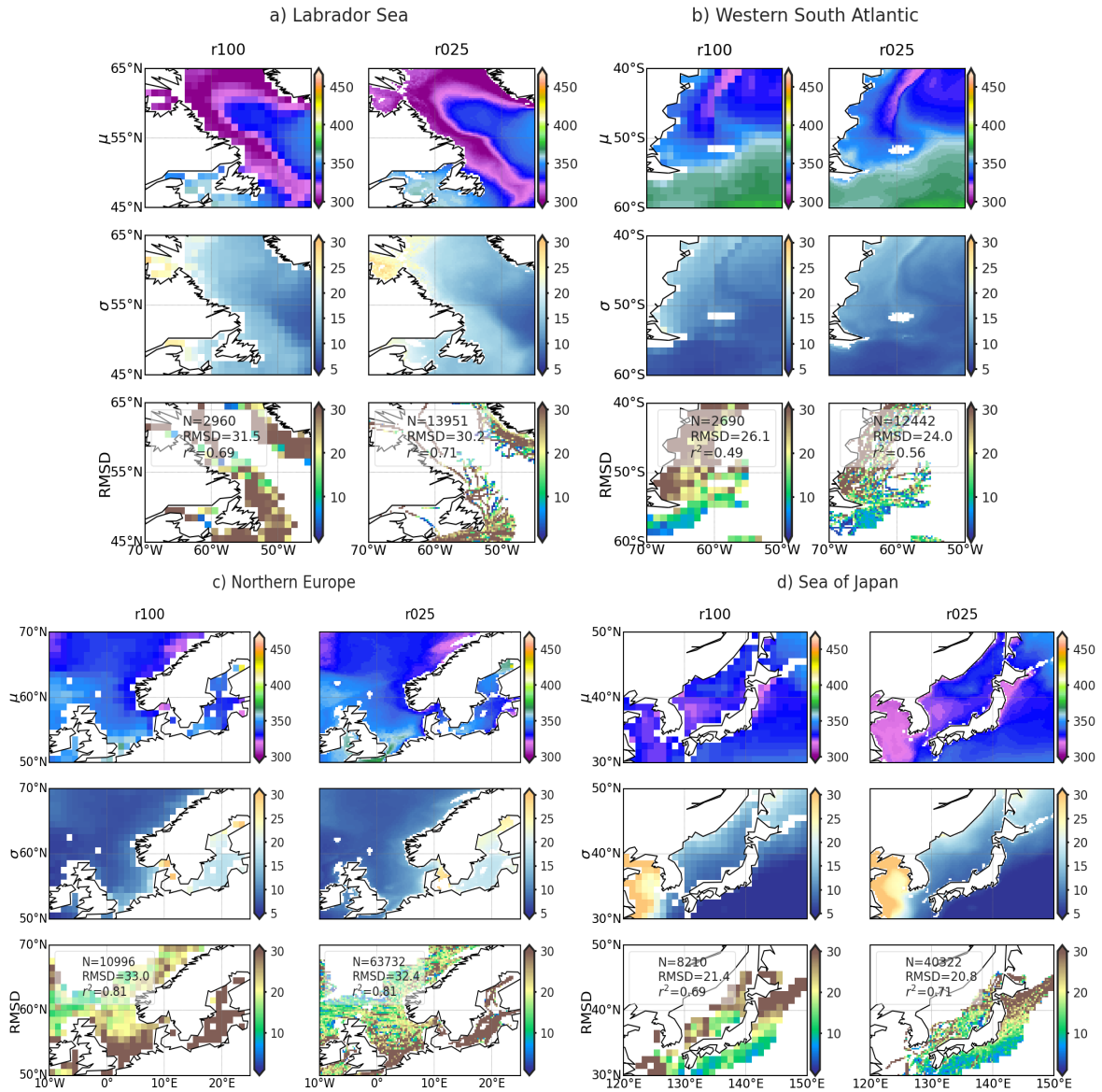


Figure 3. Comparison of CMEMS-LSCE-FFNN mapping $p\text{CO}_2$ at 1° (r100) and 0.25° (r025) resolutions over 4 regions characterized with low $p\text{CO}_2$ values (Labrador, Western South Atlantic, Northern Europe, and Japan; see Figure A1-CEFJ for geographical locations). For each region, spatial distributions of $p\text{CO}_2$ (μ) and uncertainty (σ) estimates, and coastal-ocean RMSD of $p\text{CO}_2$ averaged over 1985-2021 (Eqs. 5 and 10) are shown. Metrics present in the legend for each of the 3rd row include the number of coastal-ocean SOCATv2022 data (N), regional RMSD (Eq. 10) and r^2 (Eq. 11).

370 The lack of model skill reflects the combination of low data density and strong $p\text{CO}_2$ gradients driven by multiple underlying physical and biogeochemical processes. The HCS, for instance, is characterized by the highest $p\text{CO}_2$ levels (Fig. 2) among the

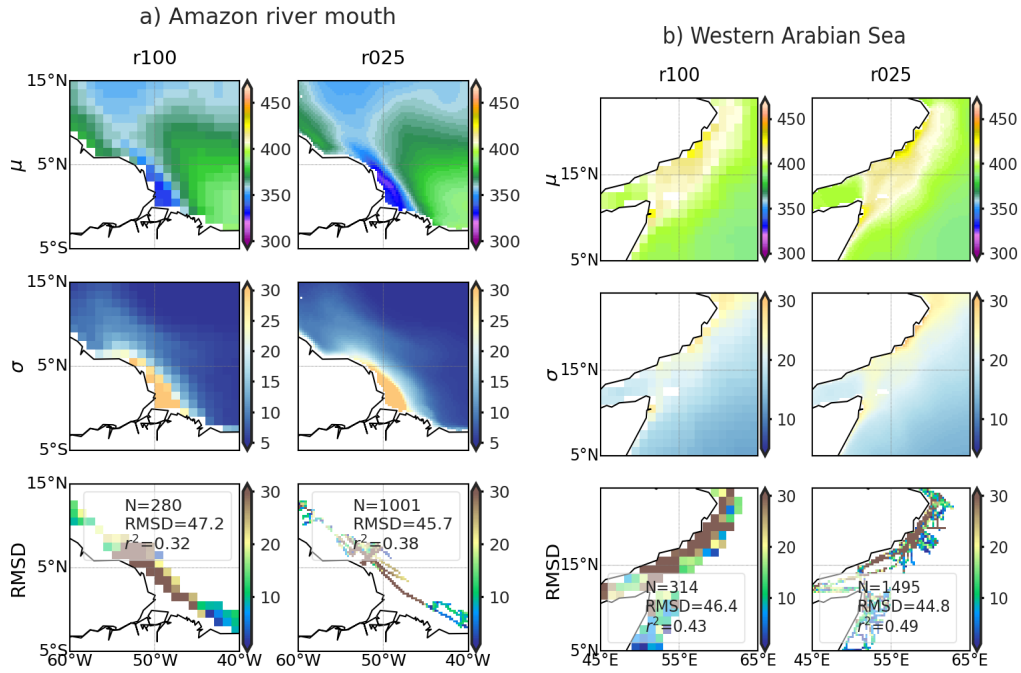


Figure 4. Comparison of CMEMS-LSCE-FFNN mapping $p\text{CO}_2$ at 1° (r100) and 0.25° (r025) resolutions over the mouth of the river Amazon and the Western Arabian Sea (see Fig. A1-DI for geographical locations). For each region, spatial distributions of $p\text{CO}_2$ (μ) and uncertainty (σ) estimates, and coastal-ocean RMSD of $p\text{CO}_2$ averaged over 1985-2021 (Eqs. 5 and 10) are shown. Metrics present in the legend for each of the 3rd row include the number of coastal-ocean SOCATv2022 data (N), regional RMSD (Eq. 10) and r^2 (Eq. 11).

four Eastern Boundary Current Systems, with interannual variability amplified with the El Niño–Southern Oscillation (ENSO) events (Feely et al., 1999; Landschützer et al., 2016). Similarly, high $p\text{CO}_2$ levels with substantial seasonal variability are observed over the Western Arabian Sea (Fig. 4b), the key driver being monsoonal upwelling (Sabine et al., 2002; Sarma et al., 2013, 2023). In contrast to the two aforementioned coastal regions, high CO_2 undersaturation as well as strong $p\text{CO}_2$ gradients (Fig. 4a) are found in the area under the influence of Amazon river discharge (Olivier et al., 2022). Extreme values and large variability of $p\text{CO}_2$ challenge any approach to estimate $p\text{CO}_2$ data over these regions (Ibáñez et al., 2015; Bakker et al., 2016; Landschützer et al., 2020).

The two FFNN reconstructions (r025 and r100) share similarities in overall structures of $p\text{CO}_2$ over the coastal-open-ocean continuum (Figs. 2-4). However, the higher spatial resolution outperforms its lower resolution counterpart in reproducing fine-scale features of $p\text{CO}_2$ in the transition from nearshore regions to the adjacent open ocean. The increase in model spatial resolution translates into a greater spatial coverage of the continental shelves such as Labrador Sea, Northern Europe, and Sea of Japan (Fig. 3), and thus an increase in the number of data over the coastal domain. The increase in spatial resolution allows a gain in prediction probability of $p\text{CO}_2$ variations on the order of roughly 2% over the Eastern Boundary Currents to 7% over the Western South Atlantic (Figs. 2-3b).

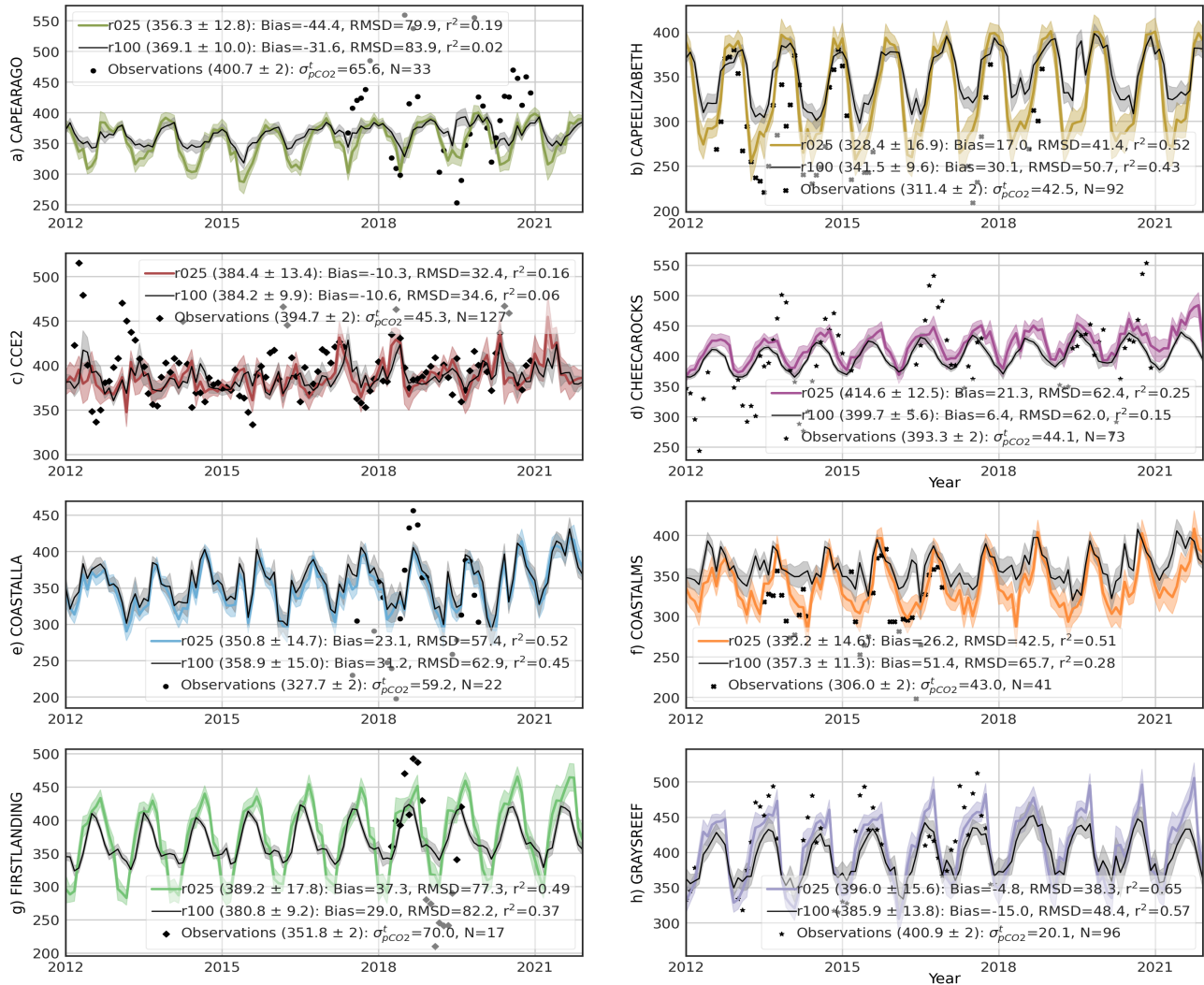


Figure 5. Time series of surface ocean $p\text{CO}_2$ (μatm) at coastal observing stations (Table A2 and Fig. A1b): model best estimate (curve), 1σ -uncertainty (envelope), and monthly average of in situ observations (point). The reconstructed data at 1° (r100) and 0.25° (r025) resolutions are co-located to in situ observations provided by Sutton et al. (2019). Means of the best estimate and 1σ -uncertainty ($\mu \pm \sigma$) calculated over the observing time span are shown in brackets. Statistics include number of months with observations (N), Bias, RMSD, and r^2 computed for the two reconstructions. $\sigma_{p\text{CO}_2}^t$ stands for temporal standard deviation from monthly averages of $p\text{CO}_2$ observations.

At local scale, the reconstruction of in situ $p\text{CO}_2$ (Sutton et al., 2019) over the open ocean is at the high order of confidence (Table A3). Low RMSD (between 7.8 and 23.5 μatm) and sustainably high r^2 (from 0.45 to 0.98) dominate evaluation statistics over the 18 open-ocean stations. Obviously, CMEMS-LSCE-FFNN has less skill in the coastal sector and model-observation deviation varies depending on a wide range of $p\text{CO}_2$ conditions. However, coastal-ocean RMSD can be smaller

390 than 10% of station climatology (e.g., KILONALU, KANEOHE, ALAWAI) and the reproduction availability of temporal variations of $p\text{CO}_2$ possibly exceeds 70% (e.g., SEAK, KODIAK, DABOB). Through Fig. 5, we further assess seasonal to inter-annual variability reproduced at the eight coastal sites (see Fig. A1b and Table A2 for station location) where measurements are available for both $p\text{CO}_2$ and $p\text{H}$ (analyzed in Section 5.3) and they are poorly constrained by the 1° -reconstruction (Chau et al., 2022b). The temporal variability of $p\text{CO}_2$ reported for these time series sites reflects a combination of processes
395 (Sutton et al., 2019), e.g., California Current System (CAPEARAGO and CCE2), western coastal upwelling (CAPEELIZABETH), eutrophication enhancing respiration of CO_2 (FIRSTLANDING), and multiple stressors on coral reef environments (CHEECAROCKS, GREYREEF). As shown in Fig. 5 (scattered points for observations) time series of coastal $p\text{CO}_2$ are still short. The longest time series covers 127 months of $p\text{CO}_2$ monitoring since 2010 (CCE2) while the shortest one contributes 17 months with observations (FIRSTLANDING).

400 Analyzing the station time series, we have found that data have been sampled within a few days with an average offset of about a week from the month center. At these coastal sites, the temporal standard deviation from monthly averages of $p\text{CO}_2$ ($\sigma_{p\text{CO}_2}^t$) exceeds analytical errors ($2 \mu\text{atm}$, Sutton et al., 2019). $\sigma_{p\text{CO}_2}^t$ ranges from $20.1 \mu\text{atm}$ at GREYREEFF to values as large as $65.6 \mu\text{atm}$ at CAPEARAGO or $70 \mu\text{atm}$ at FIRSTLANDING. The monthly average of $p\text{CO}_2$ might not be adequately represented by discrete samples at sites with a large temporal standard deviation of $p\text{CO}_2$. The misfit between
405 the monthly reconstruction and discrete observations is exacerbated in dynamical coastal environments and might explain in part the large RMSD of reconstructions of monthly coastal $p\text{CO}_2$ (e.g., GREYREEFF: $38.3 \mu\text{atm}$, CAPEARAGO: $79.9 \mu\text{atm}$, FIRSTLANDING: $77.3 \mu\text{atm}$) for the $r025$ reconstruction. The RMSD is mostly lower for the FFNN reconstruction at 0.25° resolution compared to the FFNN at 1° resolution by $2.2 \mu\text{atm}$ (CCE2) to $23.2 \mu\text{atm}$ (COASTALMS). Similarly, r^2 increases between 7%-23% at higher resolution. Overall, seasonal to interannual variations of coastal-ocean $p\text{CO}_2$ are better reproduced
410 in the reconstruction at 0.25° resolution (Fig. 5).

5.2 Total alkalinity and dissolved inorganic carbon

This section presents and analyses global ocean surface reconstructions of total alkalinity (A_T) and dissolved inorganic carbon (DIC) at monthly, 0.25° resolutions over 1985-2021. GLODAPv2.2022 bottle data (Sect. 2.2) serve as reference data for model evaluation. Model reconstruction skill is further assessed at the eight Eulerian time series sites: AWIPEV, BATS, DYFAMED,
415 ESTOC, HOT, ICELAND, IRMINGER, and KERFIX (Table 2).

Figure 6 shows spatial distributions of the climatological mean and uncertainty (Eq. 5) for A_T and DIC. Despite being in part influenced by common biological and physical processes, both properties have contrasting distributions due to the strong correlation between surface ocean A_T and salinity (Lee et al., 2006; Broullón et al., 2019), as well as the contribution of air-sea gas exchange and biological productivity on surface ocean DIC levels (Feely et al., 2001; Takahashi et al., 2014). Over subtropical
420 Atlantic gyres and the Mediterranean Sea, oceanic areas with net evaporation, A_T exceeds $2400 \mu\text{mol kg}^{-1}$. Total alkalinity falls below $2150 \mu\text{mol kg}^{-1}$ in regions where precipitation, river freshwater runoff, or seasonal sea-ice melting dilute surface water salinity (e.g., subpolar North Pacific, Arctic, and equatorial river outflows). The distribution of DIC is relatively uniform between the Atlantic, Pacific, and Indian Ocean basins, but shows pronounced latitudinal gradients. High concentrations of

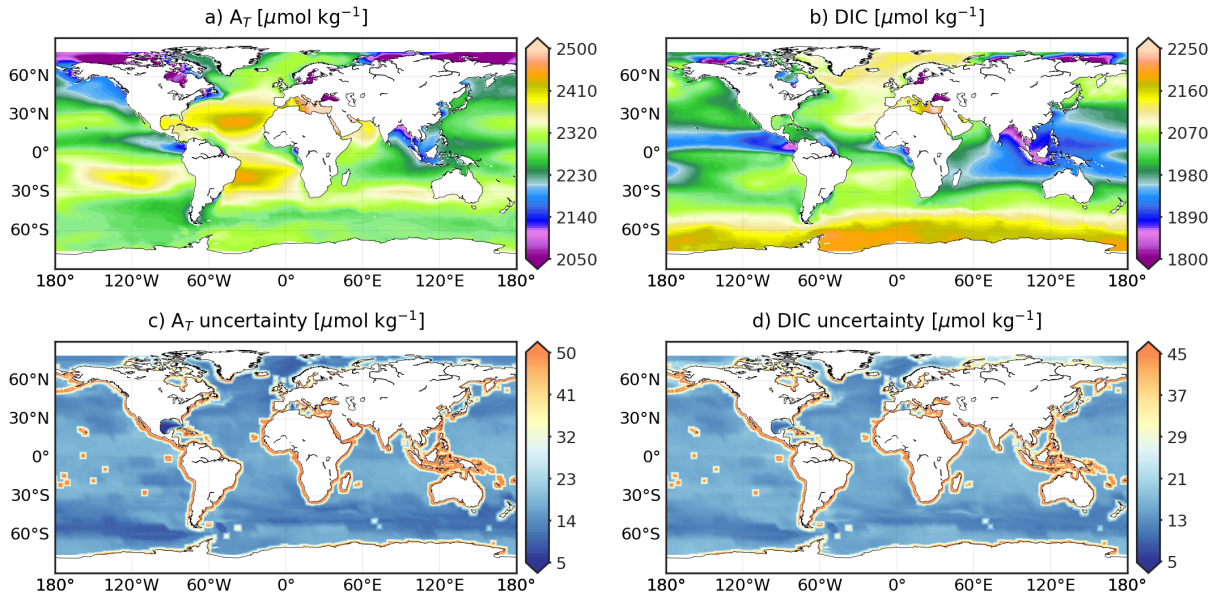


Figure 6. CMEMS-LSCE A_T and DIC over the global ocean at a spatial resolution of 0.25° . Temporal means of the model best estimate and 1σ -uncertainty per grid cell over 1985-2021 are calculated by using Eq. (5).

DIC are found throughout the Southern Ocean ($DIC > 2100 \mu\text{mol kg}^{-1}$) where strong upwelling brings up subsurface water enriched in CO_2 and nutrients. The inefficient utilization of nutrients in this high nutrient low chlorophyll region limits the biological drawdown of DIC allowing the massive DIC input to be spread horizontally by westerlies (Key et al., 2004; Men-
 425 viel et al., 2018). Levels of DIC below $1900 \mu\text{mol kg}^{-1}$ are reconstructed over the Equatorial Pacific, the Equatorial Eastern Atlantic, the Eastern Indian Ocean, and coastal areas on the Arctic Ocean. While low DIC levels associated with Equatorial upwelling reflect gas exchanges across the air-sea interface and enhanced biological production, the interaction between physical
 430 and biogeochemical processes at work in the Indian Ocean are less well understood (Takahashi et al., 2014). Low DIC levels found close to river mouths reflect outgassing of CO_2 across the salinity gradient, as well as enhanced biological uptake fueled by river nutrient inputs. Representation uncertainty (Fig. 6-cd) associated with monthly alkalinity and DIC reconstructions is lower than $20 \mu\text{mol kg}^{-1}$ throughout the open ocean. The open-ocean σ -to- μ ratio (Eq. 8) ranges between $0.5 - 1.5\%$ which is relatively small (Fig. A9-cd). DIC uncertainty is computed through CO_2SYS error propagation with reconstruction uncertain-
 435 ties of $p\text{CO}_2$ and A_T set as inputs. The largest values ($\sigma > 30 \mu\text{mol kg}^{-1}$) appear nearshore and surrounding oceanic islands (Fig. 6d). A similar feature is found on the field of A_T (Fig. 6c) inherited from input uncertainty associated with the CMEMS salinity product (Fig. A7a).

We qualify monthly, 0.25° reconstructions of A_T and DIC with GLODAPv2.2022 data (Lauvset et al., 2022a) for the 37-year period (Table 4 and Fig. 8). The global open-ocean reconstruction scores a RMSD of $22.1 \mu\text{mol kg}^{-1}$ and a r^2 of 0.9 in
 440 A_T . Similar numbers are found for DIC (RMSD= $22.7 \mu\text{mol kg}^{-1}$ and $r^2 = 0.9$). The model scores the good fit in the open

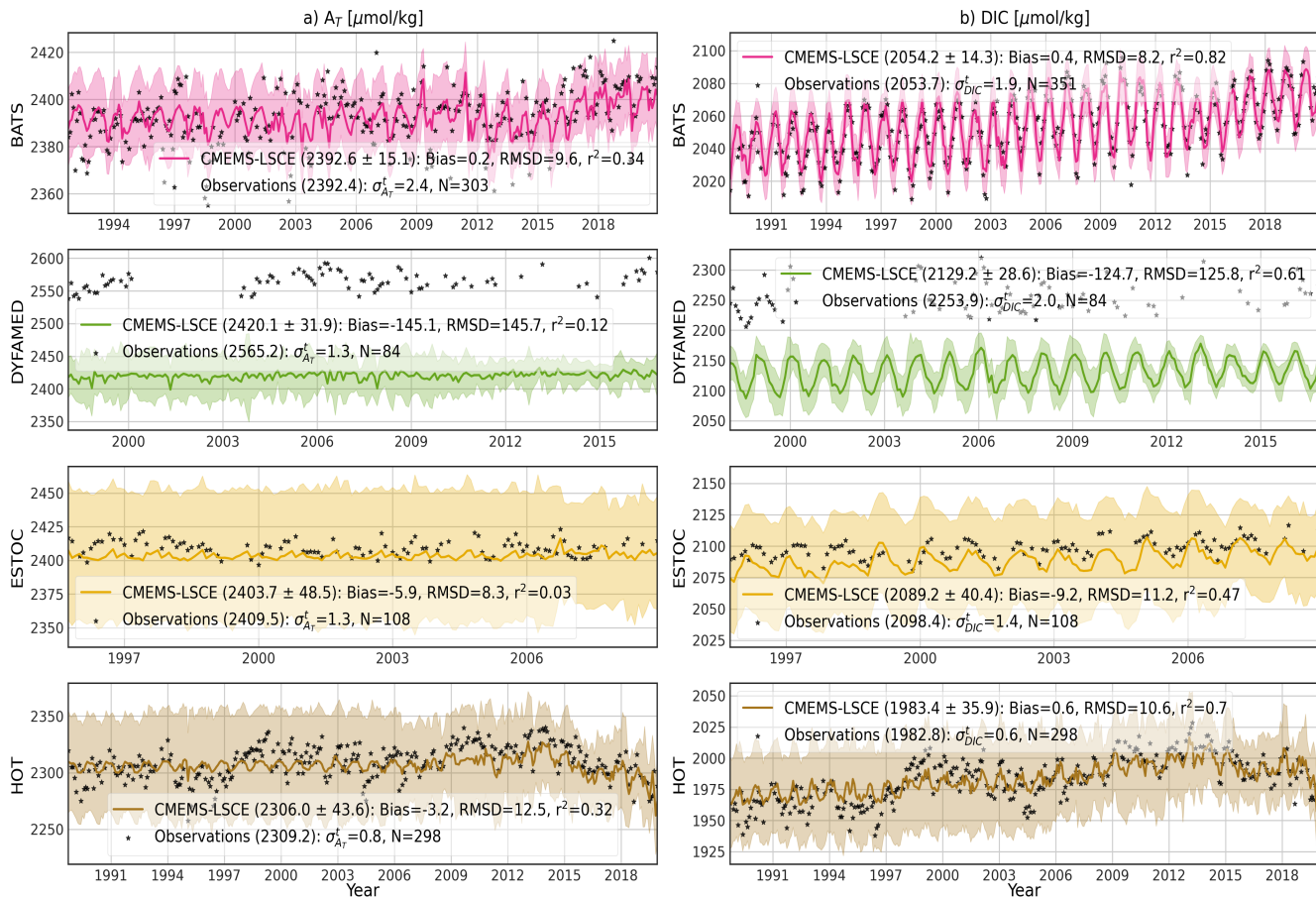


Figure 7. Monthly time series of A_T and DIC at BATS, DYFAMED, ESTOC and HOT stations (Table 2 and Fig. A1b): model best estimate (curve), 1σ -uncertainty (envelope), and monthly average of surface (0-10 m) observations (point). Means of the best estimate and 1σ -uncertainty ($\mu \pm \sigma$) calculated over the observing time span are shown in brackets if accessible. Statistics include number of months with observations (N), Bias, RMSD, and r^2 . $\sigma_{A_T}^t$ [σ_{DIC}^t] stands for temporal standard deviation from monthly averages of A_T [DIC] observations.

Indian Ocean with RMSD smaller than $15.5 \mu\text{mol kg}^{-1}$ and r^2 above 0.92 for both variables. The reconstruction deviates from GLODAP data in the western North Atlantic, subpolar North Pacific, tropics, and nearby major rivers (Fig. 8-abcd).

A_T and DIC are underestimated in the continental shelves of north Alaska and the northeastern Atlantic, the Mediterranean Sea, South China Sea, and nearby river plumes (Fig. 8-ac). The Arctic yields the poorest estimations among all the ocean basins with a global RMSD over $100 \mu\text{mol kg}^{-1}$ (Table 4). The prediction probability of variability in A_T [DIC] is relatively large for the open ocean 79% [71%], but rather unsatisfying over the coastal ocean (46% [40%]). Extrapolating these carbonate variables towards the shore remains challenging with much higher errors and uncertainty estimates obtained over the continental shelf compared to the open-ocean reconstruction (Table 4, Figs. 6-cd and . 8-abcd). The coastal-ocean errors are on the order of 10% of the global mean values of A_T and DIC (Table 6).

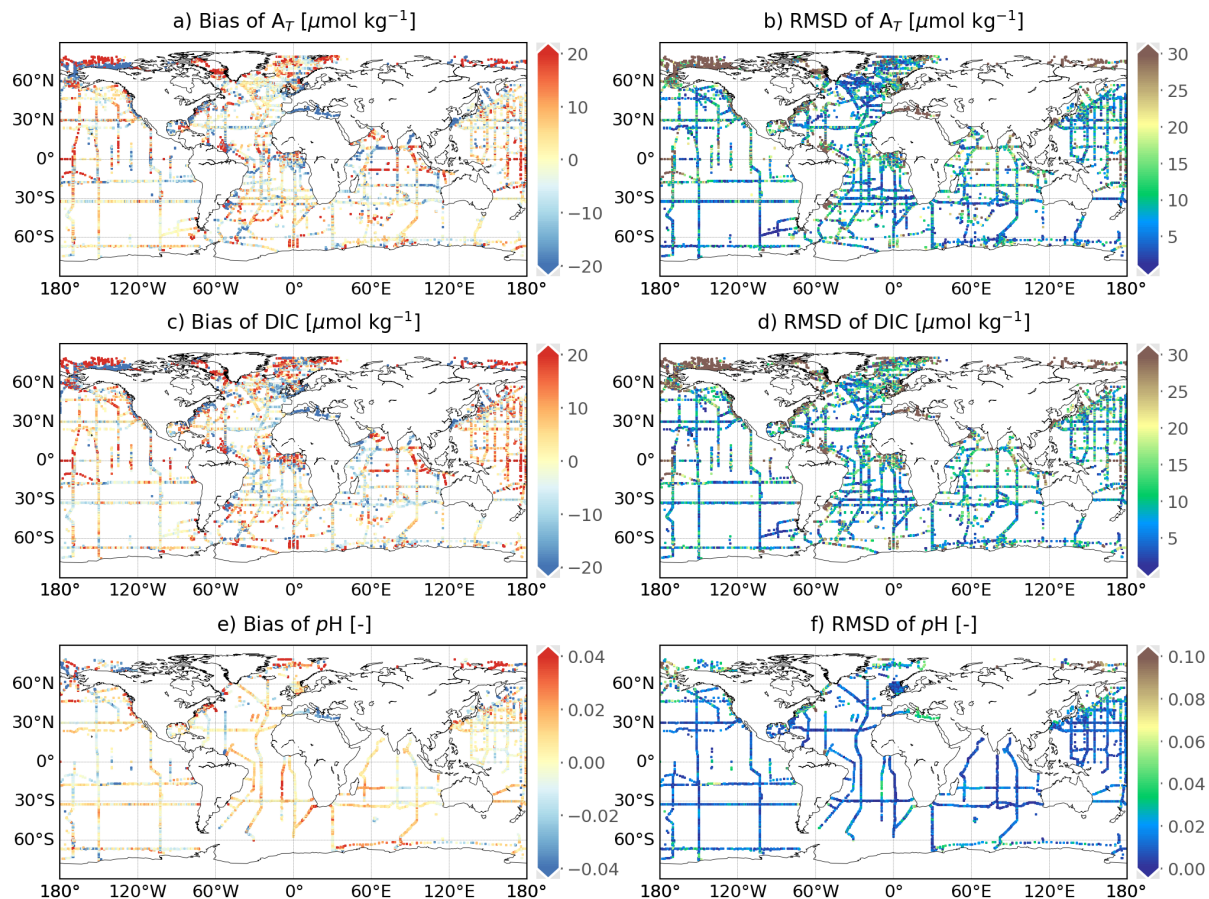


Figure 8. Spatial distribution of reconstruction skills for A_T , DIC, and pH over 1985-2021. Mean model-data difference (Bias) and root-of-mean square-deviation (RMSD) between the reconstruction and GLODAPv2.2022 surface data (0-10 m) at a spatial resolution of 0.25° . The size of grid cells is scaled upon a better visualization.

450 The reconstruction of A_T distributions relies on LIAR coefficients fit with GLODAPv2 data (Olsen et al., 2016) covering the years before 2015. These data are also part of the latest version GLODAPv2.2022 (Lauvset et al., 2022a). They do therefore not correspond to an independent dataset for the evaluation data of the CMEMS-LSCE reconstruction. To accomplish a cross-validation, reconstructions of A_T and DIC are compared to observations for eight time series stations: AWIPEV, BATS, DYFAMED, ESTOC, HOT, ICELAND, IRMINGER, and KERFIX (see Table 2 and Fig. A1b for data sources and station locations). Table A4 presents the evaluation statistics for all the stations and Figure 7 illustrates the comparison between monthly time series of A_T and DIC extracted from the CMEMS-LSCE datasets and measurements at the four sustained long-term monitoring sites. More than 270 [80] months in the years 1988-2021 [1995-2009 and 1998-2017] include measurements of A_T and DIC at BATS and HOT [ESTOC and DYFAMED]. As shown in Table A4, the Arctic site (AWIPEV) provides 52-month data in 2015-2020 while the three other stations sparsely observed A_T and DIC at the surface layer resulting in fewer than 30 monthly

455

Table 4. Skill scores computed between CMEMS-LSCE and GLODAPv2.v2022 in A_T , DIC, and pH over the period 1985-2021. Total numbers of data, RMSD (Eq. 10), and r^2 (Eq. 11) are reported for both the open ocean (O) and coastal region (C). Basin identification is shown in Fig. A1.

Basins			Number of data		A_T [$\mu\text{mol kg}^{-1}$]		DIC [$\mu\text{mol kg}^{-1}$]		pH [-]	
					RMSD	r^2	RMSD	r^2	RMSD	r^2
0.	Globe	(O)	10269	(5411)	22.1	0.90	22.7	0.90	0.022	0.70
		(C)	6309	(2080)	82.0	0.72	72.4	0.62	0.060	0.45
1.	Arctic	(O)	103	(26)	107.1	0.79	113.3	0.71	0.106	0.32
		(C)	1635	(300)	148.7	0.46	126.8	0.4	0.107	0.48
2.	Atlantic	(O)	2785	(932)	30.1	0.74	28.7	0.72	0.028	0.58
		(C)	2422	(941)	44.5	0.71	39.1	0.69	0.046	0.45
3.	Pacific	(O)	4539	(3222)	13.6	0.92	16.0	0.92	0.019	0.74
		(C)	1380	(639)	28.4	0.76	44.4	0.45	0.057	0.34
4.	Indian Ocean	(O)	1177	(551)	15.1	0.92	13.8	0.96	0.012	0.90
		(C)	328	(62)	16.6	0.92	22.0	0.90	0.013	0.82
5.	Southern Ocean	(O)	1665	(680)	11.0	0.64	13.2	0.92	0.019	0.68
		(C)	544	(138)	22.5	0.50	24.5	0.77	0.023	0.65

460 mean data in 2014-2021 (IRMINGER and ICELAND) and 1992-2018 (KERFIX). The reconstructed time series fit monthly averages of in situ measurements well. Mean estimates of A_T [DIC] over the observing period are about 2283 [1983] $\mu\text{mol kg}^{-1}$ at KERFIX [HOT] to 2420 [2219] $\mu\text{mol kg}^{-1}$ at DYFAMED [AWIPEV]. At all the stations (DYFAMED and AWIPEV excepted) and for the two variables, model-observation misfit is small (Bias $< 11 \mu\text{mol kg}^{-1}$, RMSD $< 14 \mu\text{mol kg}^{-1}$) relative to the aforementioned mean estimates (Table A4). The highest offset between the CMEMS-LSCE estimation and observations for all 465 the stations is found at DYFAMED (A_T : $-145.1 \mu\text{mol kg}^{-1}$, DIC: $-124.7 \mu\text{mol kg}^{-1}$). DYFAMED provides long-term time series of A_T and DIC measurements in the Northwestern Mediterranean Sea (Fig. A1b). Salinity and alkalinity have substantial values due to the net evaporation (Coppola et al., 2020). The average of A_T in the Mediterranean Sea exceeds that for the global ocean by 10% (Palmiéri et al., 2015). These characteristics set the Mediterranean Sea aside from the ocean basins. Although the bias between reanalysed SSS and observations (Fig. A10) is relatively small, LIAR (Carter et al., 2018) was trained on 470 GLODAPv2 (Olsen et al., 2016) including only few observations in this area. The distinct relationship between alkalinity and salinity prevailing in the Mediterranean Sea is likely not reproduced by LIAR leading to an underestimation of A_T and a systematic bias to DIC at DYFAMED (Fig. 7). ESTOC is located close to the North Atlantic east coast and under the influence of the Canary Current System (CCS, Fig. A1). Spatial gradients and temporal variability are higher in the CCS (Fig. 2c) compared to BATS and HOT which are both located in the center of subtropical gyres. Despite showing good estimates of A_T and 475 DIC in RMSD at ESTOC, temporal variability of observations are reconstructed with the lowest r^2 (Table A4). Particularly, seasonality to multi-year variations in DIC are predicted at $r^2 = 0.47$ for ESTOC compared to $r^2 > 0.7$ for AWIPEV, ICE-

LAND, IRMINGER, BATS and HOT. Over all the stations, the model underestimates temporal changes of A_T (Fig. 7a; BATS: $r^2 = 0.33$, DYFAMED: $r^2 = 0.12$, ESTOC: $r^2 = 0.03$, HOT: $r^2 = 0.32$) which can be attributed to the large discrepancy in variability between in situ measurements and the CMEMS time series of salinity (Fig. A10a; BATS: $r^2 = 0.33$, DYFAMED: $r^2 = 0.19$, ESTOC: $r^2 = 0.03$, HOT: $r^2 = 0.35$). Model uncertainty (1σ -envelop) of monthly A_T and DIC estimates (Fig. 7a) is also inflated somewhat proportional to the CMEMS salinity product uncertainty (Fig. A10a).

5.3 Surface ocean pH and saturation state with respect to carbonate minerals

Surface ocean pH and saturation states with respect to aragonite (Ω_{ar}) and calcite (Ω_{ca}) are critical indicators used to measure ocean acidification. This section first presents an overall evaluation of these variables. We then introduce estimates involved in the monitoring of ocean acidification in 1985-2021 as an essential application of the CMEMS-LSCE surface ocean carbon product.

5.3.1 General analysis and evaluation

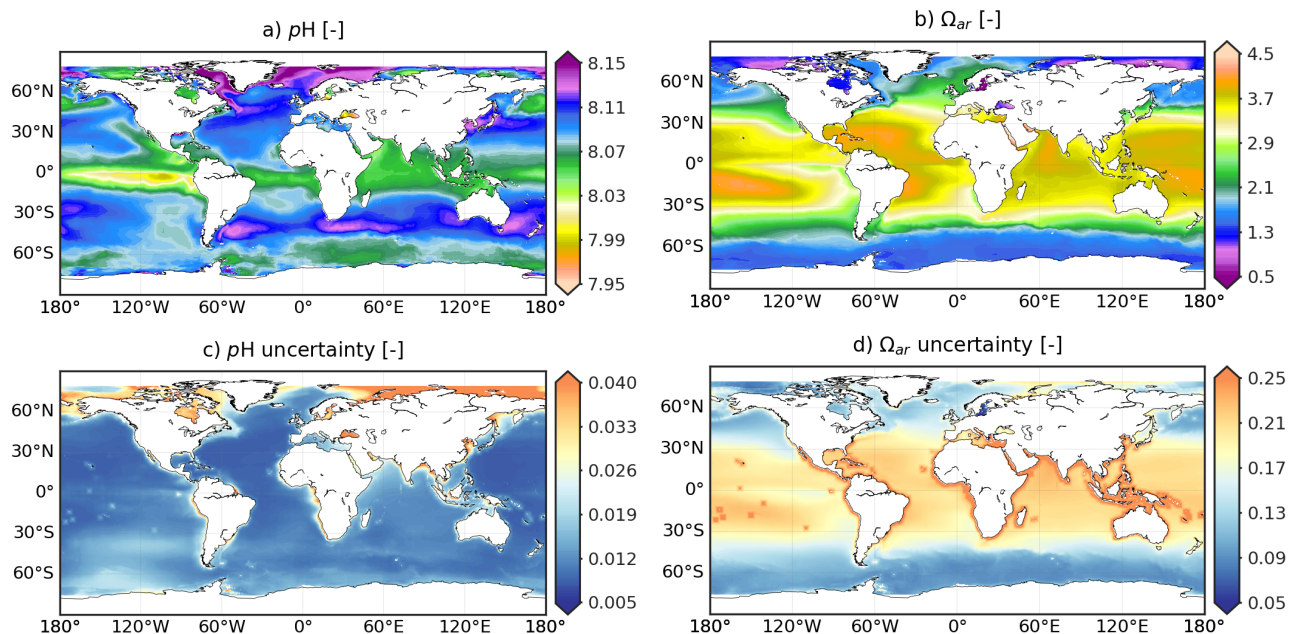


Figure 9. CMEMS-LSCE pH and Ω_{ar} over the global ocean at a spatial resolution of 0.25° . Temporal means of the model best estimate and 1σ -uncertainty per grid cell over 1985-2021 are calculated by using Eq. (5).

The spatial distribution of surface ocean pH reported on total hydrogen ion (H^+) scale is shown in Fig. 9 (the corresponding figure for H^+ , Fig. A4, is included in the supplementary). Both temporal means of the best model estimate and 1σ -uncertainty of pH share spatial patterns with pCO_2 (Fig. 1). Variables pH and pCO_2 correlate closely through equilibrium relationships of

dissolved CO₂ in seawater: an increase in $p\text{CO}_2$ generally corresponds to a decrease in $p\text{H}$. The distribution of the climatological mean of $p\text{H}$ displays a gradient with latitude between 8.03 and 8.11 $p\text{H}$ units across most of the basins (Fig. 9a). Values of $p\text{H}$ below 8 are associated with the upwelling of CO₂-rich waters (e.g., Eastern Equatorial Pacific, Western Arabian Sea). $p\text{H}$ exceeds 8.15 in sub- and polar cold surface water and in the regions with high biological productivity (e.g. Labrador Sea, Nordic Seas, Southern Ocean between 35°S-50°S).

The saturation state of surface ocean waters with respect to calcium carbonate minerals aragonite and calcite is defined as the ratio of the product of the concentrations of calcium ions (Ca²⁺) and carbonate ions (CO₃²⁻) to the solubility of the respective calcium carbonate mineral (CaCO₃) in surface seawater. Aragonite being the more soluble polymorph, its degree of saturation (Ω_{ar}) is smaller than that of calcite (Ω_{ca}) (Mucci, 1983). With the exception of this offset, the spatial distributions of their climatological means share common spatial patterns over the global ocean (Figs. 9b and A5a). Surface seawater is generally supersaturated, i.e., Ω_{ar} and Ω_{ca} greater than 1. The magnitude of surface ocean calcium carbonate saturation state varies with latitude. Values as large as 3.7-4.5 [5-7] for aragonite [calcite] are reconstructed in subtropical and tropical regions. Ω_{ar} and Ω_{ca} decrease toward the poles. In the Southern Ocean, surface seawater enriched in CO₂ from vertical mixing has Ω_{ar} [Ω_{ca}] values in the range of 1.5-2.1 [2-3.4]. Low saturation states are also computed in the Arctic and for waters of upwelling regimes (Fig. 9b). Locally Ω_{ar} drops below 1.3, and even fall under the CaCO₃ dissolution threshold of 1 (Gattuso and Hansson, 2011) in the Arctic water runoff and Baltic sea.

The uncertainty (1 σ) of $p\text{H}$, Ω_{ar} , and Ω_{ca} propagated the speciation of the CO₂ system takes into account the ensemble spread of $p\text{CO}_2$ estimates and analysis errors of other variables (Sect. 3.3). Monthly $p\text{H}$ uncertainty estimates fall in the 95% confidence interval of [0.008, 0.036] with a global mean value of 0.011. These estimates are in close agreement with the global uncertainty between 0.01-0.022 $p\text{H}$ units calculated by Jiang et al. (2019), Iida et al. (2021), and Gregor and Gruber (2021). $p\text{H}$ uncertainty is typically larger than 0.03 in the Arctic and in coastal regions (Figs. 9c). In contrast, the reconstructions of Ω_{ar} and Ω_{ca} are subject to high uncertainty ($\sigma > 0.175$) between 30°S-30°N (Fig. 9d and A5b). Regarding the σ -to- μ ratio, mean uncertainty estimates per cell for the saturation states in the (sub-) tropical band are relatively small compared to the mean of the best monthly estimates (Figs. A9-ef). The Arctic and the coastal oceans remain the regions with largest reconstruction uncertainties for Ω_{ar} and Ω_{ca} , as well as for $p\text{CO}_2$ and $p\text{H}$ (Figs. A9-ab). Excluding these regions, $R(\sigma, \mu)$ (Eq. 8) is less than 0.3% for $p\text{H}$ and 8% for Ω_{ar} and Ω_{ca} .

The monthly CMEMS-LSCE reconstruction at 0.25° resolution is assessed against $p\text{H}$ measurements from GLODAPv2.2022 bottle data (Table 2). For the period 1985-2021, the global RMSD amounts to 0.022 [0.060] $p\text{H}$ units and r^2 scores at 0.70 [0.45] over the open [coastal] ocean (Table 4). Model bias lies within [-0.01, 0.01] $p\text{H}$ units and RMSD is below 0.02 $p\text{H}$ units over the open ocean, except for high latitudes over 60° (Figs. 8-ef). At local scale, the time series from Sutton et al. (2019) are used for further evaluation (Tables A2 and A3). There exists much fewer evaluation data for $p\text{H}$ than for $p\text{CO}_2$, e.g., only 2 months of monitoring $p\text{H}$ at COASTALLA and FIRSLANDING or devoid of $p\text{H}$ measurements at equatorial observing systems. CMEMS-LSCE reconstructs $p\text{H}$ over the open ocean with rather high scores, e.g., at BOBOA (RMSD = 0.011 and $r^2 = 0.71$) and KEO (RMSD = 0.014 and $r^2 = 0.86$). Referring to the eight coastal sites evaluated for $p\text{CO}_2$ in Section 5.1, RMSD can be as small as 0.035 and 0.04 $p\text{H}$ units at CCE2 and GRAYSREEF while it is over 0.05 $p\text{H}$ units at the other

stations (e.g., COASTALLA: 0.068, CAPEARAGO: 0.069). Similar to the $p\text{CO}_2$ time series (Fig. 5, Sect. 5.1), $p\text{H}$ has been monitored with low sampling frequency (roughly few days in the tracking month) and the temporal sampling deviation of instantaneous observations from monthly averages ($\sigma_{p\text{H}}^t$) is significant. This temporal sampling uncertainty of $p\text{H}$ contributes to the mismatch between model estimates and observations. For example, $\sigma_{p\text{H}}^t$ amounts to 0.048 $p\text{H}$ units at CCE2 and 0.020 $p\text{H}$ units at GRAYSREEF, and reaches highest values of 0.078 $p\text{H}$ units at COASTALLA and 0.086 $p\text{H}$ units at CAPEARAGO. Although model-observation misfit and model uncertainty remain high over the coastal sector (see also Figs. 8-ef and 9c), their estimates do not surpass 1% of the global mean $p\text{H}$ (8.082). The reconstructed $p\text{H}$ time series reproduce measurement variability with relatively high correlation, r^2 in [0.21, 0.94], that reinforces the reliability of CMEMS-LSCE $p\text{H}$ data.

5.3.2 Ocean acidification: key features from global to local scales

The monthly, 0.25° CMEMS-LSCE datasets of $p\text{H}$, Ω_{ar} , and Ω_{ca} are at the basis of two CMEMS ocean indicators monitoring surface ocean acidification from 1985 to 2021: (1) annual global means and (2) global trend maps.

In Fig. 10, we present annual global means of surface ocean $p\text{H}$ and saturation states for aragonite (Ω_{ar}). An illustration of calcite (Ω_{ca}) is provided in the Appendix (Fig. A13a). For each variable, the calculation of annual global area-weighted means of best estimates (line) and 1σ -uncertainties (envelope) follows Eq. (7). The trends reported in the legend result from linear least-squares regression on annual global means of 100-ensembles of the carbonate system variables. These ensembles are generated with Gaussian distribution having the mean and variance as best model estimate μ and squared uncertainty (σ^2) at monthly time steps and 0.25° -grid cells, respectively. $p\text{H}$ decreases from 8.110 ± 0.017 in 1985 to 8.049 ± 0.014 in 2021 with a descend rate of $-0.017 \pm 0.004 \text{ decade}^{-1}$. Similar trends are found for the surface ocean saturation states with respect to calcium carbonate minerals. The global mean estimates of Ω_{ar} [Ω_{ca}] amount to 3.141 ± 0.198 [4.807 ± 0.302] and 2.862 ± 0.174 [4.372 ± 0.266] for the open and coastal oceans. The saturation state declines at a rate of $-0.080 \pm 0.029 \text{ decade}^{-1}$ with respect to aragonite while the reduction is steeper for calcite ($-0.114 \pm 0.045 \text{ decade}^{-1}$).

Global trend maps of surface ocean $p\text{H}$, Ω_{ar} , and Ω_{ca} over the entire period are illustrated in Figs. 11 and A13b. Linear least-squares regression is used to estimate secular trends at every 0.25° -grid cell. The linear fits of each variable against time rely on the 100-member ensemble generated with the best estimates and propagated uncertainties of $p\text{H}$, Ω_{ar} , and Ω_{ca} (see Figs. A14 for examples). Regression slope and residual standard deviation estimates are defined as linear trend and uncertainty of $p\text{H}$, Ω_{ar} , and Ω_{ca} . Hatched area represents $p\text{H}$ [Ω_{ar} and Ω_{ca}] trend estimates (μ) with highest uncertainties (σ), i.e., σ -to- μ ratio (Eq. 8) above 10% [20%]. These regions include a portion of the Arctic, Antarctic, equatorial Pacific, and coastal ocean (Figs. 11, A11, and A12). 95% of $p\text{H}$ trend estimates over the global ocean is in the range of $[-0.022, -0.012] \text{ decade}^{-1}$ (Fig. 11a). In the broad open ocean of the tropics and subtropics, $p\text{H}$ has been declining around $-0.018 \text{ decade}^{-1}$ to $-0.012 \text{ decade}^{-1}$. Faster decrease rates are found in the Indian Ocean and Southern Ocean with values between -0.022 and $-0.018 \text{ decade}^{-1}$. Fastest reductions are computed for the eastern equatorial Pacific and the Arctic with rates exceeding $-0.025 \text{ decade}^{-1}$. A similar magnitude of $p\text{H}$ trends over these regions is also found in (Lauvset et al., 2015; Leseurre et al., 2022; Ma et al., 2023). The spatial distribution of saturation states with respect to calcium carbonate minerals generally shows the opposite latitudinal pattern (Figs. 11b and A13b). The magnitude of Ω_{ar} [Ω_{ca}] trends over the 30°S - 30°N band can be as large as

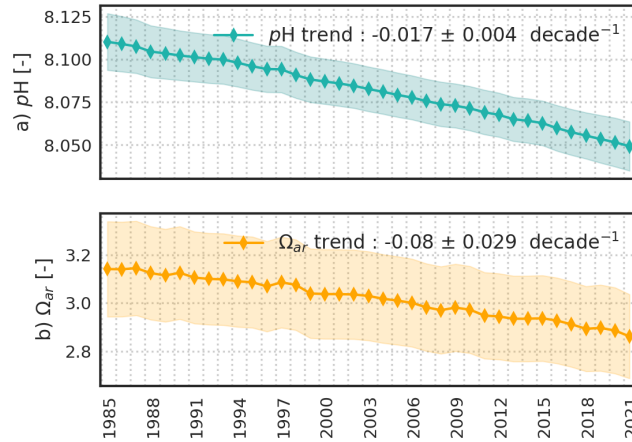


Figure 10. Yearly global area-weighted mean of surface seawater pH reported on total scale (a) and surface ocean saturation states with respect to aragonite (b). Global means of the best estimate (μ , plain line) and of uncertainty (σ , envelop) are computed with Eq. (7a). Trend and uncertainty in the legend are computed with linear regressions on the 100-member ensemble of yearly global means for each variable.

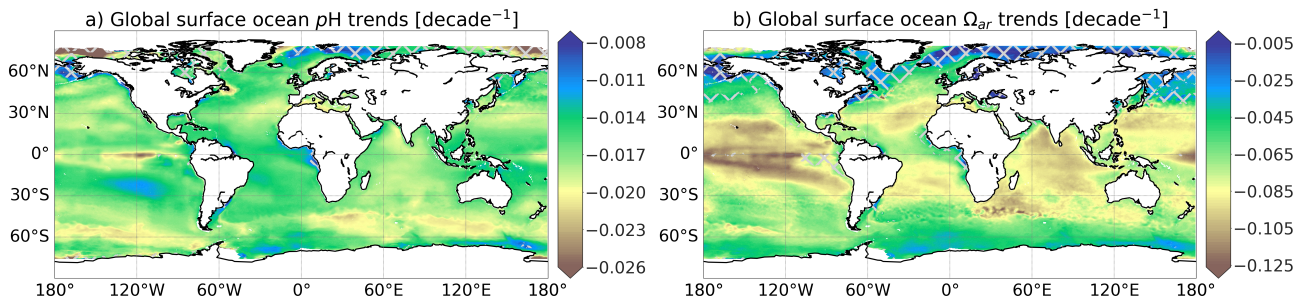


Figure 11. Global trend maps of surface seawater pH reported on total scale (a) and surface ocean saturation states with respect to aragonite (b). Linear trend of CMEMS-LSCE pH and Ω_{ar} is estimated per 0.25° -grid cell over 1985-2021. Cross-hatching covers the regions with uncertainty over 10% [20%] of pH [Ω_{ar}] trend estimates.

560 $-0.086 \text{ decade}^{-1}$ [$-0.134 \text{ decade}^{-1}$] to the greatest extent of $-0.186 \text{ decade}^{-1}$ [$-0.275 \text{ decade}^{-1}$] (e.g., eastern equatorial Pacific). Trends of Ω_{ar} and Ω_{ca} computed in polar and subpolar northern hemisphere regions are not significant.

Trend estimates derived from reconstructions of pH and Ω_{ar} are evaluated at seven time series stations (Bates et al., 2014) in Table 5. Time series locations are shown in Fig. A1b. With the exception of CARIACO and HOT for which pH measurements are available, long-term trend estimates by Bates et al. (2014) rely on time series of pH and Ω_{ar} calculated via speciation
 565 from measurements of A_T and DIC. 100-member ensembles of monthly time series of pH and Ω_{ar} are extracted from the 0.25° -grid box nearest to each monitoring station. Linear least-squares regression is then used to infer estimates of their secular trends and associated uncertainties (see Fig. A14 for illustration). Trend estimates derived from CMEMS-LSCE reconstructions at HOT, BATS, ESTOC, and Munida are in line with previous studies for both pH and Ω_{ar} (Dore et al., 2009; González-

Table 5. Secular trend estimates of pH and Ω_{ar} at seven time-series stations (Bates et al., 2014). Trend and uncertainty estimates are reported as $\mu \pm \sigma$. Monthly time series in the CMEMS-LSCE datasets are extracted at the grid box nearest to each station location (Fig. A1b). For the first three stations, this study calculates linear trends starting in the year 1985. Brackets show values computed over the full period 1985-2021.

Stations	Coordinates	Time span	pH trend [decade ⁻¹]		Ω_{ar} trend [decade ⁻¹]	
			Bates et al. (2014)	This study	Bates et al. (2014)	This study
1. Iceland Sea	68.00°N 12.66°W	1983-2012	-0.014 ± 0.005	-0.010 ± 0.001 (-0.014 ± 0.001)	-0.018 ± 0.027	-0.013 ± 0.011 (-0.025 ± 0.008)
2. Irminger Sea	64.30°N 28.00°W	1983-2012	-0.026 ± 0.006	-0.014 ± 0.001 (-0.016 ± 0.001)	-0.080 ± 0.040	-0.006 ± 0.011 (-0.039 ± 0.009)
3. BATS	32.00°N 64.00°W	1983-2012	-0.017 ± 0.001	-0.014 ± 0.001 (-0.016 ± 0.001)	-0.095 ± 0.007	-0.079 ± 0.016 (-0.074 ± 0.010)
4. ESTOC	29.04°N 15.50°W	1995-2012	-0.018 ± 0.002	-0.018 ± 0.002 (-0.019 ± 0.001)	-0.115 ± 0.023	-0.103 ± 0.031 (-0.089 ± 0.011)
5. HOT*	22.75°N 158.00°W	1988-2012	-0.016 ± 0.001	-0.016 ± 0.001 (-0.019 ± 0.001)	-0.084 ± 0.011	-0.100 ± 0.020 (-0.102 ± 0.011)
6. CARIACO*	10.50°N 64.66°W	1995-2012	-0.025 ± 0.004	-0.017 ± 0.003 (-0.018 ± 0.001)	-0.066 ± 0.028	-0.059 ± 0.053 (-0.099 ± 0.018)
7. Munida	45.70°S 171.50°E	1998-2012	-0.013 ± 0.003	-0.017 ± 0.002 (-0.017 ± 0.001)	-0.085 ± 0.026	-0.088 ± 0.032 (-0.070 ± 0.009)

*Stations with direct observations of pH .

Dávila and Santana-Casiano, 2009; Bates et al., 2014). The magnitude of the trend estimate at Irminger Sea for 1985-2012
570 (pH : -0.014 ± 0.001 decade⁻¹, Ω_{ar} : -0.006 ± 0.011 decade⁻¹) is smaller than that determined by Bates et al. (2014).
However, the CMEMS-LSCE pH trend is consistent with the estimate by Pérez et al. (2021) (-0.017 ± 0.002 decade⁻¹).
Moreover, 1σ -uncertainty reported for both pH and Ω_{ar} trend estimates by Bates et al. (2014) is large at this station (pH :
 -0.025 ± 0.006 decade⁻¹, Ω_{ar} : -0.080 ± 0.040 decade⁻¹) highlighting the associated uncertainty. Long-term trends of pH
and Ω_{ar} are also under-estimated at the Iceland Sea monitoring site, but the bias is not as large as at Irminger Sea (Table 5).
575 Low data sampling frequency at these two stations (Table 1, Bates et al., 2014) could be on account of trend estimate deviation.
At CARIACO, the CMEMS-LSCE time series yields a decrease in Ω_{ar} of -0.059 ± 0.053 decade⁻¹, relatively close to Bates
et al. (2014) (-0.066 ± 0.028 decade⁻¹). The decrease in pH derived from CMEMS-LSCE is, however, larger than in Bates
et al. (2014).

6 Summary

580 This study presents the CMEMS-LSCE product, a dataset of six carbonate system variables (Table 6) covering the global surface ocean at a spatial resolution of 0.25° for every month in the period 1985-2021 (444 months). Datasets of individual carbonate system variables are built on the combination of the three methods. First, we adapt an ensemble of 100 feed-forward neural network models (CMEMS-LSCE-FFNN, Chau et al., 2022b) to estimate surface ocean partial pressure of CO_2 ($p\text{CO}_2$) at the pre-defined data resolution. Second, the high-resolution total alkalinity (A_T) reconstruction is obtained by using locally
585 interpolated alkalinity regression (LIAR, Carter et al., 2016, 2018). Finally, surface ocean $p\text{H}$, total dissolved inorganic carbon (DIC), and saturation states with respect to aragonite (Ω_{ar}) and calcite (Ω_{ca}) are calculated with the carbonate system speciation software (CO2SYS, Lewis and Wallace, 1998; Van Heuven et al., 2011; Orr et al., 2018), given the global monthly reconstructions of $p\text{CO}_2$ and A_T and other environmental input data (Sect. 3). Results are 2D-fields of the best estimate and associated uncertainty (1σ) of carbonate system variables available at each grid box of $1\text{month} \times 0.25^\circ \times 0.25^\circ$. 1σ -uncertainty
590 is referred to as the ensemble standard deviation of 100 FFNN outputs for $p\text{CO}_2$ while it is propagated through the processing chain of LIAR and CO2SYS taking into account different uncertainty sources of input parameters for other variables.

Multiple observation-based datasets, which are not used for the CMEMS-LSCE reconstructions at monthly and 0.25° resolutions, serve as benchmarks in the assessments of product quality from global to local scales (e.g., Tables 3, 4, and A3; Figs. 2-5 and 7-8). A summary of the primary statistics for all the six carbonate variables is presented Table 6. Over the full period
595 1985-2021, CMEMS-LSCE yields global RMSDs of $14.3 \mu\text{atm}$ and $27.6 \mu\text{atm}$ in comparison with SOCATv2022 $p\text{CO}_2$ for the open and coastal oceans, respectively. Temporal variability of observation-based data is well reproduced with r^2 of 0.83 for the open ocean and 0.74 for the coastal domain. In comparison to CMEMS-LSCE at monthly and 1° resolutions (Chau et al., 2022b), the reconstructions over coastal areas are improved at higher resolution. The monthly, 0.25° reconstruction outperforms its 1° counterpart in reproducing horizontal and temporal gradients of $p\text{CO}_2$ over a variety of oceanic regions
600 as well as at nearshore time series stations (Figs. 2-5). Evaluations with GLODAPv2022 bottle data and time series stations results in good reconstruction skills for A_T , DIC, and $p\text{H}$ at monthly and 0.25° resolutions (Tables 4 and A3, Figs. 7 and 8). At the global scale, the open-ocean reconstruction scores a RMSD smaller than $23 \mu\text{mol kg}^{-1}$ and a r^2 of 0.9 in A_T and DIC. The model-observation deviation is higher in the coastal zone. However, it does not exceed 5% of the global mean values and r^2 is above 0.6 for both coastal A_T and DIC. Regarding $p\text{H}$, the CMEMS-LSCE reconstruction provides estimates with
605 RMSD= 0.022 [0.060] and $r^2 = 0.7$ [0.45] over the open [coastal] ocean. From the statistics in Tables 3 and 4, the Indian Ocean and the Southern Ocean have poor data density (Fig. A2) but generally show the best global reconstruction among the ocean basins. Thus, model evaluation with different numbers of observation data might not reflect a fair comparison of skill scores (e.g., RMSD and r^2) between regions. Data density is much higher in the Arctic, Atlantic, and Pacific than in the Indian and Southern Oceans. The increased data density reveals stronger spatio-temporal variability, for instance, related to coastal
610 dynamics or upwelling than resolved in the two latter basins. RMSD and r^2 computed on the lower data variability result in better model scores.

The spatial distribution of long-term mean 1σ -uncertainty estimates (Figs. 1b, 6cd, and 9cd) indicates higher confidence levels for open-ocean estimates than over the coastal sector. The evaluation of temporal mean 1σ -uncertainty estimates relative to climatological mean values μ (Figs. 1a, 6ab, and 9ab) results in σ -to- μ ratio (Eq. 8) below 5% and 8% for $p\text{CO}_2$ and Ω_{ar} , 2% for A_T and DIC, and 0.4% for $p\text{H}$ over the open ocean (Fig. A9). The σ -to- μ ratio reaches values as high as 10% to 20% for $p\text{CO}_2$ and Ω_{ar} in the coastal domain. The global mean of open-ocean 1σ -uncertainty estimates (Eq. 7a) for CMEMS-LSCE $p\text{CO}_2$ (8.5 μatm), A_T (16.7 $\mu\text{mol kg}^{-1}$), DIC (15.8 $\mu\text{mol kg}^{-1}$), $p\text{H}$ (0.011), and Ω_{ar} (0.180) are in line with those reported by previous studies despite being derived from different statistics. For instance, Iida et al. (2021) calculated 1σ -uncertainty based on the median absolute deviation of regression model fits from open-ocean observations. Their approach yielded global σ -averages of 17.8 μatm , 11.5 $\mu\text{mol kg}^{-1}$, 0.018, and 0.110 for $p\text{CO}_2$, normalized DIC, $p\text{H}$, and Ω_{ar} , respectively. In Gregor and Gruber (2021), the authors propagated the sum squared errors (global RMSD and measurement uncertainties) of $p\text{CO}_2$ (15 μatm) and A_T (22 $\mu\text{mol kg}^{-1}$) obtaining global uncertainty estimates of 19 $\mu\text{mol kg}^{-1}$ in DIC and 0.022 in $p\text{H}$. Mean uncertainty estimates over the coastal region are on the order of twofold that computed for the open ocean for these four variables (Table 6), corroborating results by Gregor and Gruber (2021) (Fig. 7).

Table 6. Summary in global evaluation statistics for CMEMS-LSCE surface ocean carbonate system datasets at monthly, 0.25° resolutions over the period 1985-2021. μ and σ stand for the global area-weighted means of monthly best estimates and 1σ -uncertainties for each variable (Eq. 7). RMSD (Eq. 10) and r^2 (Eq. 11) are computed with SOCATv2022 for $p\text{CO}_2$ and GLODAPv2.2022 for $p\text{H}$, A_T , and DIC. The division between the coastal (C) and open (O) oceans is at 400 km on a distance from the shore line (Fig. A1a).

Variables	Standard names	Units	Sector	μ	σ	RMSD	r^2
1. $p\text{CO}_2$	Partial pressure of CO_2 in surface seawater	μatm	(O)	364.5	8.5	14.3	0.83
			(C)	359.4	17.1	27.6	0.74
2. A_T	Total alkalinity in surface seawater	$\mu\text{mol kg}^{-1}$	(O)	2305.8	16.7	22.1	0.90
			(C)	2263.0	38.4	82.0	0.72
3. DIC	Surface ocean dissolved inorganic carbon	$\mu\text{mol kg}^{-1}$	(O)	2031.1	15.8	22.7	0.90
			(C)	2008.7	33.4	72.4	0.62
4. $p\text{H}$	Surface seawater $p\text{H}$ reported on total scale	-	(O)	8.082	0.011	0.022	0.70
			(C)	8.082	0.021	0.060	0.45
5. Ω_{ar}	Saturation state for surface seawater with respect to aragonite	-	(O)	3.059	0.180	-	-
			(C)	2.864	0.206	-	-
6. Ω_{ca}	Saturation state for surface seawater with respect to calcite	-	(O)	4.674	0.275	-	-
			(C)	4.384	0.314	-	-

Our high-resolution carbon data product opens the door to various analyses of the marine carbonate system from global to local scale. This study exemplifies an application of the data for monitoring ocean acidification over recent years. The monitoring indicators derived from the monthly, 0.25° surface ocean CMEMS-LSCE product consist of (1) yearly global means of surface ocean $p\text{H}$ and saturation states with respect aragonite Ω_{ar} and calcite Ω_{ca} and (2) global maps of multi-annual trends of surface ocean $p\text{H}$, Ω_{ar} , and Ω_{ca} (Figs. 10, 11, and A13). In 1985, the global mean surface ocean $p\text{H}$ was 8.110 ± 0.017 . It was 8.049 ± 0.014 in 2021 (Fig. 10a). Over the same 37-year time period, Ω_{ar} decreased from 3.141 ± 0.198 to 2.862 ± 0.174 (Fig. 10b). The rate of decline of surface ocean $p\text{H}$ and Ω_{ar} was respectively -0.017 ± 0.004 decade $^{-1}$ and -0.080 ± 0.029 decade $^{-1}$ since 1985 (see also results for Ω_{ca} in Sect. 5.3.2). Estimates of $p\text{H}$ trend lie between $[-0.022, -0.012]$ decade $^{-1}$ across most

of the open ocean (Fig. 11a). In general, surface ocean pH decreased more rapidly in the Indian Ocean and Southern Ocean than the tropics and subtropics. These findings are in close agreement with the suggestions by Lauvset et al. (2015) and Ma et al. (2023) but future studies would need to include analyses of underlying drivers to provide insight into regional differences in pH changes. By contrast, the greatest reduction in surface ocean saturation states (Fig. 11b) was computed for the two latter regions. The global trend maps of pH and Ω_{ar} highlight the Eastern Equatorial Pacific as one of the vulnerable regions with respect to ocean acidification. In this area, the decline rate of pH exceeds -0.025 decade⁻¹ and -0.186 decade⁻¹ for Ω_{ar} . The comparison of multi-annual trends of pH and Ω_{ar} at time series stations (Table 5 and Fig. A14) highlighted the consistency between CMEMS-LSCE estimates and previous studies (Dore et al., 2009; González-Dávila and Santana-Casiano, 2009; Bates et al., 2014; Pérez et al., 2021). For most of these sites, the trends evaluated for 1985-2021 are greater than those relative to the sub-period before the year 2012. The faster rate of ocean acidification over the full period compared to the pre-2012 probably reflects a steeper acceleration in ocean uptake of anthropogenic CO₂ in the last decade. The global maps of CMEMS-LSCE pH , Ω , and their trend estimates would be potential indicators for ocean acidification along with the SDG 14.3.1 - "Average marine acidity (pH) measured at agreed suite of representative sampling stations" (<https://sdgs.un.org/goals/goal14>: last access 31/07/2023).

The production chain of CMEMS-LSCE carbonate system variables will be maintained and further improvements with the aim to reduce model-observation misfit and improve the quantification of model uncertainty are on the way forward. Being at the core of the chain, model upgrades of CMEMS-LSCE-FFNN will be tackled first. At the time, SOCAT does not provide open-ocean data of CO₂ fugacity gridded at monthly, 0.25° resolutions. Our ensemble-based approach draws thus on two SOCATv2022 data sources: a "downscaled" version of the 1°-open-ocean data and the 0.25°-coastal-ocean data (see Sect. 2.1). Open-ocean SOCAT datasets gridded at finer regular resolutions (if accessible) will be updated to gain more accuracy in our model fitting. Selections of data products for predictors needed for model input are equally important. For instance, the CMEMS SSS product used here results in a globally good reconstruction of total alkalinity (Table 4). However, the temporal variability in CMEMS SSS data does not match that in observations (Fig. A10) and this feature is retained in time series of total alkalinity (Fig. 7). Despite best efforts in determining overall product uncertainty in estimates of carbonate system variables, part of input uncertainty is still not taken into account or only partially quantified due to lack of time-space varying uncertainty fields associated with predictor variables (e.g. SSH, Chl-a, MLD, nutrient concentrations). Moreover, temporal sampling bias in pCO_2 and pH is likely to contribute to deviations between observations and model output (Fig. 5 and Table A3). The total analytical error uncertainty should be considered with great care during reconstruction and model output evaluation.

The CMEMS-LSCE approach leads as the first series of long-term reconstructions of pCO_2 , pH , A_T , DIC, Ω_{ca} and Ω_{ar} extending seamlessly from the global open ocean to coastal regions at monthly, 0.25° resolutions. Future use cases recommended for this high-resolution product include (1) estimation of monthly to interannual variations, long-term trends of carbonate system variables, as well as of air-sea CO₂ exchanges at the surface layer from local scale to large ocean basins, (2) analyses in interactions between these variables and effects of other physical and biogeochemical factors on ocean acidification and changes in the marine carbonate system, (3) assessments of horizontal and temporal gradients of carbonate system variables in the coastal-open ocean continuum, (4) evaluation or combination with other model- or observation-based products (e.g.,

Biogeochemistry Argo, Southern Ocean Carbon and Climate Observations and Modeling), and (5) improvements in coastal reconstructions based on observation system simulation experiments (e.g., with finer spatio-temporal model resolutions). The
670 CMEMS-FFNN surface ocean carbon product at monthly, 0.25° resolutions will be accessible through the CMEMS data portal (see Sect. 7).

7 Data availability

The CMEMS-LSCE datasets (netCDF format) of six carbonate system variables have been delivered to the European Copernicus Marine Environment Monitoring Service (CMEMS, Product ID: MULTIOBS_GLO_BIO_CARBON_SURFACE_REP_015_008,
675 DOI: 10.48670/moi-00047). Since November 2022, the product with monthly and 1° resolutions is available at the CMEMS portal (Chau et al., 2022a, b). The CMEMS-LSCE data product at monthly and 0.25° resolutions proposed in this study will replace its coarser resolution version in due course. For the time being, the high-resolution data product described in this manuscript can be accessed via repository under data DOI: 10.14768/a2f0891b-763a-49e9-af1b-78ed78b16982 (Chau et al., 2023).

680 *Author contributions.* TTTC, FC, and MG developed the CMEMS-LSCE-FFNN model at a quarter-degree resolution. TTTC has prepared script codes and executed the experiments with support from FC in setting and running the model at the HPC resources of TGCC. TTTC, MG, NM, and FC shaped the first manuscript version. All the authors contribute to the manuscript revision.

Competing interests. The author and co-authors have declared that they have no competing interests.

Acknowledgements. This research has been supported by the MOB TAC project of the European Copernicus Marine Environment Monitoring Service (CMEMS) (<https://marine.copernicus.eu/about/producers/mob-tac>, last access: 14 March 2023). It was granted access to the
685 HPC resources of TGCC under the allocation A0110102201 made by GENCI. The Surface Ocean CO₂ Atlas (SOCAT, www.socat.info, last access: 20 March 2023) is an international effort endorsed by the International Ocean Carbon Coordination Project (IOCCP), the Surface Ocean Lower Atmosphere Study (SOLAS) and the Integrated Marine Biogeochemistry and Ecosystem Research program (IMBER), to deliver a uniformly quality-controlled surface ocean CO₂ database. The Global Ocean Data Analysis Project (GLODAP, www.glodap.info, last
690 access: 21 August 2023) provides access to ocean surface-to-bottom quality controlled data of carbonate system variables collected through international cruises. We thank Anna Conchon for her help in testing and wrapping LIAR and CO2SYS Matlab toolboxes. We are grateful for constructive comments from two anonymous reviews to refine the manuscript.

Appendix

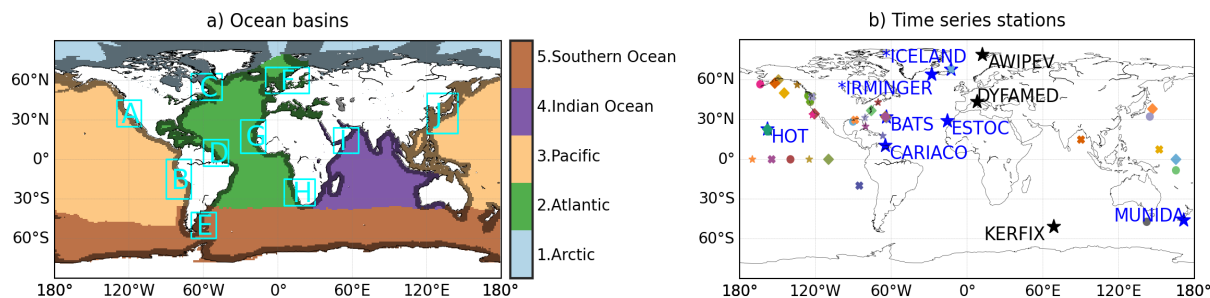


Figure A1. a) Ocean basins (<https://github.com/RECCAP2-ocean/RECCAP2-shared-resources/tree/master/data/regions>, last access: 11/7/2022): coastal mask (grey, approximately 400 km from the shoreline), feature regions analysed in this study (cyan box, Table A1); b) Location of time series stations recording in situ observations used in data evaluation (Table 2): blue stars for ocean acidification (Bates et al., 2014), black stars for A_T and DIC (Metzl and Lo Monaco, 1998; Coppola et al., 2021; Gattuso et al., 2023), and other coloured scattered objects for pCO_2 and pH (Sutton et al., 2019). Asterisk (*) marks the two stations with also A_T and DIC observations (Olafsson et al., 2010) available for assessments.

Table A1. Information of feature regions analysed in this study (Fig. A1a - cyan boxes).

Notations	Regions	Coordinates	
		Latitude	Longitude
A	California Current System	25°N-45°N	130°W-110°W
B	Humboldt Current System	30°S-0°	90°W-70°W
C	Labrador Sea	45°N-65°N	70°W-45°W
D	Amazon river mouth	5°S-15°N	60°W-40°W
E	Western South Atlantic	60°S-40°S	70°W-50°W
F	Northern Europe	50°N-70°N	10°W-25°E
G	Canary Current System	5°N-30°N	30°W-10°W
H	Benguela Current System	35°S-15°S	5°E-20°E
I	Western Arabian Sea	5°N-24°N	45°E-65°E
J	Sea of Japan	30°N-50°N	120°E-150°E

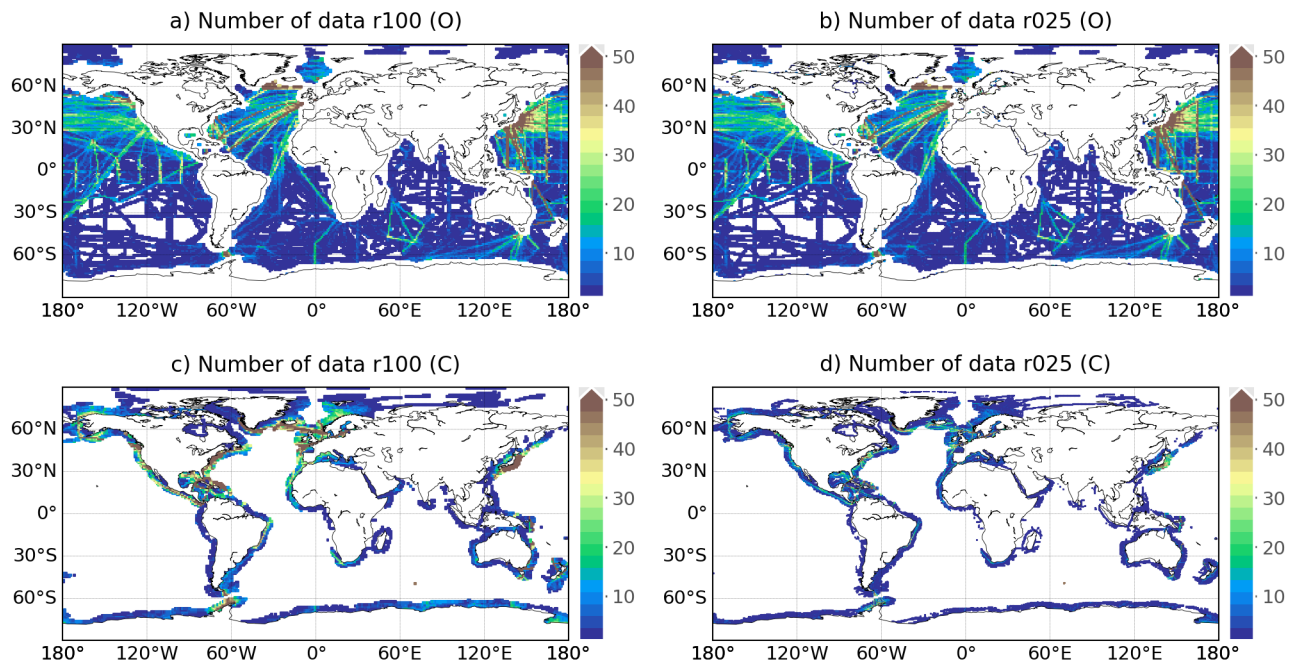


Figure A2. Spatial distribution of total months in 1985-2021 containing SOCATv2022 gridded data. Left: 1° -data product (r100), right: 0.25° -data product (r025). Open-ocean data (O) in each 0.25° -grid box is created by setting conservatively the open-ocean SOCATv2022 data at the 1° -grid box containing it. The coastal-ocean SOCATv2022 data (C) are assigned within 400 km from the shoreline (Fig. A1a).

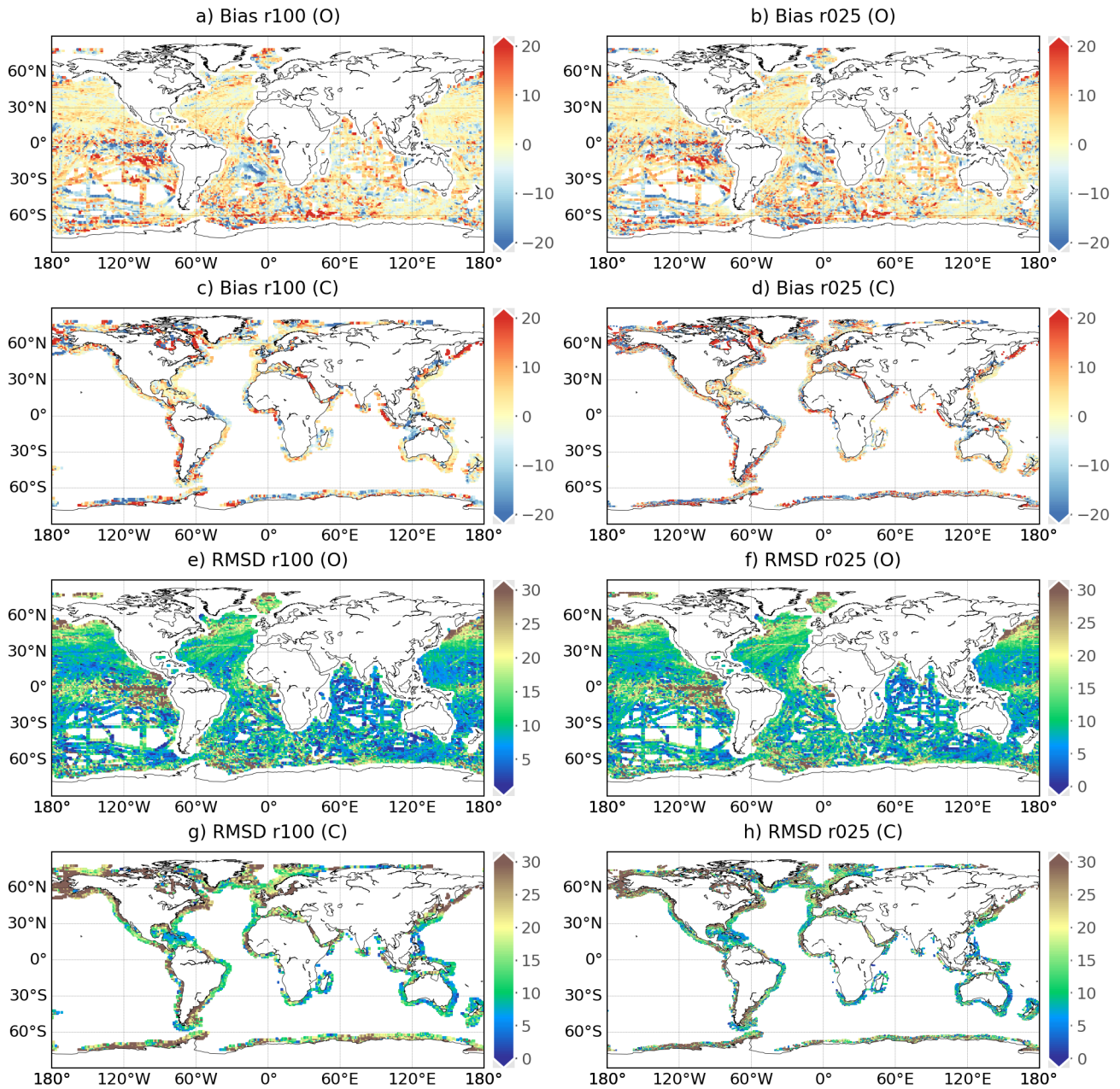


Figure A3. Global maps of mean model-data difference (Bias, abcd) and root-of-mean-square-deviation (RMSD, efgh) between the reconstruction and SOCATv2022 $p\text{CO}_2$ [μatm] over 1985-2021. Left: CMEM-LSCE-FFNN with a resolution of 1° (r100), right: CMEM-LSCE-FFNN with a resolution of 0.25° (r025). Open-ocean data (O) in each 0.25° -grid box used for evaluation is created by setting conservatively the open-ocean SOCATv2022 data value at the 1° -grid box containing it. Coastal-ocean data (C) are extracted from each of the two SOCATv2022 gridded data products.

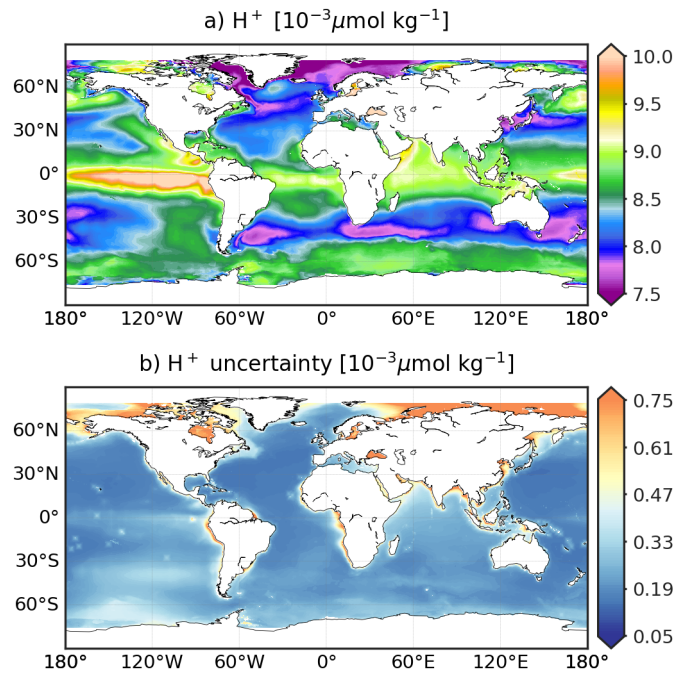


Figure A4. CMEMS-LSCE H^+ over the global ocean at a spatial resolution of 0.25° . Temporal means of the model best estimate and 1σ -uncertainty per grid cell over 1985-2021 are calculated by using Eq. (5).

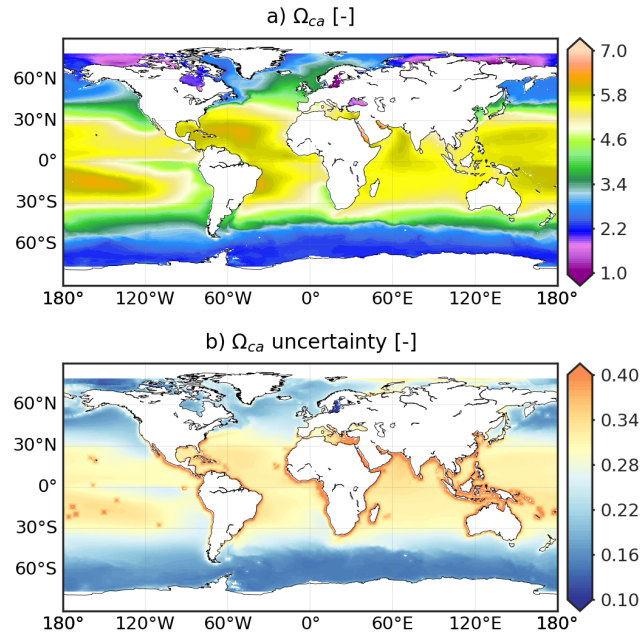


Figure A5. CMEMS-LSCE Ω_{ca} over the global ocean at a spatial resolution of 0.25° . Temporal means of the model best estimate and 1σ -uncertainty per grid cell over 1985-2021 are calculated by using Eq. (5).

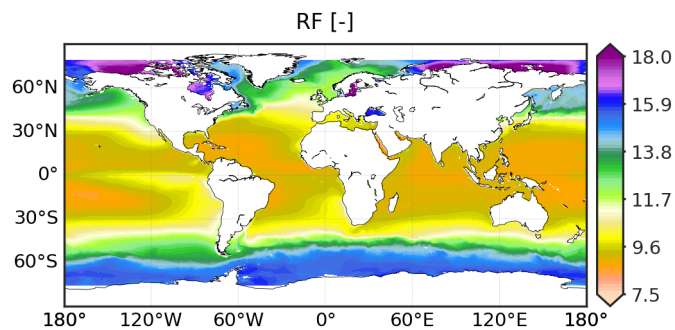


Figure A6. CMEMS-LSCE Revelle Factor (RF) over the global ocean at a spatial resolution of 0.25° . Temporal means of the model best estimate per grid cell over 1985-2021 are calculated by using Eq. (5).

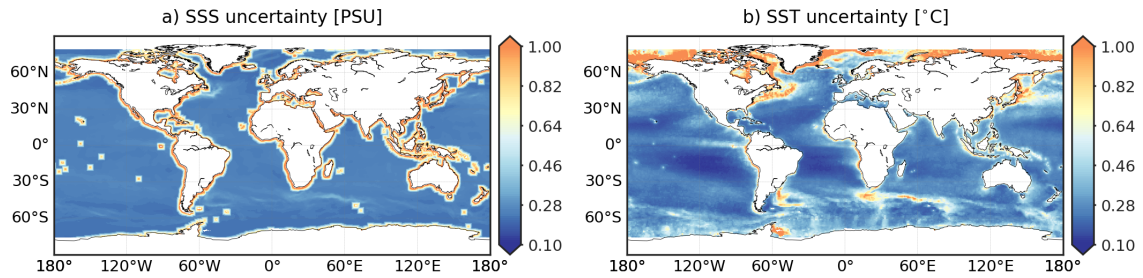


Figure A7. Spatial distribution of CMEMS SSS and SST product uncertainty over the global ocean at a spatial resolution of 0.25° . 1σ -uncertainty is computed per grid cell by using Eq. (5) over 1985-2021.

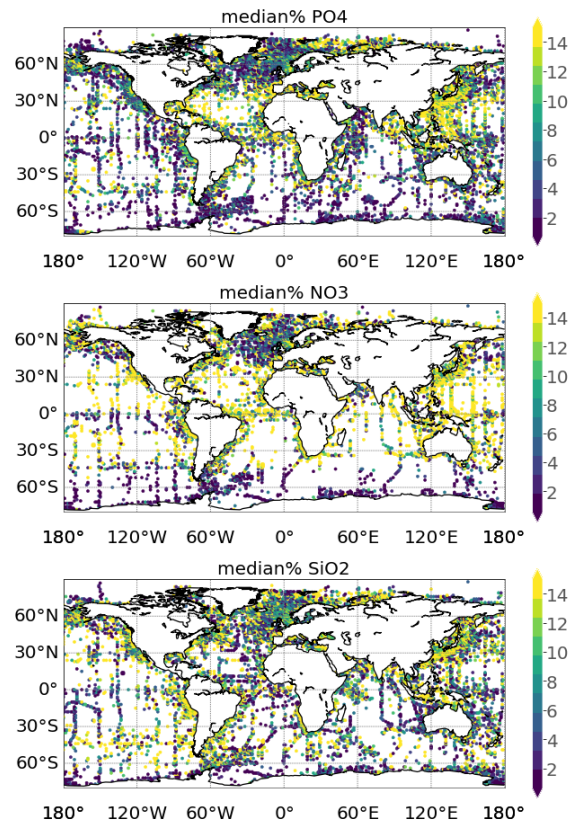


Figure A8. Median percentage of analysis error uncertainty against of climatological mean of surface WOA18 nutrient data: phosphate (PO_4), nitrate (NO_3), and silicate (SiO_2).

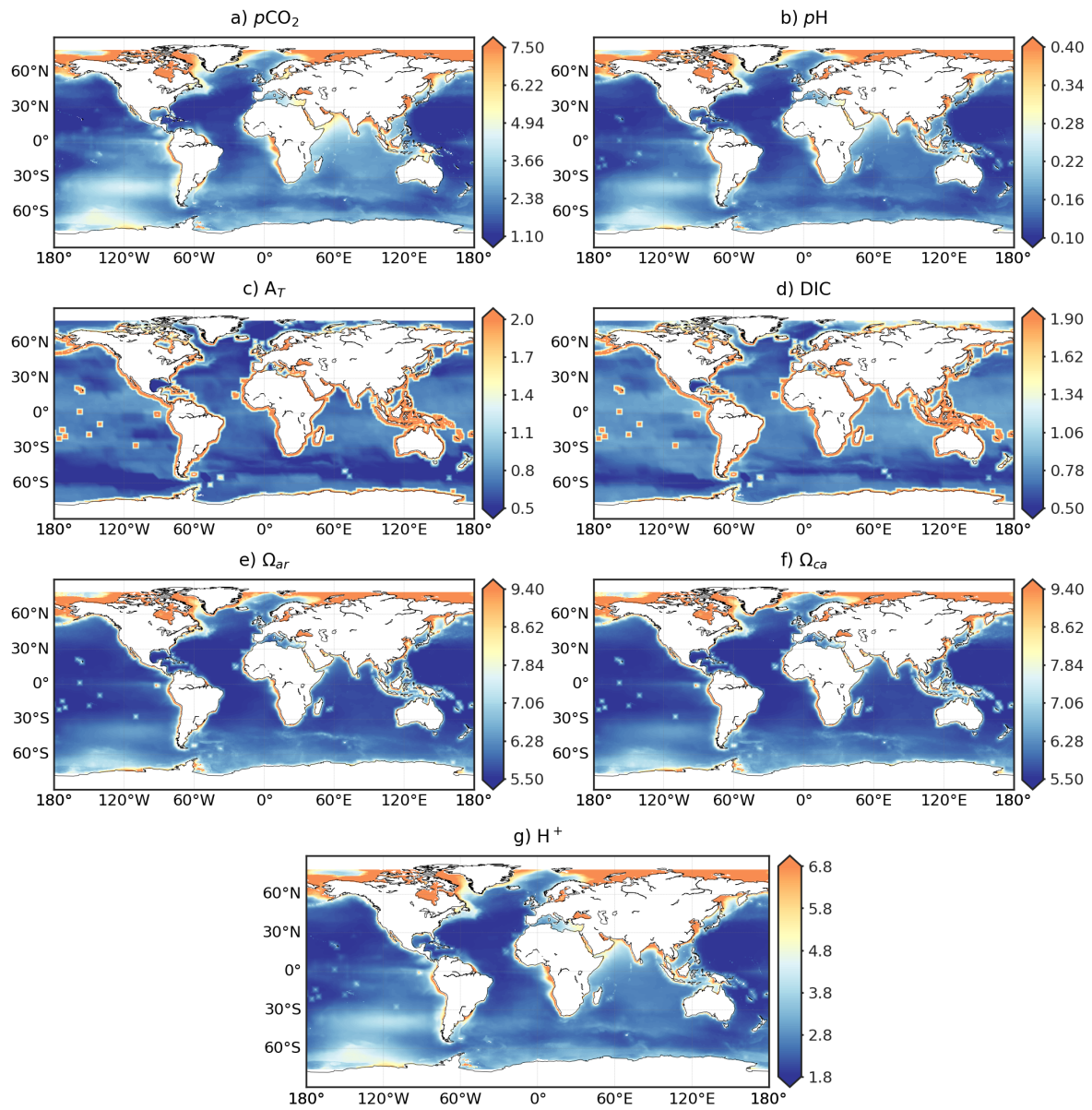


Figure A9. Spatial distribution of $R(\sigma, \mu)$ [%] (Eq 8), i.e., the ratio of model uncertainty (σ) against model best estimate (μ).

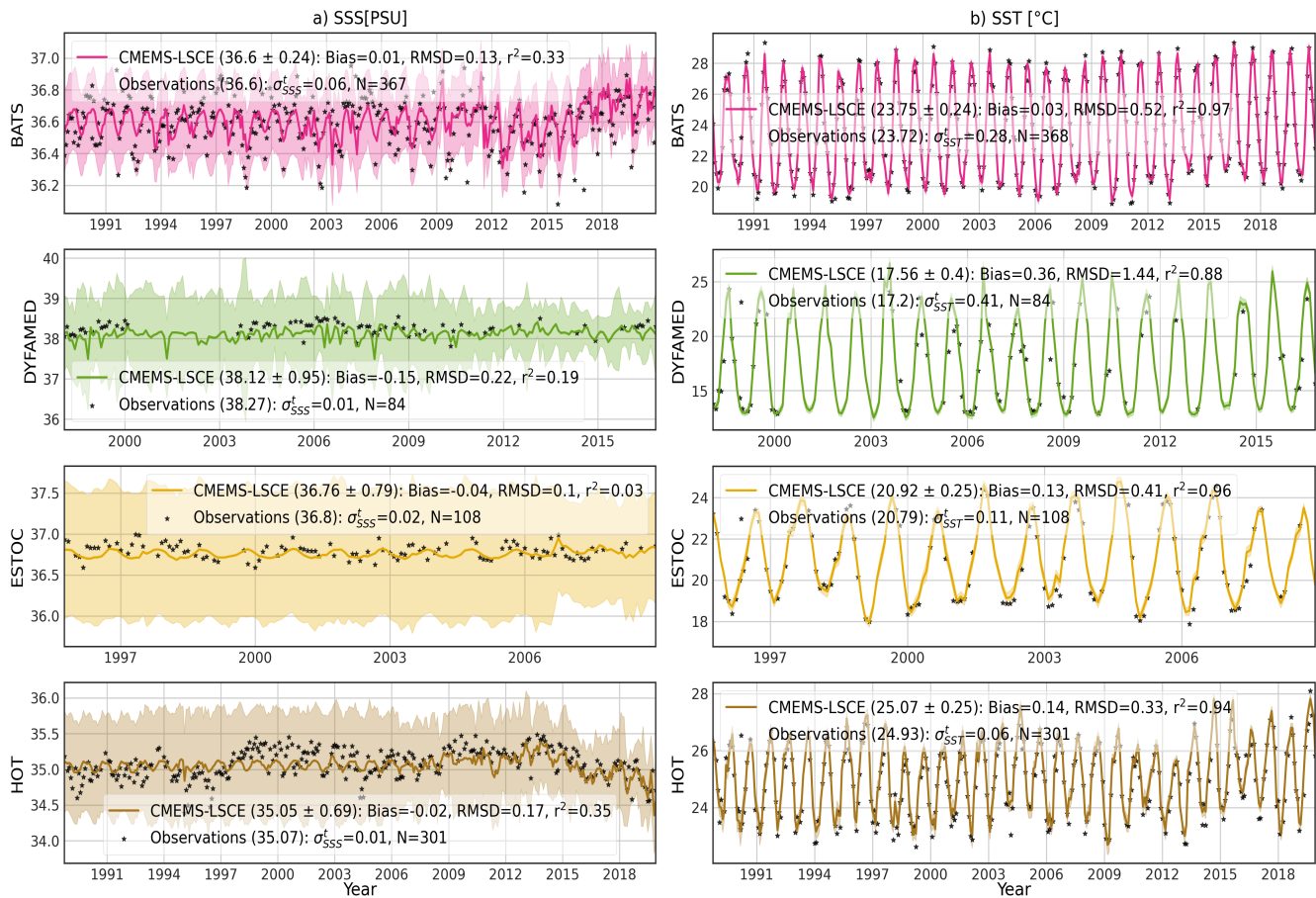


Figure A10. Monthly time series of SSS and SST at BATS, DYFAMED, ESTOC, and HOT stations (Table 2 and Fig. A1b): CMEMS data (curve), 1σ -uncertainty (envelope), and monthly average of observations (point). Means of CMEMS data and 1σ -uncertainty ($\mu \pm \sigma$) calculated over the observing time span are shown in brackets if accessible. Statistics include the number of months with observations (N), Bias, RMSD, and r^2 . σ_{SSS}^t [σ_{SST}^t] stands for temporal standard deviation from monthly averages of SSS and SST observations. Temporal variations in SSS observations are poorly described in the CMEMS SSS time series (Table 1) used in CMEMS-LSCE reconstructions.

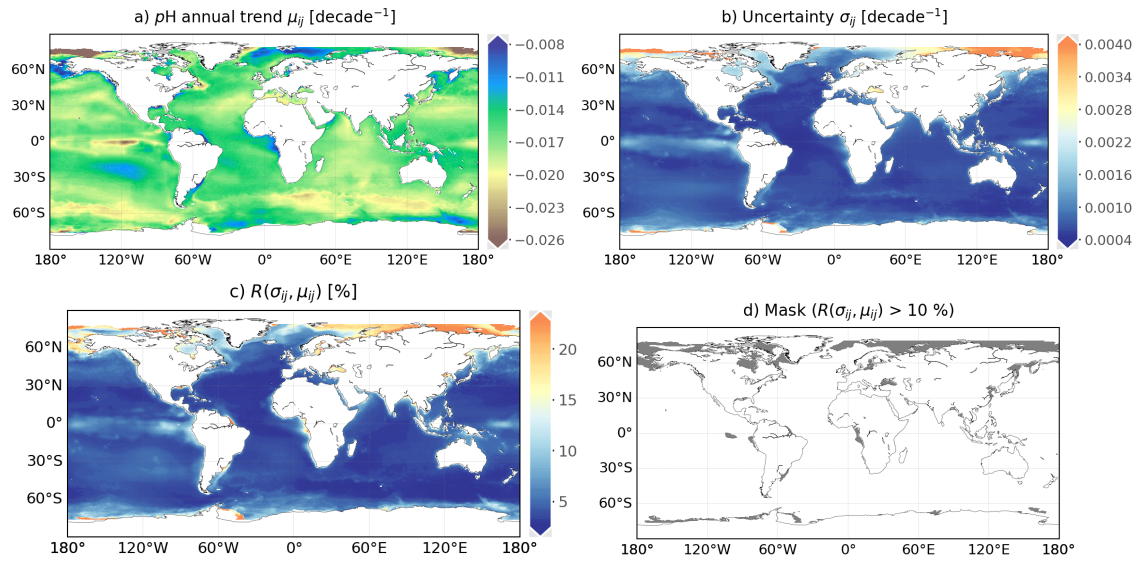


Figure A11. a) Global surface seawater pH trend over the period 1985-2021, b) 1σ -uncertainties associated to trend estimates, c) σ -to- μ ratio $R(\sigma, \mu)$ [%] (Eq. 8) between uncertainty estimates (b) and the best trend estimates (a), d) mask applied over the regions where $R(\mu, \sigma) > 10\%$.

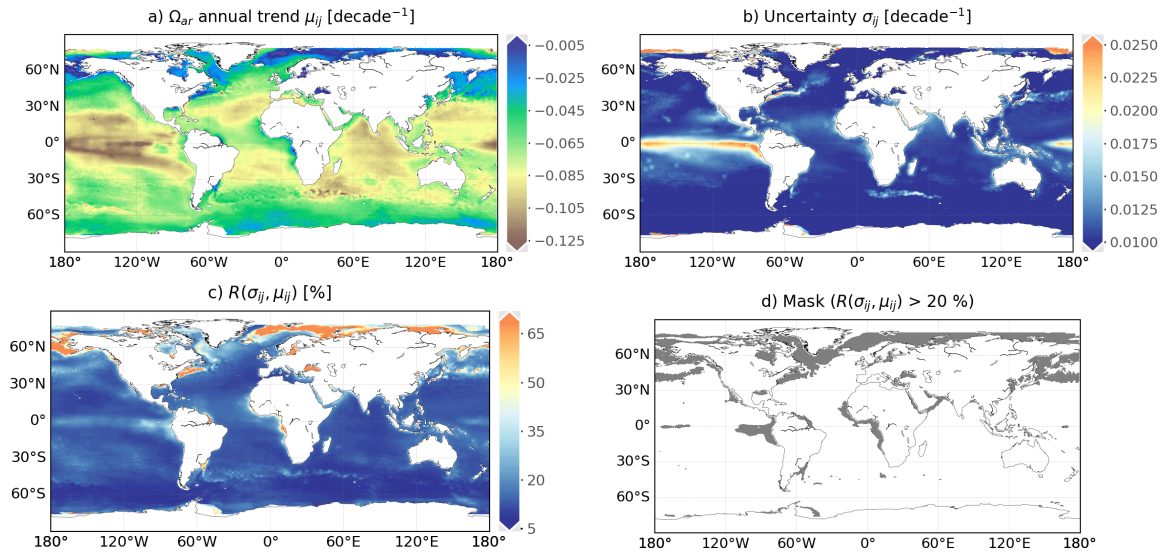


Figure A12. a) Global surface seawater Ω_{ar} trend over the period 1985-2021, b) 1σ -uncertainties associated to trend estimates, c) σ -to- μ ratio $R(\sigma, \mu)$ [%] (Eq. 8) between uncertainty estimates (b) and the best trend estimates (a), d) mask applied over the regions where $R(\mu, \sigma) > 20\%$.

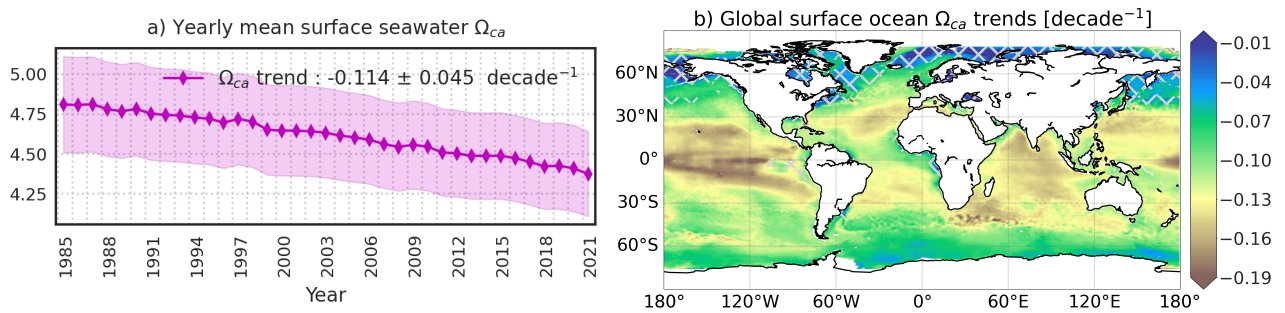


Figure A13. a) Yearly global area-weighted mean of surface ocean saturation states with respect to calcite (Ω_{ca}): Global means of the best estimate (μ , plain line) and uncertainty (σ , envelop) are computed with Eq. (7a). b) Global trend maps of Ω_{ca} over 1985-2021: Cross-hatching covers the regions with uncertainty of a trend estimate over 20% of the trend value.

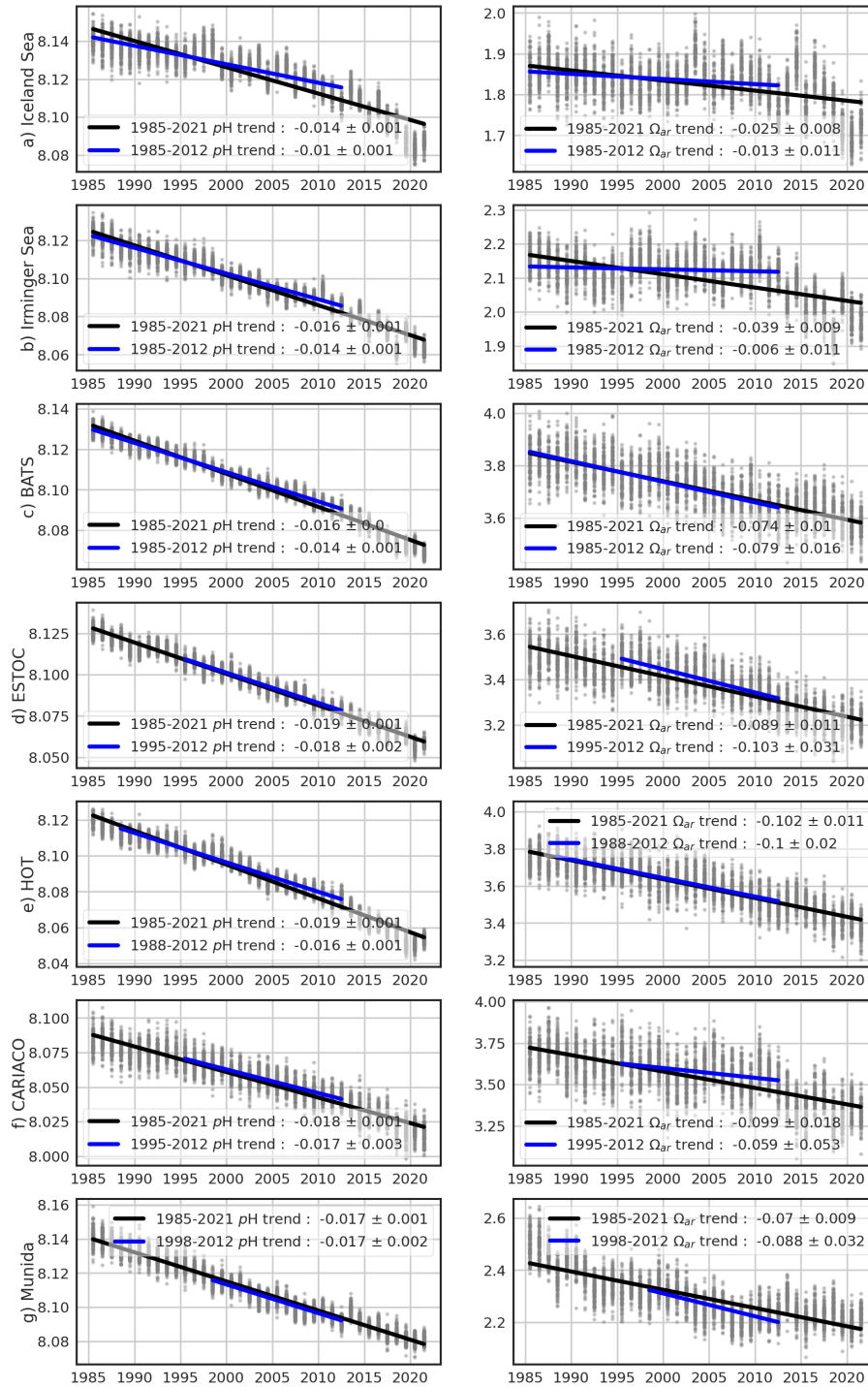


Figure A14. Linear trend estimates learned on 100-member ensemble (grey points) of yearly mean time series of pH and Ω_{ar} at different stations (Bates et al., 2014). $\mu \pm \sigma$ present linear slope and residual standard deviation. Black or blue lines stand for linear fits over the full or sub-period in 1985-2021 (see Table 5 for comparison).

Table A2. Information of moored time series of surface-ocean $p\text{CO}_2$ and $p\text{H}$ observations (Sutton et al., 2019).

Stations	Abbreviations	Coordinates	Date range
Ala Wai Water Quality Buoy Pacific island	ALAWAI	21.3°N, 157.9°W	06/2008-12/2020
Bay of Bengal Ocean Indian Ocean	BOBOA	15.0°N, 90.0°W	11/2013-12/2017
Bermuda Testbed Mooring	BTM	31.5°N, 64.2°W	10/2005f-12/2006
California Current Ecosystem 2	CCE2	34.3°N, 120.8°W	01/2010-06/2021
Cape Arago	CAPEARAGO	43.3°N, 124.5°W	06/2017-12/2020
Cape Elizabeth	CAPEELIZABETH	47.4°N, 124.7°W	06/2006-05/2020
Chá b'a Buoy in the Northwest Enhanced Moored Observatory and Olympic Coast NMS	CHABA	47.9°N, 126°W	07/2010-09/2020
Chuuk Lagoon Ocean Acidification Mooring	CHUUK	7.5°N, 151.9°E	11/2011-12/2017
Cheeca Rocks Ocean Acidification Mooring in Florida Keys National Marine Sanctuary	CHEECAROCKS	24.9°N, 80.6°W	12/2011-12/2021
Coastal Louisiana buoy	COASTALLA	28.5°N, 90.3°W	07/2017-08/2020
Central Gulf of Mexico Ocean Observing System Station 01	COASTALMS	30.0°N, 88.6°W	05/2009-05/2017
Crescent Reef Bermuda Buoy	CRESCENTREEF	32.4°N, 64.8°W	11/2010-12/2014
Coral Reef Instrumented Monitoring Platform 1	CRIMP1	21.4°N, 157.8°W	12/2005-12/2007
Coral Reef Instrumented Monitoring Platform 2	CRIMP2	21.5°N, 157.8°W	06/2008-12/2019
Chesapeake Bay Interpretive Buoy System Ocean Acidification Buoy at First Landing	FIRSTLANDING	37.0°N, 76.1°W	04/2018-09/2020
NANOOS ORCA buoy in Dabob Bay	DABOB	47.8°N, 122.8°W	06/2011-01/2016
Gulf of Alaska Ocean Acidification Mooring	GAKOA	59.9°N, 149.4°W	05/2011-12/2017
NDBC Buoy 41008 in Gray's Reef National Marine Sanctuary	GRAYSREEF	31.4°N, 80.9°W	07/2006-08/2018
Coastal Western Gulf of Maine Mooring	GULFOFMAINE	43.0°N, 70.5°W	07/2006-06/2021
Hog Reef Bermuda Buoy	HOGREEF	32.5°N, 64.8°W	12/2010-12/2017
North Atlantic Ocean Acidification Mooring	ICELAND	68.0°N, 12.7°W	08/2013-06/2017
Kaneohe Bay Ocean Acidification Offshore Observatory	KANEOHE	21.5°N, 157.8°W	09/2011-12/2019
Kuroshio Extension Observatory	KEO	32.3°N, 144.6°E	09/2007-12/2019
Kilo Nalu Water Quality Buoy at South Shore Oahu	KILONALU	21.3°N, 157.9°W	08/2008-12/2018
Kodiak Alaska Ocean Acidification Mooring	KODIAK	57.7°N, 152.3°W	03/2013-12/2015
La Parguera Ocean Acidification Mooring	LAPARGUERA	18.0°N, 67.1°W	01/2009-12/2018
Southeastern Bering Sea Mooring Site 2	M2	56.5°N, 164.0°W	05/2013-09/2017
Newport Hydrographic Line Station 10 Ocean Acidification Mooring	NH10	44.9°N, 124.8°W	04/2014-12/2016
Ocean Station Papa	PAPA	50.1°N, 144.8°W	06/2007-12/2019
Southeast Alaska Ocean Acidification Mooring	SEAK	56.3°N, 134.7°W	03/2013-12/2015
Southern Ocean Flux Station	SOFS	46.8°S, 142.0°E	11/2011-12/2020
Stratus	STRATUS	19.7°S, 85.6°W	10/2006-12/2017
National Data Buoy Center (NDBC) Tropical Atmosphere Ocean	TAO110W	0.0°N, 110.0°W	09/2009-12/2018
NDBC Tropical Atmosphere Ocean	TAO125W	0.0°N, 125.0°W	05/2004-12/2020
NDBC Tropical Atmosphere Ocean	TAO140W	0.0°N, 140.0°W	05/2004-4/2019
NDBC Tropical Atmosphere Ocean	TAO155W	0.0°N, 155.0°W	01/2010-07/2020
NDBC Tropical Atmosphere Ocean	TAO165E	0.0°N, 165.0°E	02/2010-12/2019
NDBC Tropical Atmosphere Ocean	TAO170W	0.0°N, 170.0°W	07/2005-12/2017
NDBC Tropical Atmosphere Ocean	TAO8S165E	8.0°S, 165.0°E	06/2009-11/2011
ORCA buoy at Twanoh in Hood Canal	TWANOH	47.4°N, 123.0°W	08/2009-12/2020
Woods Hole Oceanographic Institution Hawaii Ocean Time-series Station	WHOTS	22.7°N, 158.0°W	12/2004-12/2018

Table A3. Statistics computed between CMEMS-LSCE datasets (0.25°) and time series of $p\text{CO}_2$ and $p\text{H}$ measurements (Sutton et al., 2019) at open-ocean (O) and coastal stations (C): total numbers of monthly mean observations (N), temporal standard deviation of observations from their monthly averages (σ^t), RMSD (Eq. 10), and r^2 (Eq. 11). See Table A2 and Fig. A1b for stations' information and locations.

Stations	$p\text{CO}_2$ [μatm]				$p\text{H}$ [-]			
	N	σ^t	RMSD	r^2	N	σ^t	RMSD	r^2
O1. BOBOA	42	9.9	9.6	0.69	19	0.010	0.011	0.71
O2. BTM	15	7.2	11.4	0.98	0	—	—	—
O3. CHUUK	66	10.9	23.5	0.60	33	0.014	0.033	0.78
O5. CRESCENTREEF	41	13.6	45.0	0.93	0	—	—	—
O5. HOGREEF	60	23.3	47.8	0.85	0	—	—	—
O6. ICELAND	24	8.1	16.9	0.68	4	0.007	0.092	0.94
O7. KEO	130	9.0	10.1	0.92	48	0.010	0.014	0.86
O8. PAPA	135	5.7	8.7	0.60	103	0.007	0.017	0.40
O9. SOFS	61	7.1	7.8	0.81	0	—	—	—
O10. STRATUS	116	6.3	9.2	0.80	10	0.004	0.042	0.43
O11. TAO110W	67	22.8	17.7	0.79	0	—	—	—
O12. TAO125W	124	16.5	16.0	0.43	0	—	—	—
O13. TAO140W	92	11.4	12.0	0.44	0	—	—	—
O14. TAO155W	45	11.3	12.2	0.75	0	—	—	—
O15. TAO165E	39	9.1	19.8	0.76	0	—	—	—
O16. TAO170W	87	9.0	17.9	0.45	0	—	—	—
O17. TAO8S165E	29	7.1	10.5	0.49	0	—	—	—
O18. WHOTS	143	4.7	8.0	0.80	23	0.004	0.01	0.57
C1. ALAWAI	112	20.3	22.8	0.32	0	—	—	—
C2. CAPEARAGO	33	65.6	79.9	0.19	31	0.086	0.069	0.22
C3. CAPEELIZABETH	92	42.5	41.4	0.52	11	0.061	0.057	0.69
C4. CCE2	127	45.3	32.4	0.16	58	0.048	0.035	0.24
C5. CHABA	75	51.2	65.3	0.44	42	0.056	0.064	0.58
C6. CHEECAROCKS	73	44.1	62.4	0.25	40	0.038	0.066	0.21
C7. COASTALLA	22	59.2	57.4	0.52	2	0.078	0.068	—
C8. COASTALMS	41	43.0	42.5	0.51	15	0.062	0.065	0.25
C9. CRIMP1	23	26.4	95.6	0.62	0	—	—	—
C10. CRIMP2	119	85.4	90.7	0.58	0	—	—	—
C11. DABOB	24	55.0	89.3	0.74	0	—	—	—
C12. FIRSTLANDING	17	70.0	77.3	0.49	2	0.061	0.042	—
C13. GAKOA	64	20.3	66.0	0.73	0	—	—	—
C14. GRAYSREEF	96	20.1	38.3	0.65	49	0.020	0.040	0.66
C15. GULFOFMAINE	144	26.7	31.2	0.54	77	0.029	0.042	0.27
C16. KANEOHE	49	20.9	23.5	0.36	35	0.025	0.034	0.25
C17. KILONALU	69	14.3	11.6	0.56	0	—	—	—
C18. KODIAK	34	31.7	62.1	0.78	0	—	—	—
C19. LAPARGUERA	103	12.9	41.6	0.41	48	0.012	0.038	0.33
C20. M2	23	25.4	55.8	0.24	0	—	—	—
C21. NH10	25	64.6	31.4	0.46	15	0.058	0.048	0.42
C22. SEAK	31	53.4	141.3	0.82	0	—	—	—
C23. TWANOH	57	126.2	199.9	0.33	0	—	—	—

Table A4. Statistics computed between CMEMS-LSCE datasets (0.25°) and time series of A_T and DIC measurements (0–10 m depth): total numbers of monthly mean observations (N), temporal standard deviation of observations from their monthly averages (σ^t), RMSD (Eq. 10), and r^2 (Eq. 11). See Table 2 and Fig. A1b for stations’ information and locations.

Stations	A_T [$\mu\text{mol kg}^{-1}$]				DIC [$\mu\text{mol kg}^{-1}$]			
	N	σ^t	RMSD	r^2	N	σ^t	RMSD	r^2
1. AWIPEV	52	15.8	32.0	0.33	52	17.7	29.6	0.71
2. BATS	303	2.4	9.6	0.34	351	1.9	8.2	0.82
3. DYFAMED	84	1.3	145.7	0.12	84	2.0	124.7	0.61
4. ESTOC	298	1.3	8.3	0.03	108	1.4	11.2	0.47
5. HOT	298	0.8	12.5	0.32	298	0.6	10.6	0.70
6. ICELAND	27	2.5	13.4	0.24	27	0.8	13.7	0.79
7. IRMINGER	29	1.8	8.4	0.30	23	1.7	14.6	0.84
8. KERFIX	23	1.0	7.4	0.22	23	3.4	14.0	0.52

References

- 695 Bakker, D., Alin, S., Becker, M., Bittig, H., Castaño-Primo, R., Feely, R. A., Gritzalis, T., Kadono, K., Kozyr, A., Lauvset, S. K., Metzl, N., Munro, D., Nakaoka, S.-i., Nojiri, Y., O'Brien, K., Olsen, A., Pfeil, B., Pierrot, D., Steinhoff, T., Sullivan, K., Sutton, A., Sweeney, C., Tilbrook, B., Wada, C., Wanninkhof, R., Wranne, A. W., et al.: SOCAT version 2022 for quantification of ocean CO₂ uptake, https://www.socat.info/wp-content/uploads/2022/06/2022_Poster_SOCATv2022_release.pdf, 2022.
- Bakker, D. C. E., Pfeil, B., Landa, C. S., Metzl, N., O'Brien, K. M., Olsen, A., Smith, K., Cosca, C., Harasawa, S., Jones, S. D., Nakaoka, S.,
700 Nojiri, Y., Schuster, U., Steinhoff, T., Sweeney, C., Takahashi, T., Tilbrook, B., Wada, C., Wanninkhof, R., Alin, S. R., Balestrini, C. F., Barbero, L., Bates, N. R., Bianchi, A. A., Bonou, F., Boutin, J., Bozec, Y., Burger, E. F., Cai, W.-J., Castle, R. D., Chen, L., Chierici, M., Currie, K., Evans, W., Featherstone, C., Feely, R. A., Fransson, A., Goyet, C., Greenwood, N., Gregor, L., Hankin, S., Hardman-Mountford, N. J., Harlay, J., Hauck, J., Hoppema, M., Humphreys, M. P., Hunt, C. W., Huss, B., Ibáñez, J. S. P., Johannessen, T., Keeling, R., Kitidis, V., Körtzinger, A., Kozyr, A., Krasakopoulou, E., Kuwata, A., Landschützer, P., Lauvset, S. K., Lefèvre, N., Lo Monaco, C., Manke, A.,
705 Mathis, J. T., Merlivat, L., Millero, F. J., Monteiro, P. M. S., Munro, D. R., Murata, A., Newberger, T., Omar, A. M., Ono, T., Paterson, K., Pearce, D., Pierrot, D., Robbins, L. L., Saito, S., Salisbury, J., Schlitzer, R., Schneider, B., Schweitzer, R., Sieger, R., Skjelvan, I., Sullivan, K. F., Sutherland, S. C., Sutton, A. J., Tadokoro, K., Telszewski, M., Tuma, M., van Heuven, S. M. A. C., Vandemark, D., Ward, B., Watson, A. J., and Xu, S.: A multi-decade record of high-quality *f*CO₂ data in version 3 of the Surface Ocean CO₂ Atlas (SOCAT), *Earth System Science Data*, 8, 383–413, <https://doi.org/10.5194/essd-8-383-2016>, 2016.
- 710 Bates, N. R., Astor, Y. M., Church, M. J., Currie, K., Dore, J. E., González-Dávila, M., Lorenzoni, L., Muller-Karger, F., Olafsson, J., and Santana-Casiano, J. M.: A time-series view of changing surface ocean chemistry due to ocean uptake of anthropogenic CO₂ and ocean acidification, *Oceanography*, 27, 126–141, 2014.
- Bresnahan, P. J., Takeshita, Y., Wirth, T., Martz, T. R., Cyronak, T., Albright, R., Wolfe, K., Warren, J. K., and Mertz, K.: Autonomous in situ calibration of ion-sensitive field effect transistor pH sensors, *Limnology and Oceanography: Methods*, 19, 132–144, 2021.
- 715 Broullón, D., Pérez, F. F., Velo, A., Hoppema, M., Olsen, A., Takahashi, T., Key, R. M., Tanhua, T., González-Dávila, M., Jeansson, E., et al.: A global monthly climatology of total alkalinity: a neural network approach, *Earth System Science Data*, 11, 1109–1127, 2019.
- Canadell, J. G., Monteiro, P. M., Costa, M. H., Da Cunha, L. C., Cox, P. M., Alexey, V., Henson, S., Ishii, M., Jaccard, S., Koven, C., et al.: Global carbon and other biogeochemical cycles and feedbacks In *Climate Change 2021: The Physical Science Basis. Contribution of Working Group I to the Sixth Assessment Report of the Intergovernmental Panel on Climate Change*, Cambridge University Press,
720 <https://doi.org/10.1017/9781009157896.007>, 2021.
- Carter, B. R., Williams, N. L., Gray, A. R., and Feely, R. A.: Locally interpolated alkalinity regression for global alkalinity estimation, *Limnology and Oceanography: Methods*, 14, 268–277, <https://doi.org/https://doi.org/10.1002/lom3.10087>, 2016.
- Carter, B. R., Feely, R. A., Williams, N. L., Dickson, A. G., Fong, M. B., and Takeshita, Y.: Updated methods for global locally interpolated estimation of alkalinity, pH, and nitrate, *Limnology and Oceanography: Methods*, 16, 119–131,
725 <https://doi.org/https://doi.org/10.1002/lom3.10232>, 2018.
- Chau, T. T. T., Gehlen, M., and Chevallier, F.: Global ocean surface carbon product, Research Report CMEMS-MOB-QUID-015-008, Le Laboratoire des Sciences du Climat et de l'Environnement, <https://doi.org/10.48670/moi-00047>, quality Information Document, 2022a.
- Chau, T. T. T., Gehlen, M., and Chevallier, F.: A seamless ensemble-based reconstruction of surface ocean *p*CO₂ and air–sea CO₂ fluxes over the global coastal and open oceans, *Biogeosciences*, 19, 1087–1109, <https://doi.org/10.5194/bg-19-1087-2022>, 2022b.

- 730 Chau, T. T. T., Gehlen, M., Metzl, N., and Chevallier, F.: CMEMS-LSCE: A global 0.25-degree, monthly reconstruction of the surface ocean carbonate system, ESPRI/IPSL [dataset], <https://doi.org/10.14768/a2f0891b-763a-49e9-af1b-78ed78b16982>, 2023.
- Chevallier, F.: On the parallelization of atmospheric inversions of CO₂ surface fluxes within a variational framework, *Geoscientific Model Development*, 6, 783–790, <https://doi.org/10.5194/gmd-6-783-2013>, 2013.
- Chevallier, F., Fisher, M., Peylin, P., Serrar, S., Bousquet, P., Bréon, F.-M., Chédin, A., and Ciais, P.: Inferring CO₂ sources and
735 sinks from satellite observations: Method and application to TOVS data, *Journal of Geophysical Research: Atmospheres*, 110, <https://doi.org/https://doi.org/10.1029/2005JD006390>, 2005.
- Chevallier, F., Ciais, P., Conway, T. J., Aalto, T., Anderson, B. E., Bousquet, P., Brunke, E. G., Ciattaglia, L., Esaki, Y., Fröhlich, M., Gomez, A., Gomez-Pelaez, A. J., Haszpra, L., Krummel, P. B., Langenfelds, R. L., Leuenberger, M., Machida, T., Maignan, F., Matsueda, H., Morguí, J. A., Mukai, H., Nakazawa, T., Peylin, P., Ramonet, M., Rivier, L., Sawa, Y., Schmidt, M., Steele, L. P., Vay, S. A., Vermeulen,
740 A. T., Wofsy, S., and Worthy, D.: CO₂ surface fluxes at grid point scale estimated from a global 21 year reanalysis of atmospheric measurements, *Journal of Geophysical Research: Atmospheres*, 115, <https://doi.org/https://doi.org/10.1029/2010JD013887>, 2010.
- Coppola, L., Boutin, J., Gattuso, J.-P., Lefevre, D., and Metzl, N.: The Carbonate System in the Ligurian Sea, chap. 4, pp. 79–103, John Wiley & Sons, Ltd, <https://doi.org/https://doi.org/10.1002/9781119706960.ch4>, 2020.
- Coppola, L., Diamond, R. E., and Carval, T.: Dyfamed observatory data. SEANOE [dataset], <https://doi.org/0.17882/43749>, 2021.
- 745 Denvil-Sommer, A., Gehlen, M., Vrac, M., and Mejia, C.: LSCE-FFNN-v1: a two-step neural network model for the reconstruction of surface ocean pCO₂ over the global ocean, *Geoscientific Model Development*, 12, 2091–2105, <https://doi.org/10.5194/gmd-12-2091-2019>, 2019.
- Dickson, A. G.: Standard potential of the reaction $-AgCl(s)+1/2H_2(g)=Ag(s)+HCl(aq)$ and the standard acidity constant of the ion HSO₄⁻ in synthetic sea-water from 273.15-K to 318.15-K, *Journal of Chemical Thermodynamics*, 22, 113–127, [https://doi.org/doi:10.1016/0021-9614\(90\)90074-z](https://doi.org/doi:10.1016/0021-9614(90)90074-z), 1990.
- 750 Dickson, A. G.: The carbon dioxide system in seawater: equilibrium chemistry and measurements in Guide to best practices for ocean acidification research and data reporting, https://www.pmel.noaa.gov/co2/files/dickson_thecarbondioxidesysteminseawater_equilibriumchemistryandmeasurementspp17-40.pdf, 2010.
- Dickson, A. G., Sabine, C. L., and Christian, J. R.: Guide to best practices for ocean CO₂ measurements., North Pacific Marine Science Organization, 2007.
- 755 Doney, S. C., Fabry, V. J., Feely, R. A., and Kleypas, J. A.: Ocean acidification: the other CO₂ problem, *Annual review of marine science*, 1, 169–192, 2009.
- Doney, S. C., Busch, D. S., Cooley, S. R., and Kroeker, K. J.: The impacts of ocean acidification on marine ecosystems and reliant human communities, *Annual Review of Environment and Resources*, 45, 2020.
- Dore, J. E., Lukas, R., Sadler, D. W., Church, M. J., and Karl, D. M.: Physical and biogeochemical modulation of ocean acidification in the
760 central North Pacific, *Proceedings of the National Academy of Sciences*, 106, 12 235–12 240, 2009.
- Droghei, R., Buongiorno Nardelli, B., and Santoleri, R.: A new global sea surface salinity and density dataset from multivariate observations (1993–2016), *Frontiers in Marine Science*, 5, 84, 2018.
- Fabry, V. J., Seibel, B. A., Feely, R. A., and Orr, J. C.: Impacts of ocean acidification on marine fauna and ecosystem processes, *ICES Journal of Marine Science*, 65, 414–432, 2008.
- 765 Feely, R. A., Wanninkhof, R., Takahashi, T., and Tans, P.: Influence of El Niño on the equatorial Pacific contribution to atmospheric CO₂ accumulation, *Nature*, 398, 597–601, 1999.

- Feely, R. A., Sabine, C. L., Takahashi, T., and Wanninkhof, R.: Uptake And Storage Of Carbon Dioxide In The Ocean: The Global CO₂ Survey, *OCEANOGRAPHY-WASHINGTON DC-OCEANOGRAPHY SOCIETY*-, 14, 18–32, 2001.
- Fischer, P., Schwanitz, M., Loth, R., Posner, U., Brand, M., and Schröder, F.: First year of practical experiences of the new Arctic AWIPEV-COSYNA cabled Underwater Observatory in Kongsfjorden, Spitsbergen, *Ocean Science*, 13, 259–272, <https://doi.org/10.5194/os-13-259-2017>, 2017.
- Friedlingstein, P., O’Sullivan, M., Jones, M. W., Andrew, R. M., Gregor, L., Hauck, J., Le Quéré, C., Luijkx, I. T., Olsen, A., Peters, G. P., Peters, W., Pongratz, J., Schwingshackl, C., Sitch, S., Canadell, J. G., Ciais, P., Jackson, R. B., Alin, S. R., Alkama, R., Arneeth, A., Arora, V. K., Bates, N. R., Becker, M., Bellouin, N., Bittig, H. C., Bopp, L., Chevallier, F., Chini, L. P., Cronin, M., Evans, W., Falk, S., Feely, R. A., Gasser, T., Gehlen, M., Gkritzalis, T., Gloege, L., Grassi, G., Gruber, N., Gürses, O., Harris, I., Hefner, M., Houghton, R. A., Hurtt, G. C., Iida, Y., Ilyina, T., Jain, A. K., Jersild, A., Kadono, K., Kato, E., Kennedy, D., Klein Goldewijk, K., Knauer, J., Korsbakken, J. I., Landschützer, P., Lefèvre, N., Lindsay, K., Liu, J., Liu, Z., Marland, G., Mayot, N., McGrath, M. J., Metzl, N., Monacci, N. M., Munro, D. R., Nakaoka, S.-I., Niwa, Y., O’Brien, K., Ono, T., Palmer, P. I., Pan, N., Pierrot, D., Pockock, K., Poulter, B., Resplandy, L., Robertson, E., Rödenbeck, C., Rodriguez, C., Rosan, T. M., Schwinger, J., Séférian, R., Shutler, J. D., Skjelvan, I., Steinhoff, T., Sun, Q., Sutton, A. J., Sweeney, C., Takao, S., Tanhua, T., Tans, P. P., Tian, X., Tian, H., Tilbrook, B., Tsujino, H., Tubiello, F., van der Werf, G. R., Walker, A. P., Wanninkhof, R., Whitehead, C., Willstrand Wranne, A., Wright, R., Yuan, W., Yue, C., Yue, X., Zaehle, S., Zeng, J., and Zheng, B.: Global Carbon Budget 2022, *Earth System Science Data*, 14, 4811–4900, <https://doi.org/10.5194/essd-14-4811-2022>, 2022.
- Garcia, H., Weathers, K., Paver, C., Smolyar, I., Boyer, T., Locarnini, M., Zweng, M., Mishonov, A., Baranova, O., Seidov, D., et al.: World ocean atlas 2018. Vol. 4: Dissolved inorganic nutrients (phosphate, nitrate and nitrate+ nitrite, silicate), <https://archimer.ifremer.fr/doc/00651/76336/>, 2019.
- Gattuso, J.-P. and Hansson, L.: *Ocean acidification*, Oxford university press, 2011.
- Gattuso, J.-P., Alliouane, S., and Fischer, P.: High-frequency, year-round time series of the carbonate chemistry in a high-Arctic fjord (Svalbard), *Earth System Science Data*, 15, 2809–2825, <https://doi.org/10.5194/essd-15-2809-2023>, 2023.
- Gehlen, M., Gruber, N., Gangstø, R., Bopp, L., and Oschlies, A.: Biogeochemical consequences of ocean acidification and feedbacks to the earth system, *Ocean acidification*, 1, 230–248, 2011.
- González-Dávila, M. and Santana-Casiano, J.: Sea surface and atmospheric fco₂ data measured during the estoc time series cruises from 1995-2009, CDIAC, Oak Ridge National Laboratory, US Department of Energy, Oak Ridge, Tennessee. doi, 10, 2009.
- Good, S., Fiedler, E., Mao, C., Martin, M. J., Maycock, A., Reid, R., Roberts-Jones, J., Searle, T., Waters, J., While, J., and Worsfold, M.: The Current Configuration of the OSTIA System for Operational Production of Foundation Sea Surface Temperature and Ice Concentration Analyses, *Remote Sensing*, 12, <https://www.mdpi.com/2072-4292/12/4/720>, 2020.
- Gregor, L. and Gruber, N.: OceanSODA-ETHZ: a global gridded data set of the surface ocean carbonate system for seasonal to decadal studies of ocean acidification, *Earth System Science Data*, 13, 777–808, <https://doi.org/10.5194/essd-13-777-2021>, 2021.
- Gregor, L., Lebehot, A. D., Kok, S., and Scheel Monteiro, P. M.: A comparative assessment of the uncertainties of global surface ocean CO₂ estimates using a machine-learning ensemble (CSIR-ML6 version 2019a) – have we hit the wall?, *Geoscientific Model Development*, 12, 5113–5136, <https://doi.org/10.5194/gmd-12-5113-2019>, 2019.
- Gruber, N., Clement, D., Carter, B. R., Feely, R. A., Van Heuven, S., Hoppema, M., Ishii, M., Key, R. M., Kozyr, A., Lauvset, S. K., et al.: The oceanic sink for anthropogenic CO₂ from 1994 to 2007, *Science*, 363, 1193–1199, 2019.

- Hauck, J., Zeising, M., Le Quéré, C., Gruber, N., Bakker, D. C., Bopp, L., Chau, T. T. T., Gürses, Ö., Ilyina, T., Landschützer, P., Lenton, A., Resplandy, L., Rödenbeck, C., Schwinger, J., and Séférian, R.: Consistency and Challenges in the Ocean Carbon Sink Estimate for the Global Carbon Budget, *Frontiers in Marine Science*, 7, 852, <https://doi.org/10.3389/fmars.2020.571720>, 2020.
- Hoffmann, L. J., Breitbarth, E., Boyd, P. W., and Hunter, K. A.: Influence of ocean warming and acidification on trace metal biogeochemistry, *Marine Ecology Progress Series*, 470, 191–205, 2012.
- Hopkins, F. E., Suntharalingam, P., Gehlen, M., Andrews, O., Archer, S. D., Bopp, L., Buitenhuis, E., Dadou, I., Duce, R., Goris, N., et al.: The impacts of ocean acidification on marine trace gases and the implications for atmospheric chemistry and climate, *Proceedings of the Royal Society A*, 476, 20190769, 2020.
- Ibáñez, J. S. P., Diverrès, D., Araujo, M., and Lefèvre, N.: Seasonal and interannual variability of sea-air CO₂ fluxes in the tropical Atlantic affected by the Amazon River plume, *Global Biogeochemical Cycles*, 29, 1640–1655, 2015.
- Iida, Y., Takatani, Y., Kojima, A., and Ishii, M.: Global trends of ocean CO₂ sink and ocean acidification: an observation-based reconstruction of surface ocean inorganic carbon variables, *Journal of Oceanography*, 77, 323–358, 2021.
- Jiang, L.-Q., Carter, B. R., Feely, R. A., Lauvset, S. K., and Olsen, A.: Surface ocean pH and buffer capacity: past, present and future, *Scientific reports*, 9, 1–11, 2019.
- Jones, S., Le Quéré, C., and Rödenbeck, C.: Autocorrelation characteristics of surface ocean pCO₂ and air-sea CO₂ fluxes, *Global biogeochemical cycles*, 26, 2012.
- Key, R. M., Kozyr, A., Sabine, C. L., Lee, K., Wanninkhof, R., Bullister, J. L., Feely, R. A., Millero, F. J., Mordy, C., and Peng, T.-H.: A global ocean carbon climatology: Results from Global Data Analysis Project (GLODAP), *Global Biogeochemical Cycles*, 18, <https://doi.org/https://doi.org/10.1029/2004GB002247>, 2004.
- Körtzinger, A.: Determination of carbon dioxide partial pressure (pCO₂), chap. 9, pp. 149–158, John Wiley & Sons, Ltd, <https://doi.org/https://doi.org/10.1002/9783527613984.ch9>, 1999.
- Landschützer, P., Gruber, N., and Bakker, D. C.: Decadal variations and trends of the global ocean carbon sink, *Global Biogeochemical Cycles*, 30, 1396–1417, 2016.
- Landschützer, P., Ilyina, T., and Lovenduski, N. S.: Detecting Regional Modes of Variability in Observation-Based Surface Ocean pCO₂, *Geophysical Research Letters*, 46, 2670–2679, 2019.
- Landschützer, P., Laruelle, G. G., Roobaert, A., and Regnier, P.: A uniform pCO₂ climatology combining open and coastal oceans, *Earth System Science Data*, 12, 2537–2553, <https://doi.org/10.5194/essd-12-2537-2020>, 2020.
- Laruelle, G. G., Landschützer, P., Gruber, N., Tison, J.-L., Delille, B., and Regnier, P.: Global high-resolution monthly pCO₂ climatology for the coastal ocean derived from neural network interpolation, *Biogeosciences*, 14, 4545–4561, 2017.
- Lauvset, S. K. and Gruber, N.: Long-term trends in surface ocean pH in the North Atlantic, *Marine Chemistry*, 162, 71–76, 2014.
- Lauvset, S. K., Gruber, N., Landschützer, P., Olsen, A., and Tjiputra, J.: Trends and drivers in global surface ocean pH over the past 3 decades, *Biogeosciences*, 12, 1285–1298, <https://doi.org/10.5194/bg-12-1285-2015>, 2015.
- Lauvset, S. K., Lange, N., Tanhua, T., Bittig, H. C., Olsen, A., Kozyr, A., Alin, S., Álvarez, M., Azetsu-Scott, K., Barbero, L., Becker, S., Brown, P. J., Carter, B. R., da Cunha, L. C., Feely, R. A., Hoppema, M., Humphreys, M. P., Ishii, M., Jeansson, E., Jiang, L.-Q., Jones, S. D., Lo Monaco, C., Murata, A., Müller, J. D., Pérez, F. F., Pfeil, B., Schirnack, C., Steinfeldt, R., Suzuki, T., Tilbrook, B., Ulfso, A., Velo, A., Woosley, R. J., and Key, R. M.: GLODAPv2.2022: the latest version of the global interior ocean biogeochemical data product, *Earth System Science Data*, 14, 5543–5572, <https://doi.org/10.5194/essd-14-5543-2022>, 2022a.

- 840 Lauvset, S. K., Lange, N., Tanhua, T., Bittig, H. C., Olsen, A., Kozyr, A., Alin, S., Álvarez, M., Azetsu-Scott, K., Barbero, L., Becker, S., Brown, P. J., Carter, B. R., da Cunha, L. C., Feely, R. A., Hoppema, M., Humphreys, M. P., Ishii, M., Jeansson, E., Jiang, L.-Q., Jones, S. D., Lo Monaco, C., Murata, A., Müller, J. D., Pérez, F. F., Pfeil, B., Schirnack, C., Steinfeldt, R., Suzuki, T., Tilbrook, B., Ulfso, A., Velo, A., Woosley, R. J., and Key, R. M.: Global Ocean Data Analysis Project version 2.2022 (GLODAPv2.2022) (NCEI Accession 0257247), NOAA National Centers for Environmental Information [dataset], <https://doi.org/10.25921/1f4w-0t92>, 2022b.
- 845 Lee, K., Tong, L. T., Millero, F. J., Sabine, C. L., Dickson, A. G., Goyet, C., Park, G.-H., Wanninkhof, R., Feely, R. A., and Key, R. M.: Global relationships of total alkalinity with salinity and temperature in surface waters of the world's oceans, *Geophysical research letters*, 33, 2006.
- Leseurre, C., Lo Monaco, C., Reverdin, G., Metzl, N., Fin, J., Mignon, C., and Benito, L.: Summer trends and drivers of sea surface fCO₂ and pH changes observed in the southern Indian Ocean over the last two decades (1998–2019), *Biogeosciences*, 19, 2599–2625, <https://doi.org/10.5194/bg-19-2599-2022>, 2022.
- 850 Lewis, E. and Wallace, D.: CO2SYS-Program developed for the CO₂ system calculations, Carbon Dioxide Inf Anal Center Report ORNL/CDIAC-105, <https://doi.org/https://doi.org/10.15485/1464255>, 1998.
- Lueker, T. J., Dickson, A. G., and Keeling, C. D.: Ocean pCO₂ calculated from dissolved inorganic carbon, alkalinity, and equations for K₁ and K₂: validation based on laboratory measurements of CO₂ in gas and seawater at equilibrium, *Marine chemistry*, 70, 105–119, 2000.
- 855 Ma, D., Gregor, L., and Gruber, N.: Four Decades of Trends and Drivers of Global Surface Ocean Acidification, *Global Biogeochemical Cycles*, 37, e2023GB007765, <https://doi.org/https://doi.org/10.1029/2023GB007765>, e2023GB007765 2023GB007765, 2023.
- Maritorena, S., d'Andon, O. H. F., Mangin, A., and Siegel, D. A.: Merged satellite ocean color data products using a bio-optical model: Characteristics, benefits and issues, *Remote Sensing of Environment*, 114, 1791–1804, <https://doi.org/https://doi.org/10.1016/j.rse.2010.04.002>, 2010.
- 860 Menemenlis, D., Campin, J., Heimbach, P., Hill, C., Lee, T., Nguyen, A., Schodlok, M., and Zhang, H.: ECCO2: High Resolution Global Ocean and Sea Ice Data Synthesis, 2008, OS31C-1292, 2008.
- Menviel, L., Spence, P., Yu, J., Chamberlain, M., Matear, R., Meissner, K., and England, M. H.: Southern Hemisphere westerlies as a driver of the early deglacial atmospheric CO₂ rise, *Nature Communications*, 9, 1–12, 2018.
- Metzl, N. and Lo Monaco, C.: OISO - Ocean Indien Service d'Observation [dataset], <https://doi.org/10.18142/228>, 1998.
- 865 Michaels, A. F. and Knap, A. H.: Overview of the US JGOFS Bermuda Atlantic Time-series Study and the Hydrostation S program, *Deep Sea Research Part II: Topical Studies in Oceanography*, 43, 157–198, 1996.
- Millero, F. J., Woosley, R., Ditrolio, B., and Waters, J.: Effect of ocean acidification on the speciation of metals in seawater, *Oceanography*, 22, 72–85, 2009.
- Mucci, A.: The solubility of calcite and aragonite in seawater at various salinities, temperatures, and one atmosphere total pressure, *American*
870 *Journal of Science*, 283, 780–799, 1983.
- Nardelli, B. B., Droghei, R., and Santoleri, R.: Multi-dimensional interpolation of SMOS sea surface salinity with surface temperature and in situ salinity data, *Remote Sensing of Environment*, 180, 392–402, 2016.
- Olafsson, J., Olafsdottir, S., Benoit-Cattin, A., and Takahashi, T.: The Irminger Sea and the Iceland Sea time series measurements of sea water carbon and nutrient chemistry 1983–2008, *Earth System Science Data*, 2, 99–104, 2010.
- 875 Olivier, L., Boutin, J., Reverdin, G., Lefèvre, N., Landschützer, P., Speich, S., Karstensen, J., Labaste, M., Noisel, C., Ritschel, M., Steinhoff, T., and Wanninkhof, R.: Wintertime process study of the North Brazil Current rings reveals the region as a larger sink for CO₂ than expected, *Biogeosciences*, 19, 2969–2988, <https://doi.org/10.5194/bg-19-2969-2022>, 2022.

- Olsen, A., Key, R. M., Van Heuven, S., Lauvset, S. K., Velo, A., Lin, X., Schirnack, C., Kozyr, A., Tanhua, T., Hoppema, M., et al.: The Global Ocean Data Analysis Project version 2 (GLODAPv2)—an internally consistent data product for the world ocean, *Earth System Science Data*, 8, 297–323, 2016.
- 880 Orr, J. C., Fabry, V. J., Aumont, O., Bopp, L., Doney, S. C., Feely, R. A., Gnanadesikan, A., Gruber, N., Ishida, A., Joos, F., et al.: Anthropogenic ocean acidification over the twenty-first century and its impact on calcifying organisms, *Nature*, 437, 681–686, 2005.
- Orr, J. C., Epitalon, J.-M., Dickson, A. G., and Gattuso, J.-P.: Routine uncertainty propagation for the marine carbon dioxide system, *Marine Chemistry*, 207, 84–107, <https://doi.org/https://doi.org/10.1016/j.marchem.2018.10.006>, 2018.
- 885 Palmiéri, J., Orr, J., Dutay, J.-C., Béranger, K., Schneider, A., Beuvier, J., and Somot, S.: Simulated anthropogenic CO₂ storage and acidification of the Mediterranean Sea, *Biogeosciences*, 12, 781–802, 2015.
- Park, P. K.: OCEANIC CO₂ SYSTEM: AN EVALUATION OF TEN METHODS OF INVESTIGATION¹, *Limnology and Oceanography*, 14, 179–186, <https://doi.org/https://doi.org/10.4319/lo.1969.14.2.0179>, 1969.
- Pérez, F. F., Olafsson, J., Ólafsdóttir, S. R., Fontela, M., and Takahashi, T.: Contrasting drivers and trends of ocean acidification in the subarctic Atlantic, *Scientific Reports*, 11, 1–16, 2021.
- 890 Pfeil, B., Olsen, A., Bakker, D. C., Hankin, S., Koyuk, H., Kozyr, A., Malczyk, J., Manke, A., Metzl, N., Sabine, C. L., et al.: A uniform, quality-controlled Surface Ocean CO₂ Atlas (SOCAT), *Earth System Science Data*, 5, 125–143, 2013.
- Rödenbeck, C., Keeling, R. F., Bakker, D. C., Metzl, N., Olsen, A., Sabine, C., and Heimann, M.: Global surface-ocean pCO₂ and sea-air CO₂ flux variability from an observation-driven ocean mixed-layer scheme, *Ocean Science*, 9, 193–216, 2013.
- 895 Rose, A.: *Vision: human and electronic*, Springer Science & Business Media, 2013.
- Sabine, C. L., Key, R. M., Feely, R. A., and Greeley, D.: Inorganic carbon in the Indian Ocean: Distribution and dissolution processes, *Global Biogeochemical Cycles*, 16, 15–1, 2002.
- Sabine, C. L., Hankin, S., Koyuk, H., Bakker, D. C. E., Pfeil, B., Olsen, A., Metzl, N., Kozyr, A., Fassbender, A., Manke, A., Malczyk, J., Akl, J., Alin, S. R., Bellerby, R. G. J., Borges, A., Boutin, J., Brown, P. J., Cai, W.-J., Chavez, F. P., Chen, A., Cosca, C., Feely, R. A., González-Dávila, M., Goyet, C., Hardman-Mountford, N., Heinze, C., Hoppema, M., Hunt, C. W., Hydes, D., Ishii, M., Johannessen, T., Key, R. M., Körtzinger, A., Landschützer, P., Lauvset, S. K., Lefèvre, N., Lenton, A., Lourantou, A., Merlivat, L., Midorikawa, T., Mintrop, L., Miyazaki, C., Murata, A., Nakadate, A., Nakano, Y., Nakaoka, S., Nojiri, Y., Omar, A. M., Padin, X. A., Park, G.-H., Paterson, K., Perez, F. F., Pierrot, D., Poisson, A., Ríos, A. F., Salisbury, J., Santana-Casiano, J. M., Sarma, V. V. S. S., Schlitzer, R., Schneider, B., Schuster, U., Sieger, R., Skjelvan, I., Steinhoff, T., Suzuki, T., Takahashi, T., Tedesco, K., Telszewski, M., Thomas, H., Tilbrook, B., Vandemark, D., Veness, T., Watson, A. J., Weiss, R., Wong, C. S., and Yoshikawa-Inoue, H.: Surface Ocean CO₂ Atlas (SOCAT) gridded data products, *Earth System Science Data*, 5, 145–153, <https://doi.org/10.5194/essd-5-145-2013>, 2013.
- 900 Sarma, V. V. S. S., Lenton, A., Law, R. M., Metzl, N., Patra, P. K., Doney, S., Lima, I. D., Dlugokencky, E., Ramonet, M., and Valsala, V.: Sea-air CO₂ fluxes in the Indian Ocean between 1990 and 2009, *Biogeosciences*, 10, 7035–7052, <https://doi.org/10.5194/bg-10-7035-2013>, 2013.
- 910 Sarma, V. V. S. S., Sridevi, B., Metzl, N., Patra, P. K., Lachkar, Z., Chakraborty, K., Goyet, C., Levy, M., Mehari, M., and Chandra, N.: Air-Sea Fluxes of CO₂ in the Indian Ocean Between 1985 and 2018: A Synthesis Based on Observation-Based Surface CO₂, Hindcast and Atmospheric Inversion Models, *Global Biogeochemical Cycles*, 37, e2023GB007694, <https://doi.org/https://doi.org/10.1029/2023GB007694>, 2023.
- Skjelvan, I., Lauvset, S. K., Johannessen, T., Gundersen, K., and Skagseth, Ø.: Decadal trends in ocean acidification from the Ocean Weather Station M in the Norwegian Sea, *Journal of Marine Systems*, 234, 103775, <https://doi.org/10.1016/j.jmarsys.2022.103775>, 2022.
- 915

- Steinberg, D. K., Carlson, C. A., Bates, N. R., Johnson, R. J., Michaels, A. F., and Knap, A. H.: Overview of the US JGOFS Bermuda Atlantic Time-series Study (BATS): a decade-scale look at ocean biology and biogeochemistry, *Deep Sea Research Part II: Topical Studies in Oceanography*, 48, 1405–1447, 2001.
- 920 Sutton, A. J., Feely, R. A., Maenner-Jones, S., Musielwicz, S., Osborne, J., Dietrich, C., Monacci, N., Cross, J., Bott, R., Kozyr, A., et al.: Autonomous seawater pCO₂ and pH time series from 40 surface buoys and the emergence of anthropogenic trends, *Earth System Science Data*, 11, 421–439, 2019.
- 925 Takahashi, T., Sutherland, S. C., Wanninkhof, R., Sweeney, C., Feely, R. A., Chipman, D. W., Hales, B., Friederich, G., Chavez, F., Sabine, C., Watson, A., Bakker, D. C., Schuster, U., Metzl, N., Yoshikawa-Inoue, H., Ishii, M., Midorikawa, T., Nojiri, Y., Körtzinger, A., Steinhoff, T., Hoppema, M., Olafsson, J., Arnarson, T. S., Tilbrook, B., Johannessen, T., Olsen, A., Bellerby, R., Wong, C., Delille, B., Bates, N., and de Baar, H. J.: Climatological mean and decadal change in surface ocean pCO₂, and net sea–air CO₂ flux over the global oceans, *Deep Sea Research Part II: Topical Studies in Oceanography*, 56, 554–577, <https://doi.org/https://doi.org/10.1016/j.dsr2.2008.12.009>, 2009.
- Takahashi, T., Sutherland, S. C., Chipman, D. W., Goddard, J. G., Ho, C., Newberger, T., Sweeney, C., and Munro, D.: Climatological distributions of pH, pCO₂, total CO₂, alkalinity, and CaCO₃ saturation in the global surface ocean, and temporal changes at selected locations, *Marine Chemistry*, 164, 95–125, 2014.
- 930 Thomsen, J., Haynert, K., Wegner, K. M., and Melzner, F.: Impact of seawater carbonate chemistry on the calcification of marine bivalves, *Biogeosciences*, 12, 4209–4220, 2015.
- Uppstrom, L.: The boron/chlorinity ratio of deep-sea water from the Pacific Ocean, *Deep Sea Res.*, 21, 161–162, 1974.
- Van Heuven, S., Pierrot, D., Rae, J., Lewis, E., and Wallace, D.: CO₂SYST v 1.1, MATLAB program developed for CO₂ system calculations, ORNL/CDIAC-105b. Oak Ridge, TN: Oak Ridge National Laboratory, https://cdiac.ess-dive.lbl.gov/ftp/co2sys/CO2SYS_calc_MATLAB_v1.1/, 2011.
- 935 Wosley, R. J.: Evaluation of the temperature dependence of dissociation constants for the marine carbon system using pH and certified reference materials, *Marine Chemistry*, 229, 103–114, 2021.
- Zeebe, R. E. and Wolf-Gladrow, D.: CO₂ in seawater: equilibrium, kinetics, isotopes, 65, Gulf Professional Publishing, 2001.